

Stability and Performance Improvement of a Cluster State Generator for Universal Quantum Computing

Chun-Hung Chang
Yilan, Taiwan

M.S. Physics, National Tsing-Hua University, 2012

A Thesis presented to the Graduate Faculty of the University
of Virginia in Candidacy for the Degree of Doctor of
Philosophy

Department of Physics
University of Virginia
December, 2021

Abstract

Quantum computing promises exponential speedup over classical computing for specific algorithms [38], such as integer factoring [53] and quantum simulation [19]. While a classical computer follows the rules of classical physics, a quantum computer follows the rules of quantum physics. These rules include superposition and entanglement. Classical computers store the information into bits, 0 and 1, and quantum computers typically use qubits, superpositions of $|0\rangle$ and $|1\rangle$, to store the information. However, in this work, the information is stored in quantized electromagnetic fields called qumodes. Just like the qubits are regarded as discrete variables due to their basis being composed of $|0\rangle$ and $|1\rangle$, the qumodes are named continuous variables because their basis is formed of the eigenstates of amplitude quadratures (or phase quadratures) which are continuous. To use qumodes for quantum computing, measurement-based quantum computing is preferred, which requires a particular type of large entangled quantum states, cluster states, as calculation resources. Simply speaking, cluster states are sparsely (i.e., locally) but fully entangled networks of qubits or qumodes, represented by a two-dimensional graph. The computing is performed by local measurements on each qumode with feedforward. To perform universal quantum computing, preparing a 2-dimensional (2-d) cluster state is one of the criteria [49] to achieve the quantum speed up. Suppose one can prepare a 3-d cluster state. In that case, it is possible to perform topological quantum error correction encoding [50] to decrease the error rate to a small amount. Therefore, this thesis aims to provide a method to generate 2-d and 3-d cluster states and then experimentally verify the states.

This thesis will discuss a theoretical method that generates 1-d, 2-d, and 3-d cluster states in the frequency domain by employing only one optical parametric oscillator (OPO) and one electro-optic modulator (EOM). This thesis will also discuss how the author approaches the experimental realization and verification of 1-d cluster states in the lab. In order to increase the performance and stability of the systems, several improvements have been performed: first and foremost, the observed squeezing was improved from 3.2 dB to 5.0 dB; also, a quantum heterodyne measurement method was devised to verify the cluster states by reconstructing their covariance matrix; last but not least, vast improvements of the stability and performance of the quantum optical setup were achieved by increasing signal-to-noise ratios by one order of magnitude on quantum detection and by two orders of magnitude on servo loops, and by implementing two new servo loops to phase lock all quantum fields.

Acknowledgements

Time flies. Six and half years of graduate school at the University of Virginia is just like a dream. I would like to express my appreciations to many people. Without their help and supports, there is no way I can finish this thesis.

First of all, I sincerely thank my advisor Prof. Olivier Pfister for his continual support and guidance to my research work. Prof. Pfister is a cheerful, creative, and passionate supervisor that I ask no more. He completely trusts me and allows me to freely explore in the research. I truly learned a lot from him, not just only the fearless attitude and systematic approach to face any difficulties, but also an optimistic spirit in life. I am thankful to have him as my advisor.

I thank all my committee members Prof. Cass Sackett, Prof. Peter Schauss, and Prof. Xu Yi for a comprehensive discussion about my research and providing suggestions and comments to make this thesis better.

I thank all my QFQI labmates and colleagues for the help and discussions: Dr. Rajveer Nehra for walking with me to the coffee shop and the conversations we had about all sort of topics; Miller Eaton for willing to share coffee and for spending the time discussing all sort of experimental problems with me; I thank Xuan Zhu for working together on the EOM paper and for exchanging our life experiences; I thank Dr. Carlos González-Arciniegas for the discussion about all sort of theory and for helping me understand better about the quantum information science; I thank Aye Lu Win, Benjamin Godek, Zack Carson, Rafael Alexander, Jacob Higgins, Nicolas Fabre, and Amr Hossameldin for all the help they provided.

I thank all the Physics department staff for all sort of support and help they provided. Without their help, my research life wouldn't be this smooth.

I thank all the members of Taiwanese Graduate Student Association for holding many events to celebrate Taiwan festival and create opportunities to bring Taiwanese students together. Those celebrations always can ease my home sick and make me happy.

Last but not the least, I want to thank my family for their supports. I especially want to thank my lovely wife, Dr. Ying-Tsen Liu, for her wholehearted supports and the joys she brings to me.

Contents

1	Introduction	1
1.1	Overview	1
1.2	Thesis Plan	2
2	Quantum Optics	4
2.1	Quantum Harmonic Oscillators	4
2.2	Heisenberg Uncertainty Principle	6
2.3	Three Pictures	7
2.3.1	Schrödinger Picture	7
2.3.2	Heisenberg Picture	8
2.3.3	Interaction Picture	9
2.4	Quantum States	10
2.4.1	Fock States	10
2.4.2	Coherent States	11
2.5	Beam Splitter	12
2.6	Squeezing Generation, Detection, and Degradation	13
2.6.1	Single-Mode Squeezing	13
2.6.2	Two-Mode Squeezing	15
2.6.3	Squeezing Detection: Balanced Homodyne Detection	16
2.6.4	Squeezing Degradation - Phase Noise and Loss	18
3	Generating the 1-d, 2-d, and 3-d Cluster States by a Phase Modulated Quantum Optical Frequency Comb	24
3.1	Introduction of Measurement-Based Quantum Computing (MBQC) and the Cluster States	24
3.1.1	Bits, Qubits, and Qumodes	24
3.1.2	Measurement-Based Quantum Computing	25
3.1.3	Graph States and Cluster States	27
3.1.4	Stabilizers and Nullifiers	28
3.1.5	H-Graph	29
3.1.6	Graphical Calculus	30
3.2	Cluster State Generation in the Phase-Modulated QOFC	32
3.2.1	Phase Modulation	33
3.2.2	Cluster State Generation in the Phase-Modulated EPR QOFC	34
3.2.2.a	Generation of 1-d cluster states:	34
3.2.2.b	Generation of 2-d ClusterStates:	37
3.2.2.c	Generation of 3-d Cluster States:	39
3.2.3	Graph Error Analysis:	39

4	The Optical Parametric Oscillator	42
4.1	Optical Cavity	42
4.2	Nonlinear Medium	46
4.3	Quantum Optical Frequency Comb	48
4.4	Pound-Drever-Hall (PDH) Locking	51
4.4.1	Introduction of PDH Locking	51
4.4.2	Signal-to-Noise Ratio of PDH Lock	53
4.5	Parametric Gain and Squeezing	54
5	Old OPO setup	56
5.1	Phase Noise Investigation	56
5.2	OPO PDH Cavity Locking Improvement	62
5.3	Preliminary Evidence for Multipartite Entanglement Generation by Phase Modulation of the QOFC	65
6	New OPO setup	70
6.1	OPO Improvements	70
6.1.1	Squeezing Improvement and Calibration	70
6.1.2	The Anomalous OPO Reflected Mode	72
6.1.3	Using reference beam as Local Oscillator	76
6.1.4	Balanced Homodyne Detector Sensitivity Improvement	77
6.1.5	Lifting the Bandwidth of a Balanced Homodyne Detector	80
6.2	Covariance Matrix Measurement Setup	81
6.2.1	Measurement Principle and Plan	81
6.2.2	Two Optical Phase Locks	87
6.2.2.a	Pump and reference beam phase lock	87
6.2.2.b	LO and reference beam phase lock	91
7	Conclusion and Future Work	95

List of Figures

2.1	BS with two input modes and two output modes	12
2.2	Phase diagram for the two-mode squeezed state.	16
2.3	Set up for the balanced homodyne detection	17
2.4	Squeezing traces.	18
2.5	Interference fringe without the phase noise.	19
2.6	Two-point of view about loss.	21
2.7	Loss degrades squeezing and antisqueezing.	22
3.1	Two examples of quantum computing.	26
3.2	Graphical representation of a cluster state.	27
3.3	H-graph representation for two-mode cluster states.	30
3.4	Quantum description of PM of the two-mode squeezed QOFC.	33
3.5	Phase modulation of a single QOFC.	34
3.6	\mathbf{V} and \mathbf{U} graphs for the state generated by OPO-extrinsic PM	35
3.7	Plot of the average trace of \mathbf{U} versus the squeezing parameter r	36
3.8	\mathbf{V} graph of figure 3.6 and its compact representation	37
3.9	Square-grid cluster state and its compact representation	38
3.10	Cubic cluster state over $N=400$ EPR macronodes	40
4.1	The total reflected, total internal, and total transmitted field of a two-mirror cavity	43
4.2	Four-mirror cavity	44
4.3	Illustration of the cavity response for a lossless cavity with $r_1^2 = 0.95$ and $r_2^2 = 0.99995$	45
4.4	The transmittance T is a function of round trip optical phase δ for a symmetric cavity with $R_1 = R_2 = 0.95$	47
4.5	Sum frequency generation	48
4.6	Schematic representations of a nonlinear crystal	49
4.7	A four-mirror one-sided OPO	50
4.8	The principles behind the OPO output fields	51
4.9	The basic layout for PDH cavity locking to a laser	52
4.10	The PDH error signal v.s. modulation frequency	52
4.11	Schematic setup for OPO PDH cavity lock and the OPO emission spectrum	53
4.12	Schematic setup for measuring the parametric gain	54
4.13	reference beam signal with and without pump beam	55
5.1	Former experimental setup for generating 1-d dual-rail wire cluster state	56

5.2	Modified experimental setup after dual-rail wire cluster state generation project.	57
5.3	Interference of laser 1 before OPO and laser 3 after the filter cavity	58
5.4	The first attempt to observe squeezing	59
5.5	Simplified schematic experimental setup for the PLL between laser 1 and laser 3	60
5.6	Checking the 70 MHz signals by a SA	60
5.7	Squeezing measurement after switching the locking beam from laser 1 to laser 3	61
5.8	Spectra of interference fringe signal and PLL error signal when PLL was not activated	61
5.9	Two types of OPO locking beam injection	62
5.10	The improved PDH cavity locking signal	63
5.11	V and U graphs for the state generated by OPO-extrinsic PM	66
5.12	Schematic experimental setup for the preliminary experiment.	67
5.13	Preliminary results of two-mode squeezing with different EOM modulation index.	68
5.14	Two-mode Squeezed Canonical Cluster State with n Extra Qumodes.	69
6.1	Squeezing trace after changing the output coupler mirror from 5% of transmittance to 17% of transmittance	72
6.2	Calibration of the squeezing obtained experimentally from the actual squeezing	73
6.3	Reflected beam profiles at four different resonance conditions	74
6.4	Schematic experimental setup for observing anomalous OPO reflected beam profile	75
6.5	Schematic experimental setup for observing the OPO transmitted beam profile	75
6.6	Schematic experimental setup for using the reference beam as the LO to observe the squeezing	76
6.7	Spectra of balanced homodyne detector signal at 2 mW and 20 μ W.	78
6.8	Transimpedance amplifier	78
6.9	Model results: SNR by using OPA686 and OPA818 with feedback resistance 100 k Ω	79
6.10	New BHD circuit and its performance.	80
6.11	The bandwidth of the OPA686 based balanced homodyne detector	81
6.12	The idea of intra-modes in QOFC	82
6.13	The idea of two-mode covariance matrix reconstruction	83
6.14	Representation of using frequency-shifted LO and reference beam with respect to the interested comb line in the frequency domain	85
6.15	Phase stability improved experimental setup	86
6.16	Calculated error signals	88
6.17	Simplified schematic experimental setup for pump and reference beam phase lock	89
6.18	Recorded reference beam power and the error signal as the pump phase scanned	89
6.19	Reference beam power without and with the phase lock between the reference beam and pump over 10 seconds	91

6.20	Simplified schematic experimental setup for the reference beam and frequency-shifted LO phase lock	92
6.21	Calculated error signal with different demodulated phase δ	93
6.22	Performance test of phase lock between the reference beam and frequency-shifted LO	94

List of Tables

3.1	Correspondence between qubit- and qumode-based quantum computing	25
5.1	Results of phase noise investigation	59
5.2	Comparison of old PDH lock and new PDH lock	64
6.1	Noises of op-amps and parameters used in the model.	80

Chapter 1

Introduction

1.1 Overview

The idea of quantum computing was proposed around 1980, and one of the proposers is Richard Feynman [19]. His main idea is to use a computer that follows quantum mechanics to simulate quantum systems, while this is a challenging task for a computer that follows classical physics. A computer that follows quantum mechanics (classical physics) is called a quantum computer (classical computer). The power of quantum computers is due to a quantum computer that can scale well with the size of the quantum system, which we now call scalability. Furthermore, quantum computers can provide some speed up in certain algorithms, which have great impact on human society. For example, Peter Shor found an efficient quantum algorithm for factoring large numbers [54], which significantly impacts cryptanalysis. Lov Grover found an efficient quantum search algorithm, which can speed up an unstructured search problem quadratically. With these outstanding features and impacts, more and more countries and facilities invest many resources to develop quantum computers.

Up to date, there are three main types of quantum computers listed in the following. The first kind of quantum computer is developed using superconducting transmons, and around 50 entangled qubits have been reported [1]. Second, trapped ions are used as another quantum computer, and about 30 to 70 entangled qubits have been shown [67]. Finally, the third type of quantum computer is developed using optics, which typically have more than 50 entangled qumodes (the photon version of qubits) [69, 13, 63, 30, 2].

The most widely used quantum computing operation is circuit-based quantum computing (CBQC) [40], a classical analogy. The “quantum” circuit comprises quantum gates interconnected by quantum wires, which move the qubits. Computing is performed by an ordered sequence of quantum gates, measurements, and resets. The CBQC is favored in trapped-ion and superconducting quantum computing.

The other type of quantum computing is measurement-based quantum computing (MBQC), which is computationally equivalent to CBQC. The idea of MBQC is proposed by Robert Raussendorf and Hans Briegel in 2002 [51]. To perform MBQC, a particular kind of quantum state, cluster states, need to be prepared ahead of time. For example, suppose one can prepare a square-grid qubits cluster state and perform computations by local measurements on each qubit with feedforward. Once

the calculation is done, the entanglement is destroyed and the cluster state needs to be regenerated for a new calculation. In 2006, Nicolas Menicuci and Peter van Loock generalized the idea of MBQC from qubits (discrete-variable, DV) to qumodes (continuous-variable, CV). More detail about CV MBQC can be found in chapter 3.

There are two significant challenges toward realizing practical quantum computers: realizing scalability and resilience to decoherence [44, 14]. Compared to CBQC, the advantages of CV MBQC are (1) the scalability [44, 42, 33, 35, 20] and (2) the computation performed by measurement is more accessible than the gates implementations in the CBQC. To perform universal quantum computing in CV MBQC [33, 49], 2-d cluster states need to be prepared. To allow topological quantum error correction encoding, one needs to have 3-d cluster states [50]. It is worth mentioning the CV MBQC can be made fault-tolerant at reachable squeezing levels [34, 58, 22].

The goal of this thesis can be separated into three parts. The first part of the thesis is mainly to provide the necessary background knowledge of quantum optics. Since the reader can easily find those content in many textbooks, readers familiar with quantum optics can omit the reading of this part. The second part of the thesis provides a theoretical background about CV cluster states and a simple method (EOM method) we proposed to generate higher-dimensional cluster states in the frequency domain by a phase modulated quantum optical frequency comb. Finally, the third part of the thesis is to present my experimental works toward verifying the cluster states generated by our EOM method to improve the performance and stability of the optical system.

1.2 Thesis Plan

During my time at the University of Virginia as a Ph.D. candidate, my research work was focused on experiments. In the meantime, I also contributed to two theoretical works with my talented colleagues and lab partners. Here is the list of my two publications:

1. Rajveer Nehra, Chun-Hung Chang, Qianhuan Yu, Andreas Beling, and Olivier Pfister,
"Photon-number-resolving segmented detectors based on single-photon avalanche-photodiodes",
Opt. Express 28, 3660 (2020).
2. Xuan Zhu, Chun-Hung Chang, Carlos González-Arciniegas, Avi Pe'er, Jacob Higgins, and Olivier Pfister,
"Hypercubic Cluster States in the Phase-Modulated Quantum Optical Frequency Comb",
Optica 8, 281 (2021).

For the coherence of this thesis, the work for the first publication will not be covered in the content. However, readers interested in reading the work can find the paper online or find Rajveer Nehra's Ph.D. thesis [39].

In chapter 2, I present the quantum model to describe the electromagnetic wave

and the three pictures to depict the evolution of time. Then, I introduce quantum states: Fock states, coherent states, and squeezed states. I also introduce a beam splitter, which is used in the homodyne measurement and loss model. Lastly, the squeezing degradation by phase noise and loss is discussed as well.

In chapter 3, I introduce cluster states, which acts as computing resources for continuous-variable quantum computing. I provide the mathematical description of cluster states, also known as graphical calculus. I also present a simple method we proposed to generate 1-d, 2-d, and 3-d cluster states by a phase-modulated quantum optical frequency comb (QOFC) in the frequency domain. A graph error analysis of the bipartite case about the effect of omitting the spurious graph edges is provided.

In chapter 4, a crucial two-mode cluster states generator, an optical parametric oscillator (OPO), is presented, which can be divided into three sections, an optical cavity, nonlinear medium, and Pound-Drever-Hall (PDH) locking. I also discuss squeezing estimation based on the experimental parameters, such as parametric gain, loss, visibility, and phase noise.

In chapter 5, I present my experimental work to improve the optical system's stability. I will present the phase noise investigation of the optical system. And then, I will show the OPO PDH cavity lock improvement: the signal-to-noise ratio is improved from 40 to more than 3000. Preliminary evidence for multipartite entanglement generation by phase modulation of the QOFC is also discussed and presented.

In chapter 6, the first part is about the OPO improvements. The squeezing is improved by changing the OPO mirror and the observed squeezing is improved from 3 dB around to 5 dB with a squeezing calibration of electronic noise. I will talk about the idea of using a reference beam as a local oscillator, including the advantages and disadvantages of this method. The sensitivity improvement of a balanced homodyne detector will also be presented. The second part is for verification of cluster state by reconstructing covariance matrix. I will discuss the measurement principle and plan by reconstructing a two-mode covariance matrix as an example. Two phase locks to stabilize the phases between three optical fields in order to reconstruct the covariance matrix will also be covered, from error signal derivation to the real implements.

Finally, in chapter 7, I summarize the main results of this thesis and present a brief outlook for future work.

Chapter 2

Quantum Optics

This chapter will introduce the basics of mathematical formalism and physics descriptions in quantum optics. The references for this chapter are my adviser, Prof. Olivier Pfister, Quantum Optics and Quantum Information lecture notes [43], Moran Chen's Ph.D. thesis [12], and Ping Koy Lam's Ph.D. thesis [29].

2.1 Quantum Harmonic Oscillators

For a one-dimensional harmonic oscillator, the Hamiltonian is

$$H = \frac{\hat{P}^2}{2m} + \frac{1}{2}k\hat{X}^2, \quad (2.1)$$

where \hat{P} and \hat{X} are the momentum and position operators. These two operators can be converted into scaled and dimensionless operators by

$$Q = \beta\hat{X}, \quad (2.2)$$

$$P = \frac{\hat{P}}{\beta\hbar}, \quad (2.3)$$

where β is defined by

$$\beta = \sqrt{\frac{m\omega}{\hbar}}, \quad (2.4)$$

m is the mass of oscillator and $\omega = \sqrt{\frac{k}{m}}$ being the resonance angular frequency of the oscillator.

The annihilation and creation operators a and a^\dagger are defined in terms of Q and P as:

$$a = \frac{1}{\sqrt{2}}(Q + iP), \quad (2.5)$$

$$a^\dagger = \frac{1}{\sqrt{2}}(Q - iP). \quad (2.6)$$

Despite the Q and P are Hermitian operators, the a and a^\dagger are not. Therefore, the annihilation and creation operators are not observables. What a and a^\dagger do to

an n phonon number state (a.k.a. Fock states) is adding and removing one phonon from the state:

$$a |n\rangle = \sqrt{n} |n-1\rangle \quad (2.7)$$

$$a^\dagger |n\rangle = \sqrt{n+1} |n+1\rangle \quad (2.8)$$

The commutator of the annihilation and creation operators is:

$$[a, a^\dagger] = 1, \quad (2.9)$$

and the commutator of Q and P is:

$$[Q, P] = i, \quad (2.10)$$

With Eqs. (2.2)-(2.6) above, the Eq. (2.1) can be reformulated as

$$H = \frac{\hbar\omega}{2}(Q^2 + P^2) = \hbar\omega(N + \frac{1}{2}), \quad (2.11)$$

where $N = a^\dagger a$ is the phonon number operator.

Due to the quantization of electromagnetic field [57], the electric field becomes

$$\vec{E}(\vec{r}) = \sum_j \sqrt{\frac{\hbar\omega_j}{2\epsilon_0 L^3}} \hat{e}_j (a_j e^{i\vec{k}_j \cdot \vec{r}} + a_j^\dagger e^{-i\vec{k}_j \cdot \vec{r}}), \quad (2.12)$$

where a_j is the photon annihilation operator for the field mode that is a monochromatic plane wave, propagating in vacuum; \hbar is the Planck constant; ϵ_0 is the permittivity of free space; ω_j is the optical angular frequency of the field; L is the side length of the quantization cube; and \hat{e}_j is polarization unit vector.

So, the dynamics of the electric-field amplitudes can be described by a set of independent quantum harmonic oscillators, $\{a_j\}$ and $\{a_j^\dagger\}$, which follow the commutation relation:

$$[a_i, a_j^\dagger] = \delta_{ij}. \quad (2.13)$$

Also note, by using Eq. (2.5) and (2.6), the Eq. (2.12) can be rewritten as:

$$\vec{E}(\vec{r}) = \sum_j \sqrt{\frac{\hbar\omega_j}{\epsilon_0 L^3}} \hat{e}_j (Q_j \sin \vec{k}_j \cdot \vec{r} + P_j \cos \vec{k}_j \cdot \vec{r}), \quad (2.14)$$

where Q_j and P_j are called amplitude quadrature operator and phase quadrature operator, they also follow the commutation relation:

$$[Q_j, P_k] = i\delta_{jk}. \quad (2.15)$$

Since Q and P are Hermitian operators, and they can be measured from experiments, it is natural to use Q and P to describe each bosonic state, rather than using a and a^\dagger .

The Eq. (2.12) and (2.14) do not show the explicit time dependence. However, it is implicit in the creation and annihilation operators (so do the amplitude and phase quadrature operators). Based on the free field Hamiltonian, their equations of motion are:

$$i\hbar\dot{a}_j = [a_j, H] = \hbar\omega_j[a_j, a_j^\dagger a_j] = \hbar\omega_j a_j, \quad (2.16)$$

$$i\hbar\dot{a}_j^\dagger = [a_j^\dagger, H] = \hbar\omega_j[a_j^\dagger, a_j^\dagger a_j] = -\hbar\omega_j a_j^\dagger. \quad (2.17)$$

We can thus obtain

$$a_j(t) = a_j(0)e^{-i\omega_j t}, \quad (2.18)$$

$$a_j^\dagger(t) = a_j^\dagger(0)e^{i\omega_j t} \quad (2.19)$$

and therefore

$$\vec{E}(\vec{r}, t) = \sum_j \sqrt{\frac{\hbar\omega_j}{2\epsilon_0 L^3}} \hat{e}_j \left[a_j e^{i(\vec{k}_j \cdot \vec{r} - \omega t)} + a_j^\dagger e^{-i(\vec{k}_j \cdot \vec{r} - \omega t)} \right], \quad (2.20)$$

$$\vec{E}(\vec{r}, t) = \sum_j \sqrt{\frac{\hbar\omega_j}{\epsilon_0 L^3}} \hat{e}_j \left[Q_j \cos(\vec{k}_j \cdot \vec{r} - \omega t) + P_j \sin(\vec{k}_j \cdot \vec{r} - \omega t) \right]. \quad (2.21)$$

2.2 Heisenberg Uncertainty Principle

For two operators, A and B , suppose they have commutation relation:

$$[A, B] = c, \quad (2.22)$$

where c is a complex number. Then, they have following uncertainty relation:

$$\Delta A \Delta B \geq \frac{1}{2} |c|, \quad (2.23)$$

where ΔA and ΔB are the standard deviation (STD) of the operator A and B of a given state $|\psi\rangle$, defined as:

$$\Delta A = \sqrt{(\langle \psi | A^2 | \psi \rangle) - (\langle \psi | A | \psi \rangle)^2}. \quad (2.24)$$

Eq. (2.23) is the famous Heisenberg uncertainty principle (HUP) relation, and it implies that it is impossible to know two physical quantities whose commutation relation is nonzero, with arbitrary precision simultaneously.

For photons, from Eq. (2.15), the HUP relations are:

$$\Delta Q \Delta P \geq \frac{1}{2}. \quad (2.25)$$

Taking Fock state as an example, $|\psi\rangle = |n\rangle$, the STD for two quadrature operators is:

$$\Delta Q = \Delta P = \sqrt{n + \frac{1}{2}}, \quad (2.26)$$

which shows the fluctuations in two quadrature measurements and they are known as the quantum noise, and the corresponding HUP relation is:

$$\Delta Q \Delta P = n + \frac{1}{2} \geq \frac{1}{2}. \quad (2.27)$$

It is worth mentioning that the Fock state with $n = 0$ is the ground state of the quantum harmonic oscillator and called the vacuum state. The STD of two quadratures and the HUP relation becomes:

$$\Delta Q_{vac} = \Delta P_{vac} = \frac{1}{\sqrt{2}}, \quad (2.28)$$

$$\Delta Q_{vac} \Delta P_{vac} = \frac{1}{2}, \quad (2.29)$$

which showed the saturation of the HUP relation. The Eq. (2.28) is the standard quantum limit.

2.3 Three Pictures

When describing the dynamics of a time evolved quantum system, there are three equivalent dynamical pictures to formulate the quantum system's evolution mathematically. The three pictures are Schrödinger picture, Heisenberg picture, and Interaction picture. In quantum optics, due to the simplicity and convenience, the Heisenberg picture and Interaction picture are usually preferred.

2.3.1 Schrödinger Picture

In the Schrödinger picture, the operators remain static as $A_S(t) = A_0$ while the quantum states evolves with time: $|\psi_S\rangle = |\psi(t)\rangle$. The time evolution of a quantum system from t_0 to later time t can be described by an unitary operator, $U(t, t_0)$. For a quantum state $|\psi(t_0)\rangle$ at time t_0 , the state evolution from t_0 to t is:

$$|\psi(t)\rangle = U(t, t_0) |\psi(t_0)\rangle, \quad (2.30)$$

where the state $\psi(t)$ obeys the Schrödinger equation with time-dependent Hamiltonian $H(t)$:

$$i\hbar \frac{d|\psi\rangle}{dt} = H(t) |\psi(t)\rangle, \quad (2.31)$$

and the unitary operator, $U(t, t_0)$, also follows the similar differential equation:

$$i\hbar \frac{dU(t, t_0)}{dt} = H(t)U(t, t_0). \quad (2.32)$$

If the Hamiltonian is time-independent, $H(t) = H$, then the unitary operator, $U(t, t_0)$, has an analytic form:

$$U(t, t_0) = e^{-\frac{i}{\hbar}(t-t_0)H}. \quad (2.33)$$

The expectation value of an operator A_0 can be represented as the following:

$$\begin{aligned} & \langle \psi_S(t) | A_S(t) | \psi_S(t) \rangle \\ &= \langle \psi(t) | A_0 | \psi(t) \rangle \\ &= \langle \psi(t_0) | U^\dagger A_0 U | \psi(t_0) \rangle. \end{aligned} \quad (2.34)$$

2.3.2 Heisenberg Picture

In the Heisenberg picture, it is the operators $A_H(t)$ evolving in time while the quantum states are stationary: $|\psi_H(t)\rangle = |\psi(t_0)\rangle$.

By using the constraint that the expectation value for the operator A is identical in any pictures:

$$\langle\psi_S(t)|A_S(t)|\psi_S(t)\rangle = \langle\psi_H(t)|A_H(t)|\psi_H(t)\rangle. \quad (2.35)$$

By expanding the left-hand side:

$$\begin{aligned} \langle\psi_S(t)|A_S(t)|\psi_S(t)\rangle &= \langle\psi(t_0)|U^\dagger(t, t_0)A_S(t)U(t, t_0)|\psi(t_0)\rangle \\ &= \langle\psi_H(t)|A_H(t)|\psi_H(t)\rangle. \end{aligned} \quad (2.36)$$

Therefore, we can conclude in the Heisenberg picture, the time evolved operator $A_H(t)$ is:

$$A_H(t) = U^\dagger(t, t_0)A_S(t)U(t, t_0). \quad (2.37)$$

Taking the time derivative of $A_H(t)$ yields:

$$\begin{aligned} \frac{dA_H}{dt} &= (\dot{U}^\dagger A_S U + U^\dagger \dot{A}_S U + U^\dagger A_S \dot{U}) \\ &= \frac{1}{i\hbar}(-U^\dagger H^\dagger A_S U + U^\dagger A_S H U) + U^\dagger \dot{A}_S U \\ &= \frac{1}{i\hbar}(U^\dagger[A_S, H]U) + U^\dagger \dot{A}_S U \\ &= \frac{1}{i\hbar}[A_H, H_H] + (\dot{A}_S)_H. \end{aligned} \quad (2.38)$$

By rearrange the above equation, we can get the Heisenberg evolution equation:

$$i\hbar \frac{dA_H(t)}{dt} = [A_H(t), H_H(t)] + i\hbar(\dot{A}_S)_H. \quad (2.39)$$

Taking the free field Hamiltonian, Eq. (2.11), as an example. After solving it by Heisenberg equation, we can get

$$a(t) = a(0)e^{-i\omega t}, \quad (2.40)$$

where $a(0)$ is the initial condition of $a(t)$. The linear combination of the above equation with its Hermitian conjugate provides

$$Q(t) = Q(0) \cos \omega t + P(0) \sin \omega t \quad (2.41)$$

$$P(t) = -Q(0) \sin \omega t + P(0) \cos \omega t, \quad (2.42)$$

where $Q(0)$ and $P(0)$ are the initial condition of $Q(t)$ and $P(t)$. Eq. (2.41) and (2.42) state that the quadrature operators precess sinusoidally in phase space at frequency ω under free field evolution. That is to say, equivalently under Schrodinger evolution, the state evolves by rotating between its quadratures. Moreover, a $\pi/2$ local phase shift, from $\omega t = \pi/2$, applied to the quadratures does the following.

$$Q \rightarrow P \quad (2.43)$$

$$P \rightarrow -Q. \quad (2.44)$$

In the experiment, we use a piezoelectric transducer (PZT) mounted mirror on the beam path to achieve the $\pi/2$ phase shift.

2.3.3 Interaction Picture

In the interaction picture (a.k.a. Dirac picture), the states and the operators evolve with time. Consider the Hamiltonian $H = H_0 + V$, where the first term H_0 is a single-system interaction, whereas the second term V is a coupling term between different systems. Generally, $[H_0, V] \neq 0$. There are two versions of the interaction picture:

- (i). the states evolve solely under V whereas the operators evolve solely under H_0 ;
- (ii). the operators evolve solely under V , whereas the states evolve solely under H_0 .

Version (i) is preferred in the atomic physics area, but version (ii) is favored in the quantum optics area. Therefore, we will only focus on version (ii) here.

We can find the interaction-picture operator by de-evolving under H_0 the fully evolved operator, i.e. $A_H(t)$, as the following:

$$A_I(t) = U_0 A_H(t) U_0^\dagger = e^{-iH_0 t} e^{iHt} A_S e^{-iHt} e^{iH_0 t}. \quad (2.45)$$

The time derivative of $A_I(t)$ gives:

$$\begin{aligned} \frac{dA_I(t)}{dt} &= \frac{d(U_0 A_H(t) U_0^\dagger)}{dt} \\ &= \dot{U}_0 A_H U_0^\dagger + U_0 \dot{A}_H U_0^\dagger + U_0 A_H \dot{U}_0^\dagger \\ &= -\frac{i}{\hbar} (H_0 U_0 A_H U_0^\dagger - U_0 A_H U_0 H_0) + U_0 \frac{dA_H}{dt} U_0^\dagger \\ &= \frac{i}{\hbar} [A_I, H_0] + U_0 \frac{dA_H}{dt} U_0^\dagger \\ &= \frac{i}{\hbar} [A_I, H_0] + U_0 \left(\frac{1}{i\hbar} [A_H, H_H] + (\dot{A}_S)_H \right) U_0^\dagger. \end{aligned} \quad (2.46)$$

Consider the typical case where H commutes with its derivative at different times, thus $H_H = H$, Eq.(2.46) becomes

$$\begin{aligned} \frac{dA_I(t)}{dt} &= \frac{i}{\hbar} ([A_I, H_0] - [A_I, H_0] - [A_I, U_0 V U_0^\dagger]) + U_0 (\dot{A}_S)_H U_0^\dagger \\ &= -\frac{i}{\hbar} [A_I, U_0 V U_0^\dagger] + U_0 (\dot{A}_S)_H U_0^\dagger. \end{aligned} \quad (2.47)$$

Eq. (2.47) is the time evolution equation for the operators in the interaction picture, and the evolution is under $V_I = U_0 V U_0^\dagger$ where V is in the Schrödinger picture. Note A_S is time-independent oftentimes.

Since the state evolved solely under H_0 , we have

$$|\psi_I(t)\rangle = U_0 |\psi(t_0)\rangle, \quad (2.48)$$

and its time derivative is

$$\begin{aligned} \frac{d|\psi_I(t)\rangle}{dt} &= \frac{dU_0|\psi(t_0)\rangle}{dt} \\ &= \frac{dU_0}{dt}|\psi(t_0)\rangle \\ &= \frac{i}{\hbar}H_0|\psi(t_0)\rangle. \end{aligned} \tag{2.49}$$

2.4 Quantum States

This section will introduce two commonly used quantum states, Fock states, and coherent states. Another important quantum state, squeezed states, will be presented later.

2.4.1 Fock States

As we discussed in Section 2.1, for quantized electromagnetic fields, we can use a quantum harmonic oscillator to describe it. Thus the radiation field has the eigenenergy $\hbar\omega(n + \frac{1}{2})$. Fock states (or number states) $|n\rangle$ are the corresponding eigenstates, and they are also eigenstates of the number operator

$$a^\dagger a |n\rangle = N |n\rangle = n |n\rangle, \tag{2.50}$$

where $N = a^\dagger a$ is the photon number operator.

The annihilation and creation operators applied on Fock states follow Eq. (2.7) and (2.8).

The ground state with zero photon number hence is also called vacuum state, which is defined by

$$a |0\rangle = 0. \tag{2.51}$$

For arbitrary Fock state with n photon number, it can be represented by the vacuum state and creation operator

$$|n\rangle = \frac{(a^\dagger)^n}{\sqrt{n!}} |0\rangle. \tag{2.52}$$

Fock states are orthogonal

$$\langle n|n'\rangle = \delta_{nn'}, \tag{2.53}$$

and complete

$$\sum_n |n\rangle \langle n| = \mathbb{1}, \tag{2.54}$$

where $\mathbb{1}$ is the identity operator.

Since a Fock state with photon number n has a precisely known number of photons, therefore the STD of photon number for Fock state is zero

$$\Delta N = \sqrt{(\langle n|N^2|n\rangle) - (\langle n|N|n\rangle)^2} = 0. \tag{2.55}$$

2.4.2 Coherent States

Coherent states $|\alpha\rangle$ are the most classical quantum states of a harmonic oscillator. The coherent state can well describe laser light because the coherent state has a more precisely defined phase. Thus, α is a complex number, and it can be represented by the following:

$$\alpha = |\alpha|e^{i\theta}. \quad (2.56)$$

A coherent state is the eigenstate of annihilation operator with eigenvalue α

$$a|\alpha\rangle = \alpha|\alpha\rangle, \quad (2.57)$$

this is due to the fact that a coherent state is a displaced vacuum state by α :

$$\begin{aligned} |\alpha\rangle &= D(\alpha)|0\rangle \\ &= e^{\alpha a^\dagger - \alpha^* a}|0\rangle \\ &= \exp\left(-\frac{|\alpha|^2}{2}\right) \sum_{n=0}^{\infty} \frac{\alpha^n}{\sqrt{n!}} |n\rangle, \end{aligned} \quad (2.58)$$

where $D(\alpha) = e^{\alpha a^\dagger - \alpha^* a}$ is the displacement operator.

The expectation value of the photon number operator is

$$\bar{n} = \langle\alpha|n|\alpha\rangle = |\alpha|^2, \quad (2.59)$$

and the expectation value of square of the photon number operator is

$$\langle\alpha|n^2|\alpha\rangle = |\alpha|^2 + |\alpha|^4. \quad (2.60)$$

Therefore, the STD of the photon number operator is

$$\Delta n = \sqrt{(\langle\alpha|n^2|\alpha\rangle) - (\langle\alpha|n|\alpha\rangle)^2} = |\alpha|^2 = \bar{n}. \quad (2.61)$$

For a photon number measurement in the field, the probability of detecting n photon is a Poisson distribution with a mean of \bar{n}

$$\begin{aligned} P_n &= |\langle n|\alpha\rangle|^2 = e^{-|\alpha|^2} \frac{|\alpha|^{2n}}{n!} \\ &= e^{-\bar{n}} \frac{\bar{n}^n}{n!}. \end{aligned} \quad (2.62)$$

On the other hand, the STD of the Q and P are

$$\Delta Q = \sqrt{(\langle\alpha|Q^2|\alpha\rangle) - (\langle\alpha|Q|\alpha\rangle)^2} = \frac{1}{\sqrt{2}}, \quad (2.63)$$

$$\Delta P = \sqrt{(\langle\alpha|P^2|\alpha\rangle) - (\langle\alpha|P|\alpha\rangle)^2} = \frac{1}{\sqrt{2}}, \quad (2.64)$$

which is the same as a vacuum state Eq. (2.28), but the average photon number is nonzero. This is the reason why a coherent state is a displaced vacuum state.

2.5 Beam Splitter

A beam splitter (BS) is a passive optics where one side of the surface has an anti-reflection coating, and the other side of the surface has a reflective coating, so we can only consider it a single interface. From a classical optics point of view, when a single stream of light enters a beam splitter, part of the light will be reflected, and part will be transmitted. From quantum optics point of view: a BS always has two input ports and two output ports, and what a beam splitter does is mix/interfere with the two input lights. For a single stream of light entering a BS, the other unused port still has a vacuum mode that can come in, and the BS will interfere with the incident light with vacuum mode.

We can use a 2×2 matrix to describe a lossless BS with electric field amplitude reflection coefficient ρ and transmission coefficient τ . The figure 2.1 illustrates a BS with two input modes and two output modes. The output modes are related to the input modes as (in the interaction picture):

$$\begin{pmatrix} c \\ d \end{pmatrix} = \begin{pmatrix} \rho & \tau \\ \tau & -\rho \end{pmatrix} \begin{pmatrix} a \\ b \end{pmatrix}. \quad (2.65)$$

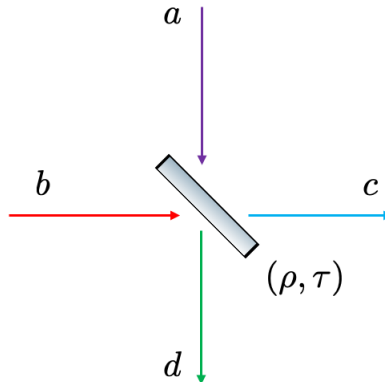


Figure 2.1: BS with two input modes and two output modes

For the classical input light, say input light a , it can be represented by $|\alpha|e^{i\theta_a}$, where $|\alpha|$ is the field amplitude and θ_a is the field phase. For the quantum input mode, the input mode a is the field operator. Note one can choose different kinds of BS matrices as long as the matrices are unitary, such that the total energy (total photon number) is conserved.

As the interference is based on the wave feature of light, another interesting interpretation about BS is based on the particle feature of light. Consider a single photon enters a BS with electric field amplitude reflection coefficient ρ and transmission coefficient τ , it actually implies the photon has a probability of ρ^2 to be reflected and probability of τ^2 to be transmitted.

One can also use the BS Hamiltonian in the interaction picture to find the unitary operator of BS [10, 28, 55]. The BS Hamiltonian used in the Heisenberg equation, Eq. (2.47), is

$$V_{BS} = \frac{i\hbar}{2}(a^\dagger b e^{-i\theta} - ab^\dagger e^{i\theta}), \quad (2.66)$$

where $a=a(0)$ and $b=b(0)$ are the two input ($t=0$) mode operators and θ is related to the reflectivity of the beam splitter. By applying the Eq. (2.47) to the BS Hamiltonian, one can find the evolved modes $d=a(t)$ and $c=b(t)$ due to the BS. Note the parameter t here is fixed and is simply equal to the BS interaction time, i.e. t is contained in the ρ and τ in the BS matrix, Eq. (2.65), which is just like the parameter r in the squeezing, which will be discussed in the next section, section 2.6.

2.6 Squeezing Generation, Detection, and Degradation

In this section, I will discuss a quantum phenomenon - squeezing. To observe squeezing, which is noise reduction, we first need to prepare the squeezed states via a nonlinear interaction. And then, I will talk about how we observe squeezing, i.e. by using homodyne detection. Finally, I will discuss two important factors that affect the amount of observed squeezing.

2.6.1 Single-Mode Squeezing

Let's consider the following Hamiltonian in the interaction picture:

$$H = \frac{i\hbar}{2}(\chi b a^{\dagger 2} - \chi^* b^\dagger a^2), \quad (2.67)$$

where $\chi = \chi^{(2)}$ is a second-order nonlinear susceptibility, b is the annihilation operator for the pump mode and a is the annihilation operator for the signal mode.

Eq. (2.67) describes a parametric process that converts pump fields with higher frequency 2ω into two identical signal fields with frequency ω , and this process is known as degenerate parametric down-conversion. Eq. (2.67) also describes the reverse process, known as degenerate parametric up-conversion. In the experiment, we operate a device called optical parametric oscillator (OPO) by sending the pump beam into the device with its power right below the lasing threshold. Thus, it initiates a process called spontaneous parametric down-conversion (SPDC). (The detail of OPO will be covered in a later chapter.)

By solving the Heisenberg equation, Eq. (2.39), taking χ as a real number, and assuming the pump beam is a strong coherent classical field (thus undepleted),

$$b \rightarrow |\beta| e^{i\phi}, \quad (2.68)$$

where β is the field amplitude of pump beam and ϕ is the phase of the pump (Note actually, ϕ is the relative phase between pump field and two signal fields, i.e., $\phi_p - 2\phi_s = \phi$, but here we take $\phi_s = 0$). We can get the so-called Bogoliubov transformation

$$a(t) = S^\dagger(r, \phi) a S(r, \phi) = a \cosh r + a^\dagger e^{i\phi} \sinh r, \quad (2.69)$$

where $r = \chi|\beta|t$ is the squeezing parameter and $S(r, \phi)$ is the squeezing operator

$$S(r, \phi) = e^{\frac{r}{2}(a^\dagger{}^2 e^{i\phi} - a^2 e^{-i\phi})}. \quad (2.70)$$

Then the linear combination of Eq. (2.69) and its Hermitian conjugate provides

$$a(t)^\dagger e^{i\frac{\phi}{2}} + a(t)e^{-i\frac{\phi}{2}} = e^r (a^\dagger e^{i\frac{\phi}{2}} + a e^{-i\frac{\phi}{2}}), \quad (2.71)$$

$$a(t)^\dagger e^{i(\frac{\phi}{2} + \frac{\pi}{2})} + a(t)e^{-i(\frac{\phi}{2} + \frac{\pi}{2})} = e^{-r} (a^\dagger e^{i(\frac{\phi}{2} + \frac{\pi}{2})} + a e^{-i(\frac{\phi}{2} + \frac{\pi}{2})}). \quad (2.72)$$

Define a generalized quadrature as

$$A(\theta, t) = a(t)^\dagger e^{i\theta} + a(t)e^{-i\theta}, \quad (2.73)$$

where $\theta = \frac{\phi}{2}$. The generalized quadratures can also be represented by two quadratures as

$$A(\theta, t) = Q(t) \cos \theta + P(t) \sin \theta. \quad (2.74)$$

The evolution of two quadratures can be found at $\theta = 0$ and $\frac{\pi}{2}$:

$$A(0, t) = Q(t) = Qe^r, \quad (2.75)$$

$$A(\frac{\pi}{2}, t) = P(t) = Pe^{-r}. \quad (2.76)$$

With the aid of Eq. (2.24), we can find out the STD of them:

$$\Delta Q = \frac{e^r}{\sqrt{2}}, \quad (2.77)$$

$$\Delta P = \frac{e^{-r}}{\sqrt{2}}, \quad (2.78)$$

and their product saturates the HUP:

$$\Delta Q \Delta P = \frac{1}{2}. \quad (2.79)$$

For Eqs. (2.77) and (2.78), the squeezing parameter plays an important role. When $r = 0$ (the condition of no pump beam), Eqs. (2.77) and (2.78) become the STD of vacuum state. As r increases, the STD of phase quadrature P decreases while at the same time the STD of amplitude quadrature Q increases, but their product still remains the same. Thus, the squeezing is a process to turn the uncertainty circle (from vacuum state) into an ellipse (that's why the state is called a single-mode squeezed vacuum state), such that one quadrature has smaller noise while increasing the noise on the other quadrature.

2.6.2 Two-Mode Squeezing

For the parametric process, the two signal fields don't have to be identical in general (nondegenerate), as long as the energy conservation and momentum conservation hold. The two signal fields, one is called the signal field, and the other is called the idler field. Now, we can consider the following Hamiltonian in the interaction picture

$$H = i\hbar(\chi b a_s^\dagger a_i^\dagger - \chi^* b^\dagger a_s a_i), \quad (2.80)$$

where χ is a second-order nonlinear susceptibility, b is annihilation operator for the pump mode, a_s is the annihilation operator for the signal mode and a_i is the annihilation operator for the idler mode.

As we did for the single-mode squeezing case, we can solve the Heisenberg equation, Eq. (2.39), by taking χ as a real number, and assuming the pump beam is a strong coherent classical field (thus undepleted), $b = |\beta|e^{i\phi}$, we then obtain

$$a_s(t) = a_s \cosh r + a_i^\dagger \sinh r, \quad (2.81)$$

$$a_i(t) = a_i \cosh r + a_s^\dagger \sinh r, \quad (2.82)$$

which is the two mode squeezing Bogoliubov transformation.

The squeezing and antisqueezing appear as we convert the Eq. (2.81) and (2.82) into the amplitude quadrature and phase quadrature:

$$Q_+(r) = Q_s(r) + Q_i(r) = (Q_s + Q_i)e^r, \quad (2.83)$$

$$P_+(r) = P_s(r) + P_i(r) = (P_s + P_i)e^{-r}, \quad (2.84)$$

$$Q_-(r) = Q_s(r) - Q_i(r) = (Q_s - Q_i)e^{-r}, \quad (2.85)$$

$$P_-(r) = P_s(r) - P_i(r) = (P_s - P_i)e^r. \quad (2.86)$$

Note Eq. (2.84) and (2.85) are called variance-based entanglement witnesses[27] or nullifiers.

The corresponding STD are

$$\Delta Q_+(r) = e^r, \quad (2.87)$$

$$\Delta P_+(r) = e^{-r}, \quad (2.88)$$

$$\Delta Q_-(r) = e^{-r}, \quad (2.89)$$

$$\Delta P_-(r) = e^r. \quad (2.90)$$

The Eq. (2.88) implies P_s and P_i are anticorrelated while the Eq. (2.89) implies Q_s and Q_i are correlated, and the amount of correlation/anti-correlation is determined by the squeezing parameter r . This quantum correlation is, in fact, entanglement. Figure 2.2a and 2.2b show the STD of ΔP_+ and ΔQ_- . Three different squeezing parameters are considered. Purple dashed circle: when $r = 0$, the STD is the same as the vacuum fluctuation, and there is no correlation (anticorrelation) between Q_s and Q_i (P_s and P_i). Red line: when $r \rightarrow \infty$, the STD of ΔP_+ and ΔQ_-

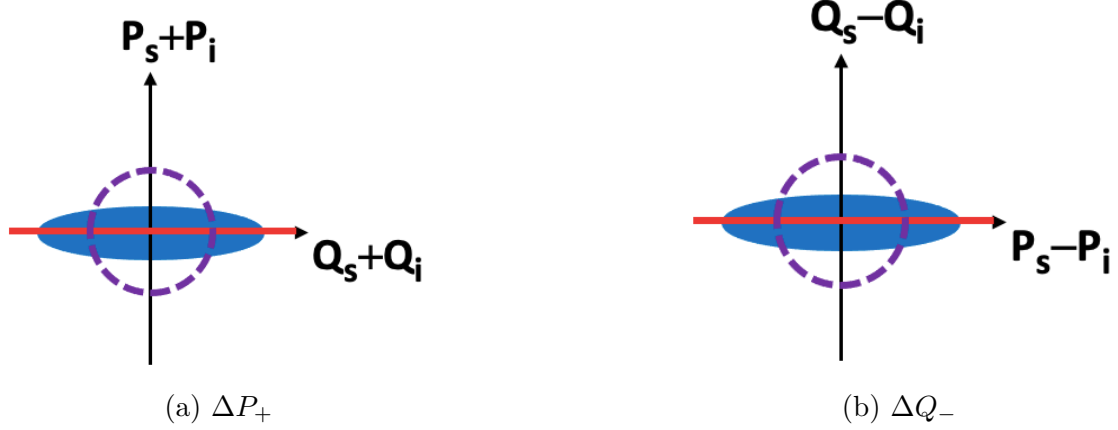


Figure 2.2: Phase diagram for the two-mode squeezed state. The purple dashed circle represents vacuum fluctuation, the blue ellipse represents the finite squeezing case, and the red line represents the infinite squeezing case.

becomes zero. Therefore, Q_s and Q_i are perfectly correlated (P_s and P_i are perfectly anticorrelated). This is the case of Einstein-Podolski-Rosen (EPR) state [16], which is the continuous variable version of Bell state (see next chapter for detail). However, infinite squeezing requires infinite pump energy, which is impossible to achieve. Blue ellipse: r is finite, the STD is squeezed for ΔQ_- and ΔP_+ compared to the vacuum fluctuation. Therefore, the two-mode squeezing is the best practical realization of the EPR state in the experiment.

2.6.3 Squeezing Detection: Balanced Homodyne Detection

To detect the squeezing, we need to use a special type of measurement scheme, balanced homodyne detection (BHD). Figure 2.3 illustrates the setup, and the principle is the following: preparing a classical coherent state of light b , so-called optical local oscillator (LO), and interfering LO with the target light a by a 50:50 BS. The target light can be a vacuum state or squeezed state. Collect the two output beams after the BS, c and d , by using two photodiodes and then send the photocurrent difference signal to a spectrum analyzer to observe the noise.

Mathematically, by using Eq. (2.65) (or by solving the Heisenberg equation of Eq. (2.66)) with $\rho = \tau = \frac{1}{\sqrt{2}}$, the out modes, c and d , are related to the input modes, a and b , as the following:

$$c = \frac{1}{\sqrt{2}}(a + b), \quad (2.91)$$

$$d = \frac{1}{\sqrt{2}}(a - b). \quad (2.92)$$

Thus, the photocurrent difference is

$$\begin{aligned} N_- &= N_c - N_d = c^\dagger c - d^\dagger d = a^\dagger b + b^\dagger a \\ &= |\beta|(a^\dagger e^{i\theta} + a e^{-i\theta}) = |\beta|A(\theta) \\ &= |\beta|(P \cos \theta + Q \sin \theta), \end{aligned} \quad (2.93)$$

with classical LO, $b = |\beta|e^{i\theta}$ been employed, where $|\beta|$ is LO electric field magnitude, θ is the relative optical phase difference between LO and target light, and $A(\theta)$ is the

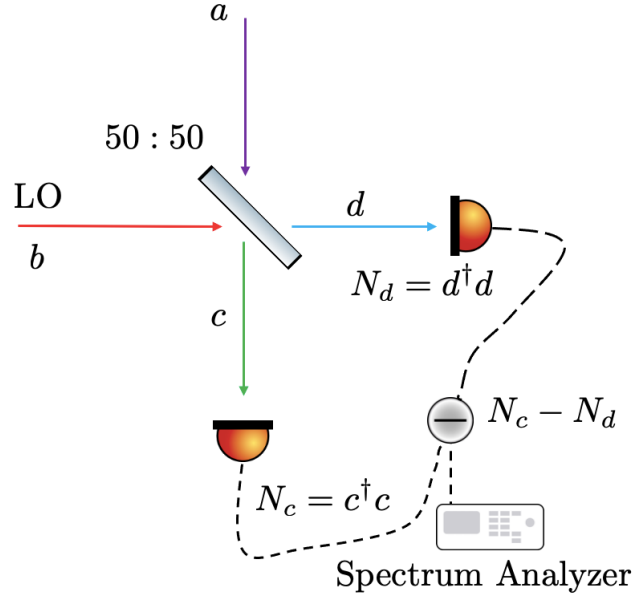


Figure 2.3: Set up for the balanced homodyne detection

generalized quadrature. Note the generalized quadrature $A(\theta)$ is amplified by strong LO field amplitude $|\beta|$ and we now have the ability to measure the quadrature from $\theta = 0$ to 2π . With squeezing, the two quadratures is $P \rightarrow Pe^{-r}$ and $Q \rightarrow Qe^r$. Therefore, the photocurrent difference becomes

$$N_- = |\beta|(Pe^{-r} \cos \theta + Qe^r \sin \theta). \quad (2.94)$$

Experimentally, the optical phase difference, θ , can be introduced by setting a piezoelectric (PZT) mounted mirror on the target light path or LO path with a ramp or triangular wave signal with a known frequency.

The STD of photocurrent difference is

$$\Delta N_- = |\beta| \sqrt{e^{-2r} + 2 \sinh[2r](\sin \theta)^2}, \quad (2.95)$$

but what is measuring by the spectrum analyzer is the power spectrum in decibel (dB) units, thus the squeezing in dB is defined as

$$s(r, \theta) = 20 \log_{10} \frac{\Delta N_-(r)}{\Delta N_-(r=0)}, \quad (2.96)$$

which implies the squeezing is normalized to the noise of vacuum.

Figure 2.4 shows the squeezing traces. The vertical axis is variance in dB, and the horizontal axis is relative phase θ in radiant. Different color of lines represents different squeezing parameters. For $r = 0$, which provides the variance of the vacuum state, a.k.a. shot noise, and the variance is independent of θ . When $r \neq 0$, the variance depends on θ and r : as θ changes, the variance can become larger or smaller than the shot noise, and the minimal (maximal) variance is the largest squeezed (antisqueezed) can be obtained; as r increases, the maximal values of squeezing and antisqueezing also increase.

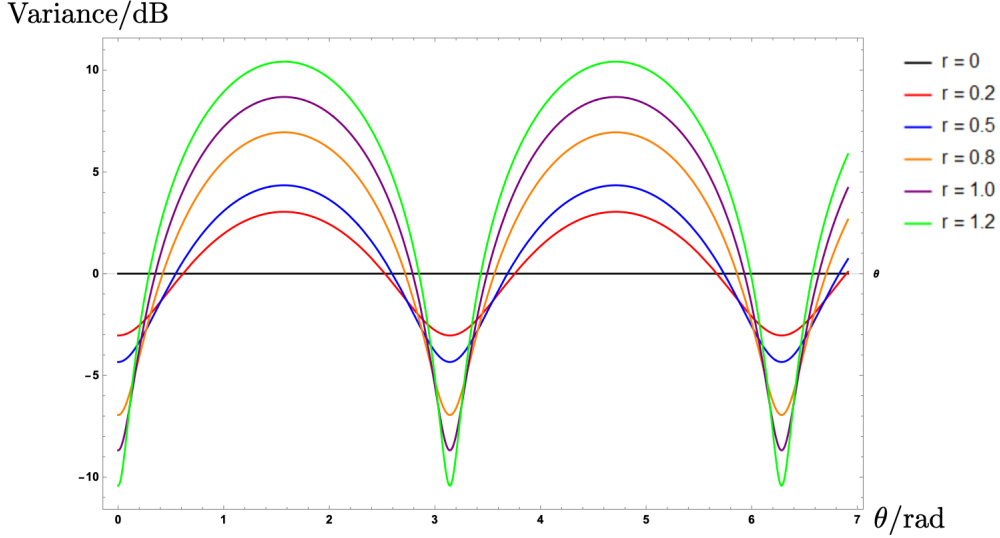


Figure 2.4: Squeezing traces: the variance changes with the relative phase θ and squeezing parameter r .

2.6.4 Squeezing Degradation - Phase Noise and Loss

Squeezed light is quite fragile, and there are two important factors that will affect the amount of observed squeezing: phase noise and loss.

Phase noise: When phase noise exists inside an optical system, if the phase noise has a frequency larger than the inverse of acquisition time of the detector or spectrum analyzer, then the maximal squeezing will be mixed with less squeezing part and thus reduce the amount of observed squeezing. We can measure the phase noise from an interference measurement. Considering the case when two fields are mode matched, we can observe the interference fringe by a power meter, and the observed signal is

$$\begin{aligned}
 I &= |E_1 e^{i(\omega_1 t + \phi_1)} + E_2 e^{i(\omega_2 t + \phi_2)}|^2 \\
 &= |E_1|^2 + |E_2|^2 + 2|E_1 E_2| \cos [(\omega_1 - \omega_2)t + (\phi_1 - \phi_2)] \\
 &= I_1 + I_2 + 2\sqrt{I_1 I_2} \cos [(\omega_1 - \omega_2)t + (\phi_1 - \phi_2)],
 \end{aligned} \tag{2.97}$$

where E_i is the electric field amplitude for field i , $I_i = |E_i|^2$ is the intensity for field i , ω_i is the frequency of field i , ϕ_i is the initial phase of field i , and $i \in [1, 2]$. The amplitude envelope of the oscillating intensity is

$$A = I_{max} - I_{min} = 2\sqrt{I_1 I_2} \tag{2.98}$$

and the average intensity is

$$\bar{I} = I_{max} + I_{min} = I_1 + I_2. \tag{2.99}$$

Figure 2.5 shows an interference fringe without the phase noise looks like with maximal, minimal, and average value denoted.

To find out the phase noise, we can simplify the Eq. (2.97) by considering the two fields are ideally monochromatic, $\omega_2 = \omega_1$. Suppose we introduce a relative

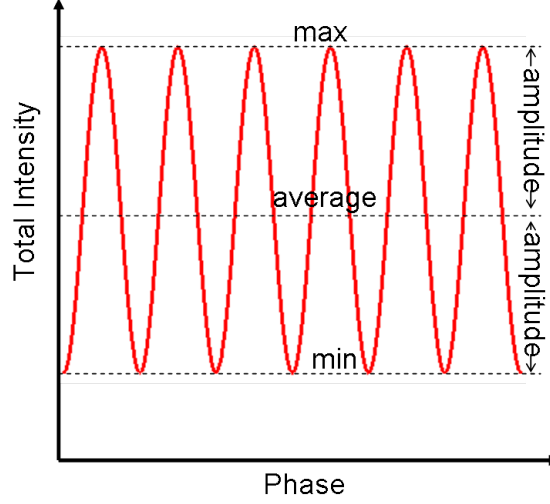


Figure 2.5: Interference fringe without the phase noise. (from Wikipedia).

phase changing (say from a PZT mounted mirror in the optical pass of field 1) and assume a phase noise, $\delta\phi$, exists, the Eq. (2.97) can be written as

$$\begin{aligned}
 & I_1 + I_2 + 2\sqrt{I_1 I_2} \cos [\Omega t + \delta\theta] \\
 & \rightarrow I_1 + I_2 + 2\sqrt{I_1 I_2} [\cos (\Omega t) \cos \delta\theta + \sin (\omega t) \sin \delta\theta] \quad (2.100) \\
 & \xrightarrow{\delta\theta \ll 1} I_1 + I_2 + 2\sqrt{I_1 I_2} [\cos (\Omega t) + \sin (\Omega t) \delta\theta],
 \end{aligned}$$

where Ω is the frequency of phase changing introduced by a PZT mounted mirror. In the equation above, we take the assumption of the $\delta\theta$ is small and the approximation in the last two steps. Eq. (2.100) implies we can measure the effect of phase noise from the interference fringe, I_{phase} , at the place $\cos (\Omega t) = 0$, which is the average value of the interference fringe, we then obtain

$$\begin{aligned}
 I_{phase} &= I_1 + I_2 + 2\sqrt{I_1 I_2} \delta\theta \\
 &= \bar{I} + A\delta\theta.
 \end{aligned} \quad (2.101)$$

Rearrange the above equation, and we can get

$$\delta\theta = \frac{I_{phase} - \bar{I}}{A} = \frac{I_{pp}^{noise}}{2A}, \quad (2.102)$$

where I_{pp}^{noise} is the peak to peak value of noise measured at the average of fringe, see figure 5.3 for an example. Note the phase noise $\delta\theta$ is in units of radian. Actually, the phase noise is also a function of time, therefore the phase noise can be written as

$$\delta\theta \rightarrow \sum_i \delta\theta_i \sin \Omega_i t, \quad (2.103)$$

where δ_i is the amplitude of phase noise i and Ω_i is the frequency of phase noise i . However, when the interference fringe contains only one or two phase noises, we still can use Eq. (2.102) to estimate the amplitude of phase noise.

The effect of phase noise on the squeezing can be estimated by using Eq. (2.93). When phase noise doesn't exist, the photocurrent difference for squeezed quadrature is at $\theta = 0$

$$N_- = |\beta| (P e^{-r} \cos 0 + Q e^r \sin 0) = |\beta| P e^{-r}. \quad (2.104)$$

The photocurrent difference for squeezed quadrature when phase noise exists becomes

$$\begin{aligned} N_-^{noise} &= |\beta|(Pe^{-r} \cos(0 + \delta\theta) + Qe^r \sin(0 + \delta\theta)) \\ &= |\beta|(Pe^{-r} \cos(\delta\theta) + Qe^r \sin(\delta\theta)), \end{aligned} \quad (2.105)$$

and the corresponding STD of photocurrent difference is

$$\Delta N_-^{noise} = |\beta|\sqrt{e^{-2r} + 2 \sinh[2r](\sin \delta\theta)^2}, \quad (2.106)$$

which is in the same form as Eq. (2.95). Therefore, by regarding the relative phase as phase noise, the figure 2.4 can be understood as the effect of phase noise on the squeezing. As an example, when $r = 1.2$, the maximal amount of squeezing is about -10.4 dB if there is no phase noise. With phase noise $6^\circ = 0.1$ rad, the observed squeezing dropped to -6.8 dB.

Loss: When there is a loss in the squeezed light path, the maximal amount of observed squeezing will also drop. There are two ways to understand the effect of the loss on squeezing. The first point of view is a loss causes some of the photons lost, so the detector can't catch all the correlated photons. Thus, the observed squeezing will drop. The second point of view is the loss introduces a channel such that a vacuum state can come in and mix with the squeezed state. As we discussed before, a vacuum state has zero photons but still has noise. Therefore, the observed squeezing will drop. Figure 2.6 illustrates these two points of view about the loss.

We can use a BS with electric field amplitude reflection coefficient ρ and transmission coefficient τ to model the loss, i.e. $\rho = 0$ means no loss and $\rho = 1$ means all the light is missed. Here, I will use the second point of view about the loss to do the estimation. The squeezed state is denoted as a , and the vacuum mode is denoted as b . The STD of the mode's two quadratures after the BS becomes

$$\begin{aligned} \Delta P_{out} &= (\langle 00 | (\rho \Delta P_a + \tau \Delta P_b)^2 | 00 \rangle)^{1/2} \\ &= \Delta P_b \sqrt{\rho^2 + \tau^2 e^{2r}} \geq \Delta P_b, \end{aligned} \quad (2.107)$$

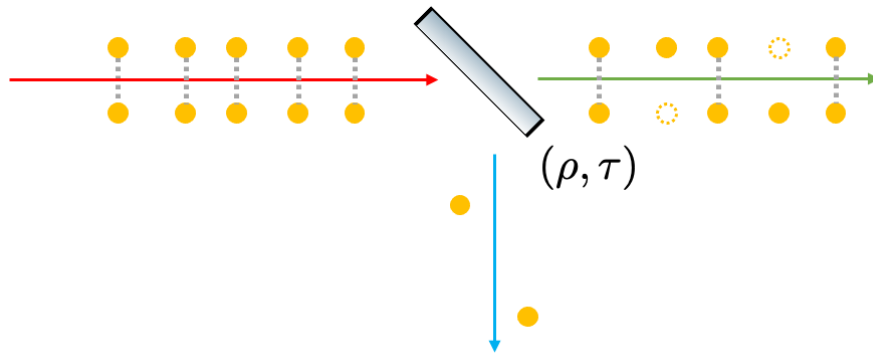
$$\begin{aligned} \Delta Q_{out} &= (\langle 00 | (\rho \Delta Q_a + \tau \Delta Q_b)^2 | 00 \rangle)^{1/2} \\ &= \Delta Q_b \sqrt{\rho^2 + \tau^2 e^{-2r}} \leq \Delta Q_b. \end{aligned} \quad (2.108)$$

Hence, Eq. (2.107) and Eq. (2.108) provide how the maximal antisqueezing and squeezing are affected by the loss. Convert them into variance in dB units and normalize to vacuum noise

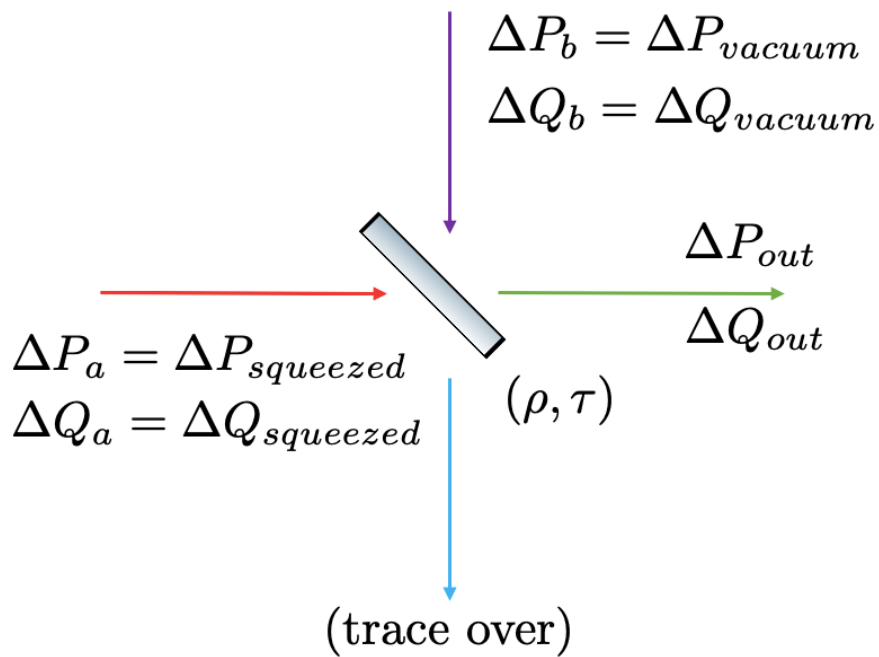
$$s(r, \tau) = 20 \log_{10} \frac{\Delta P_{out}(r)}{\Delta P_{out}(r=0)}, \quad (2.109)$$

$$as(r, \tau) = 20 \log_{10} \frac{\Delta Q_{out}(r)}{\Delta Q_{out}(r=0)}, \quad (2.110)$$

where $s(r, \tau)$ is squeezing and $as(r, \tau)$ is antisqueezing. As Figure 2.7 shows the loss degrades the maximal amount of observed squeezing and antisqueezing. Hence, it is very important to minimize the loss in the experiment. Besides, figure 2.7 also reveals the squeezing and anti-squeezing have different sensitivity to loss.



(a) Loss causes degradation to photon correlations.



(b) Loss introduces a channel for the vacuum to come in

Figure 2.6: Two-point of view about how the loss degrades the maximal amount of observed squeezing.

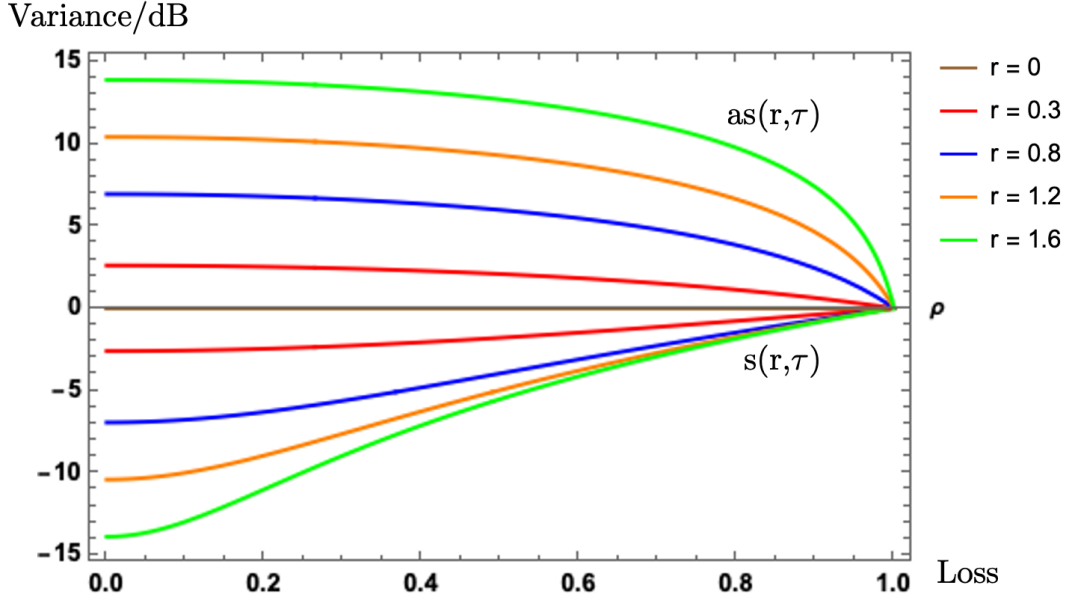


Figure 2.7: Loss degrades the maximal amount of observed squeezing and anti-squeezing.

Note when using the balanced homodyne detection, there are two factors that introduced the loss: inefficient photodiodes and mode mismatch in the balanced homodyne measurement.

Inefficient Photodiode: When observing squeezing by a photodiode with quantum efficiency, η_d , which is less than 100%, the observed squeezing will drop. One can understand this result by modeling a nonideal photodiode as the following: a BS with intensity transmission $T = \eta_d$ placed in front of an ideal photodiode with 100% quantum efficiency. Such BS couples the quantum light and vacuum modes before entering the ideal photodiodes. Therefore, it is desired to use a photodiode with quantum efficiency as perfect as possible, such that the observed squeezing degrades as little as possible.

Mode Mismatch: When aligning the optical LO and target light to the balanced homodyne detector, it is very crucial to mode match one to the other. Mode matching of the two fields requires them to have identical polarization and the same spatial modes. Once again, we can use a BS with transmission coefficient η and reflective coefficient $\sqrt{1 - \eta^2}$, where $\sqrt{1 - \eta^2}$ also represents the fraction of mismatch. We can measure the interference quality by defining the visibility as a ratio of the amplitude envelope of the oscillating intensity and the average intensity

$$\begin{aligned} VIS &= \frac{A}{\bar{I}} \\ &= \frac{I_{max} - I_{min}}{I_{max} + I_{min}}. \end{aligned} \quad (2.111)$$

$$VIS = \eta, \quad (2.112)$$

where I_{max} and I_{min} are the maximal and minimal of the interference fringe.

In fact, when two fields have different optical intensity, I_1 and I_2 , the ideal visibility is given by

$$VIS_{ideal} = \frac{2\sqrt{I_1 I_2}}{I_1 + I_2}. \quad (2.113)$$

Therefore, the visibility can be calibrated by the following

$$VIS_{cal} = \frac{VIS}{VIS_{ideal}}. \quad (2.114)$$

Without showing the detail, the balanced homodyne efficiency of the system is given by

$$\eta_{\text{BHD}} = (VIS_{cal})^2. \quad (2.115)$$

Remark: In fact, in the experiment, the power of quantum light is about a few nW, which requires a special photodiode with very high sensitivity to directly detect it. However, we can use the transmitted beam of the OPO, which has the identical polarization and spatial mode as the quantum light, to find out the balanced homodyne efficiency, which is the same as the case of quantum light.

Escape efficiency: We define a parameter, η_{esc} , as the escape efficiency, and it is defined as the following

$$\eta_{esc} = \frac{T}{T + L}, \quad (2.116)$$

where T is the cavity OC's transmittance, and L is the round-trip loss (for one-sided cavity). The larger the escape efficiency, the more light can come out from the cavity, and thus less consumed by the intra-cavity loss.

Total Detection Efficiency: Consider all the effects related to the loss, we can define a total detection efficiency as the following [56]:

$$\eta_{total} = \eta_d \times \eta_{esc} \times \eta_{\text{BHD}}. \quad (2.117)$$

Therefore, to estimate the squeezing after the effect of the loss by Eq. (2.107) and (2.108), we can use the η_{total} as τ^2 in the equations.

Chapter 3

Generating the 1-d, 2-d, and 3-d Cluster States by a Phase Modulated Quantum Optical Frequency Comb

In this chapter, I will cover two main topics, one topic is cluster states, and the other topic is cluster state generation in the phase-modulated two-mode squeezed quantum optical frequency comb (QOFC). The details about generating QOFC by an optical parametric oscillator will be covered in the next chapter.

3.1 Introduction of Measurement-Based Quantum Computing (MBQC) and the Cluster States

In this section, a brief introduction of measurement-based quantum computing (MBQC) and cluster states will be given. The major references I am using are Prof. Oliver Pfister's review paper [44] and the "Hypercubic cluster states in the phase-modulated quantum optical frequency comb" paper [70].

3.1.1 Bits, Qubits, and Qumodes

As classical computers use (binary) bits to encode the information, quantum computers use qubits to encode the information. While a binary bit can only be either 0 or 1, a qubit is a superposition of $|0\rangle$ and $|1\rangle$, such as a spin- $\frac{1}{2}$ particle. When encoding the information to the light, the qubit counterpart in quantum optics is called qumode [31]. The qumodes, $\{|q\rangle\}_{q \in \mathbb{R}}$, which are the eigenstates of position operator, Eq. (2.2), in 1-dimensional case:

$$Q|q\rangle = q|q\rangle, \quad (3.1)$$

and $\{|q\rangle\}_{q \in \mathbb{R}}$ is a continuous spectrum of states in contrast to qubit whose basis is discrete. Therefore, the quantum computing (QC) performed by using qumodes is called continuous-variable quantum computing (CVQC), while performed by qubits is called discrete-variable quantum computing (DVQC). There is a correspondence between qubit- and qumode-based quantum computing and is shown in table 3.1.

3.1. INTRODUCTION OF MEASUREMENT-BASED QUANTUM COMPUTING (MBQC) AND THE CLUSTER STATES

Note the capital letters stand for operators, and lower case letters stand for numbers. Also note the special symbol in table 3.1, \oplus , in the Pauli group means addition the modulo 2.

Qubit-based	Qumode-based
<u>Computational basis</u>	
$\{ 0\rangle, 1\rangle\}$ $\langle k l\rangle = \delta_{kl}, k, l \in \{0, 1\}$ $ \psi\rangle = \psi_0 0\rangle + \psi_1 1\rangle$	$\{ q\rangle\}_{q \in \mathbb{R}}$ $\langle q q'\rangle = \delta(q - q'), q, q' \in \mathbb{R}$ $ \psi\rangle = \int dq \psi(q) q\rangle$
<u>Conjugate basis</u>	
Hadamard transformed $ \pm\rangle = \frac{1}{\sqrt{2}}(0\rangle \pm 1\rangle)$	Fourier transformed $ p\rangle = \frac{1}{\sqrt{2\pi}} \int e^{ipq} q\rangle dq, p \in \mathbb{R}$
<u>Single-qubit/qumode group generators</u>	
Pauli group $\langle X, Z \rangle$ $X j\rangle = j \oplus 1\rangle, j = 0, 1$ $Z j\rangle = e^{ij\pi} j\rangle, j = 0, 1$ $X \pm\rangle = \pm \pm\rangle$ $Z \pm\rangle = \mp\rangle$	Weyl-Heisenberg group of phase-space displacements $\langle \{X(\xi)\}_{\xi \in \mathbb{R}}, \{Z(\varpi)\}_{\varpi \in \mathbb{R}} \rangle \equiv \langle \{e^{-i\xi P}\}_{\xi \in \mathbb{R}}, \{e^{i\varpi Q}\}_{\varpi \in \mathbb{R}} \rangle$ $X(\xi) q\rangle = q + \xi\rangle$ $Z(\varpi) q\rangle = e^{i\varpi q} q\rangle$ $X(\xi) p\rangle = e^{-i\xi p} p\rangle$ $Z(\varpi) p\rangle = p + \varpi\rangle$
<u>Controlled, entangling gates</u>	
$C_X j\rangle_1 k\rangle_2 = j\rangle_1 k \oplus j\rangle_2$	$C_X q\rangle_1 q'\rangle_2 = e^{-iQ_1 P_2} q\rangle_1 q'\rangle_2 = q\rangle_1 q' + \alpha q\rangle_2$
$C_Z j\rangle_1 k\rangle_2 = e^{i\pi j k} j\rangle_1 k\rangle_2$	$C_Z q\rangle_1 q'\rangle_2 = e^{iQ_1 Q_2} q\rangle_1 q'\rangle_2 = e^{iq_1 q'} q\rangle_1 q'\rangle_2$
<u>Bipartite entanglement</u>	
Bell state (unnormalized) $ B_{00}\rangle_{12} = \sum_{j=0}^1 j\rangle_1 j\rangle_2$	EPR state (unnormalizable) $ EPR(0, 0)\rangle_{12} = \int q\rangle_1 q\rangle_2 dq = \int p\rangle_1 -p\rangle_2 dp$ $= \sum_{n=0}^{\infty} n\rangle_1 n\rangle_2$ (Schmidt decomp.)
Bell basis $ B_{kl}\rangle_{12} = Z_1^k X_1^l B_{00}\rangle_{12}, k, l \in \{0, 1\}$ $= \sum_{j=0}^1 e^{ik\pi(j \oplus l)} j \oplus l\rangle_1 j\rangle_2$	EPR basis $ EPR(\varpi, \xi)\rangle_{12} = Z_1(\varpi) X_1(\xi) EPR(0, 0)\rangle_{12}, \varpi, \xi \in \mathbb{R}$ $= \int e^{i\varpi(q+\xi)} q + \xi\rangle_1 q\rangle_2 dq$

Table 3.1: Correspondence between qubit- and qumode-based quantum computing [4, 44].

3.1.2 Measurement-Based Quantum Computing

The idea of measurement-based QC was proposed by Rober Raussendorf and Hans J. Briegel in 2001 [49]. Measurement-based QC is a universal and equivalent alternative to the circuit model QC [40]. Figure 3.1a shows an example of circuit-based QC: quantum circuit for teleporting a qubit. The two top lines represent Alice's system, while the bottom line is Bob's system. The meters represent measurement,

and the double lines coming out of them carry classical bits.

To perform measurement-based QC, a special type of quantum state need to be prepared, which is a cluster state. A cluster state is an entangled qubit lattice that contains all the required entanglement for a quantum algorithm. Thus cluster state reacts as a computing substrate. The computation is carried out solely by single-qubit measurements with feedforward (quantum teleportation). Hence measurement-based QC is also called "one-way" QC: the state can be used only once, and irreversible project measurements drive the information flow [9]. Figure 3.1b shows an example of measurement-based QC. Before the measurements, the cluster state is in a square grid structure. Circles \odot symbolize measurements of Z to remove the qubit measured from cluster state, vertical arrows are measurements of X to propagate the information, while tilted arrows refer to measurements in the x - y plane [49].

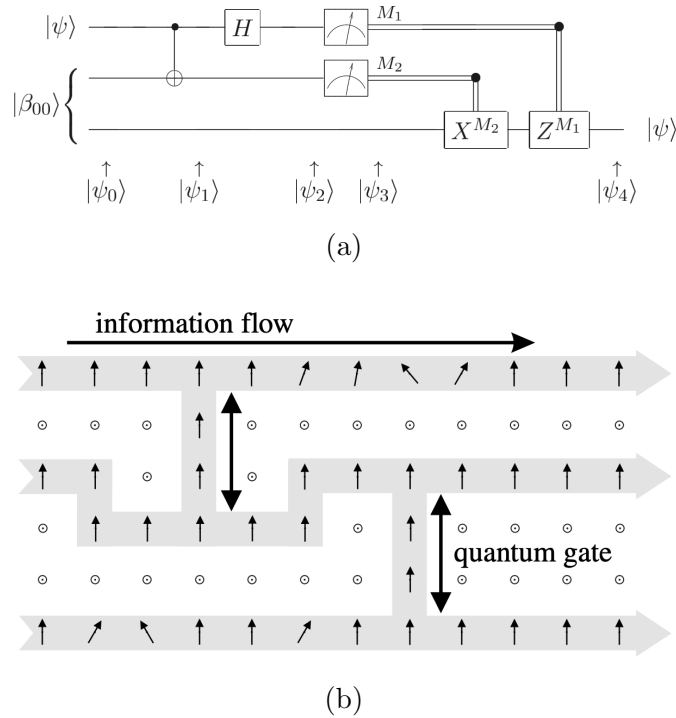


Figure 3.1: Examples of quantum computing. (a) example of circuit-based quantum computing [40]; (b) example of measurement-based quantum computing [49].

Later, the measurement-based QC was extended from qubit to qumode [37]. One significant advantage of qumodes measurement-based QC is the scalability: the capability to handle an increasing number of qumodes in an increasingly stable way [44, 45, 33, 35, 20]. To perform universal QC and to enjoy the quantum speed up by measurement-based QC, it is believed we need to prepare 2-d cluster states [49]. To allow the quantum error correction code and reduce the error, we need to prepare 3-d cluster states [50].

3.1.3 Graph States and Cluster States

A qubit cluster state can be canonically generated by initially preparing n -qubit state in the $|+\rangle$ state, and then applying C_Z gates between some pairs of qubits to build the entanglements. It is convenient to represent cluster states as graphs where vertices are qubits and edges are the entanglement between qubits. This is called graph state representation. Figure 3.2a shows a simple two qubits cluster state, and its literal expression is:

$$\begin{aligned} & C_Z |+\rangle_1 |+\rangle_2 \\ &= \frac{1}{2}(|0\rangle_1 |0\rangle_2 + |0\rangle_1 |1\rangle_2 + |1\rangle_1 |0\rangle_2 - |1\rangle_1 |1\rangle_2) \\ &= \frac{1}{\sqrt{2}}(|0\rangle_1 |+\rangle_2 + |1\rangle_1 |-\rangle_2). \end{aligned} \quad (3.2)$$

If we apply a Hadamard transformation on the qubit 2, the state becomes:

$$\frac{1}{\sqrt{2}}(|0\rangle_1 |0\rangle_2 + |1\rangle_1 |1\rangle_2), \quad (3.3)$$

which is the Bell state [40].

We can utilize the correspondence between qubits and qumodes (table 3.1) to generate CV cluster states: the CV cluster states are generated by applying C_{PHASE} gates between some pairs of qumodes in phase-quadrature eigenstates $|0\rangle_P$. Figure 3.2b shows a simple two qumodes cluster state and the literal expression is:

$$\begin{aligned} C_{\text{PHASE}} |0\rangle_{P_1} |0\rangle_{P_2} &= \frac{1}{2\pi} e^{iQ_1 Q_2} \int dq_1 |q_1\rangle_{Q_1} \int dq_2 |q_2\rangle_{Q_2} \\ &= \frac{1}{2\pi} \int \int e^{iq_1 q_2} dq_1 |q_1\rangle_{Q_1} dq_2 |q_2\rangle_{Q_2} \\ &= \frac{1}{\sqrt{2\pi}} \int dq |q\rangle_{Q_1} |q\rangle_{P_2}. \end{aligned} \quad (3.4)$$

If we apply a Fourier transform on the qumode 2, the expression becomes:

$$\int dq |q\rangle_{Q_1} |q\rangle_{Q_2} = \int dp |p\rangle_{P_1} |p\rangle_{P_2}, \quad (3.5)$$

which is the EPR state [16], and it is the qumode counterpart of the Bell state in qubits.



Figure 3.2: Graphical representation of a cluster state: (a) vertices denote qubits in the $|+\rangle$ state, edges denote the C_Z gates; (b) vertices denote qumodes in the $|0\rangle_P$ state, edges denote C_{PHASE} gates

In fact, as we discussed in section 2.6.2, the EPR state is unphysical. The two-mode squeezed state with finite squeezing is the best practical realization of the EPR state in the laboratory, and the fault-tolerant QC with continuous-variable is still feasible with finite squeezing [34].

3.1.4 Stabilizers and Nullifiers

An important feature of any graph state $|\psi\rangle$ (over qubits or qumodes) is that the cluster states $|\psi\rangle$ satisfy the following set of eigenvalue equations:

$$S|\psi\rangle = |\psi\rangle, \quad (3.6)$$

and S is defined as:

$$S = \langle X_j \bigotimes_{k \in N_j} Z_k \rangle = \langle S_j \rangle, \quad (3.7)$$

where N_j represents the neighbors of vertex j in the graph.

For example, the stabilizer for two-qubit cluster state, as per figure 3.2a, is

$$\begin{aligned} & (X_1 Z_2) C_Z |+\rangle_1 |+\rangle_2 \\ &= \frac{1}{2} \{ |1\rangle_1 |0\rangle_2 + |1\rangle_1 (-|1\rangle_2) + |0\rangle_1 |0\rangle_2 - |0\rangle_1 (-|1\rangle_2) \} \\ &= C_Z |+\rangle_1 |+\rangle_2. \end{aligned} \quad (3.8)$$

We can translate the stabilizer to the CV cluster states. From table 3.1, we have the correspondence

$$X \rightarrow X(\xi) = e^{-i\xi P}, \quad (3.9)$$

and

$$Z \rightarrow Z(\varpi) = e^{i\varpi Q}. \quad (3.10)$$

The stabilizer now becomes

$$S_j = X_j(\xi_j) \bigotimes_{k \in N_j} Z_k(\varpi_k) = \exp \left\{ -i\xi_j \left[P_j - \sum_{k \in N_j} \frac{\varpi_k}{\xi_j} Q_k \right] \right\}. \quad (3.11)$$

As an example, the stabilizer for a two-qumode cluster state with an edge weight of one, as per figure 3.2b, is

$$\begin{aligned} & [X_1(\varpi) Z_2(\xi)] C_{\text{PHASW}} |0\rangle_{P_1} |0\rangle_{P_2} \\ &= e^{-i\xi P_1} e^{i\varpi Q_2} \frac{1}{2\pi} \int \int e^{iq_1 q_2} dq_1 |q_1\rangle_{Q_1} dq_2 |q_2\rangle_{Q_2} \\ &= \frac{1}{2\pi} \int \int e^{iq_1 q_2 + i\varpi q_2} dq_1 |q_1 + \xi\rangle_{Q_1} dq_2 |q_2\rangle_{Q_2} \\ &= \frac{1}{2\pi} \int \int e^{iq_1 q_2} e^{+iq_2(\varpi - \xi)} dq_1 |q_1\rangle_{Q_1} dq_2 |q_2\rangle_{Q_2} \end{aligned} \quad (3.12)$$

which yields stabilization for $\varpi = \xi$. If $\varpi \neq \xi$, then it means we didn't find the correct stabilizer for the two-qumode cluster state with an edge weight of one.

We can define an operator, N_j , and it relates to the stabilizer, S_j , by the following

$$S_j = \exp\{-i\xi_j N_j\} \quad (3.13)$$

with

$$N_j = P_j - \sum_{k \in N_j} \frac{\varpi_k}{\xi_j} Q_k = P_j - \sum_{k \in N_j} V_{jk} Q_k, \quad (3.14)$$

where V_{jk} is the weight between qumodes j and k , and V_{jk} is nonzero if and only if there exists an edge between vertices j and k .

Considering Eq. (3.11), Eq. (3.6) holds implies N_j satisfies

$$N_j |\psi\rangle = 0 |\psi\rangle. \quad (3.15)$$

Therefore, N_j is called nullifiers or variance-based entanglement witnesses [27]. Nullifiers are Hermitian operators, thus they can be directly measured in the experiment. Define $\mathbf{Q} = (Q_1, \dots, Q_N)^T$ and $\mathbf{P} = (P_1, \dots, P_N)^T$ for N qumodes, we can write the nullifiers equation, Eq. (3.15), into the vector form

$$(\mathbf{P} - \mathbf{V}\mathbf{Q}) |\psi\rangle = 0 |\psi\rangle, \quad (3.16)$$

where \mathbf{V} is the adjacency matrix of the cluster graph, which defines the cluster state graph shapes and edge weights. Note the CV cluster states can have weighted-edge graphs, which is not the case for qubits cluster states. A qubit graph state is described by an unweighted adjacency matrix whose entries denote edge presence (value 1) or absence (value 0)

Taking the simple CV cluster state, figure 3.2b, as an example, the matrix elements $V_{12} = V_{21} = 1$, which implies its nullifiers are

$$N_1 = P_1 - Q_2 \quad (3.17)$$

and

$$N_2 = P_2 - Q_1. \quad (3.18)$$

Applying a $\frac{\pi}{2}$ local phase shift on qumode 1 provides the two-mode squeezed nullifier, Eq. (2.84) and (2.85), with zero variance.

3.1.5 H-Graph

Now let's focus on the actual CV cluster states generated in the laboratory. Eq. (2.80) is a Hamiltonian describing the two-mode entanglement. The Hamiltonian can be generalized into a matrix form to describe the multipartite entanglement

$$H = i\hbar\kappa \sum_{i < j} G_{ij} (a_i^\dagger a_j^\dagger - a_i a_j), \quad (3.19)$$

where $\kappa = \chi\alpha_p$. χ is the 2nd-order susceptibilities of the medium and α_p is the field strength of pump field. G_{ij} is the adjacency matrix element: $G_{ij} = 0$ if there is no edge (i.e. entanglement) between mode i and j ; $G_{ij} = 1$ (or $\neq 0$) if there is an edge between mode i and j . Since the Hamiltonian has quadratic fields, it is thus called Gaussian Hamiltonian, and the corresponding states are called Gaussian states.

Using the Heisenberg equation, Eq. (2.39), we can get the equation of motion.

$$\frac{d\mathbf{x}}{dt} = \kappa \mathbf{G}\mathbf{x}, \quad (3.20)$$

where $\mathbf{x} = (\mathbf{Q}, \mathbf{P})^T$, $\mathbf{Q} = (Q_1, \dots, Q_N)^T$, $\mathbf{P} = (P_1, \dots, P_N)^T$, and \mathbf{G} is the matrix of entries G_{ij} . We now introduce a new type of graph, the H-graph, which is based on the Hamiltonian and matrix \mathbf{G} . The matrix \mathbf{G} is thus the adjacency matrix of the H graph. The nonzero matrix element G_{ij} represents there is squeezing and entanglement between mode i and j . Thus, \mathbf{G} is a symmetric matrix. Moreover, diagonalizing \mathbf{G} provides the squeezing parameters (eigenvalues) and the squeezed multi-mode observables (eigenvectors). We also always assume the initial state is the vacuum state.

Figure 3.3 is a simple example for the practical two-qumode cluster state, which is also the two-mode squeezed state. The corresponding adjacency matrix is

$$\mathbf{G} = \begin{pmatrix} 0 & 1 \\ 1 & 0 \end{pmatrix}, \quad (3.21)$$

where the diagonal elements are zero due to the lack of single-mode squeezing on each mode, and off-diagonal terms are the same and nonzero due to the two-mode squeezing between two modes.

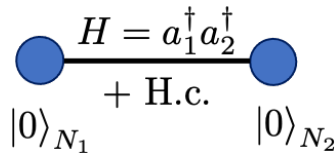


Figure 3.3: H-graph representation for two-mode cluster states. Note the starting states are vacuum states.

The relation of the H-graph, which is based on the adjacency matrix \mathbf{G} , to the canonical graph, whose graph shapes and edge weights are defined by the matrix \mathbf{V} , has been studied for infinite and finite squeezing. One of the theorem is [66], when \mathbf{G} is self-inverse:

$$\mathbf{G} = \mathbf{G}^{-1}, \quad (3.22)$$

then, under this circumstance, the adjacency matrices \mathbf{G} and \mathbf{V} are equal:

$$\mathbf{G} = \mathbf{V}. \quad (3.23)$$

3.1.6 Graphical Calculus

I will provide a short introduction of graphical calculus: a generalized CV cluster state formalism for finite squeezing [36], which is the method we used to find out the output state of the phase-modulated quantum optical frequency comb. And here, the reference I am using is in [70].

Eq. (3.20) can be solved by diagonalizing $\mathbf{G} = \mathbf{R}\mathbf{G}_{\text{diag}}\mathbf{R}^{-1}$, yielding the solution

$$\mathbf{x}(t) = \mathbf{S}(t)\mathbf{x}(0), \quad (3.24)$$

where the symplectic matrix \mathbf{S} (Note the \mathbf{S} here is not the same as the stabilizer) is given by

$$\mathbf{S}(t) = \mathbf{R}e^{t\mathbf{G}_{\text{diag}}}\mathbf{R}^{-1}, \quad (3.25)$$

and \mathbf{R} is the unitary transformation matrix obtained from eigenvectors of \mathbf{G} . Note that, in a sequence of unitary operations ($t_n > t_{n-1} > \dots > t_1$), the symplectic matrix ordering is the Schrödinger picture one

$$\mathbf{x}(t_n) = \mathbf{S}_n(t_n)\mathbf{S}_{n-1}(t_{n-1}) \cdots \mathbf{S}_1(t_1)\mathbf{x}(0) = \mathbf{S}\mathbf{x}(0). \quad (3.26)$$

Once \mathbf{S} is known, we obtain the covariance matrix $\mathbf{\Sigma}$, which contains all the information about the Gaussian state,

$$\mathbf{\Sigma} = \frac{1}{2} \mathbf{S}\mathbf{S}^T. \quad (3.27)$$

An important property of $\mathbf{\Sigma}$ is that it is related to the complex graph of the Gaussian state [36], which we now briefly introduce.

Gaussian states are described by a complex-weighted adjacency matrix $\mathbf{Z} = \mathbf{V} + i\mathbf{U}$, where \mathbf{V} is the exact analog to the adjacency matrix of a qubit graph state [44] and \mathbf{U} is called the error matrix, and $\mathbf{U} \rightarrow 0$ in the limit of infinite squeezing. See subsection 3.2.3 for a discussion about the importance of error matrix \mathbf{U} .

Any Gaussian state $|\psi\rangle$ can be defined by its nullifiers

$$(\mathbf{P} - \mathbf{Z}\mathbf{Q})|\psi\rangle = \mathbf{0}|\psi\rangle. \quad (3.28)$$

Because \mathbf{Z} is complex in general, these nullifiers are non-Hermitian and cannot be measured, which makes measurement-based quantum computing problematic since it must proceed by measuring, among other things, graph nullifiers [26]. Thus, only Gaussian states with \mathbf{Z} real, i.e., with $\mathbf{Z}=\mathbf{V}$ and $\mathbf{U}=\mathbf{0}$, can be proper cluster states.

However, measurement-based quantum computing is still possible with $\mathbf{U} \neq \mathbf{0}$. In that case, we use the (arbitrarily good) approximate nullifiers given by Hermitian operators $\mathbf{P} - \mathbf{V}\mathbf{Q}$, which verify [36]

$$\text{cov}[\mathbf{P} - \mathbf{V}\mathbf{Q}] = \frac{1}{2} \mathbf{U}, \quad (3.29)$$

where we defined the covariance matrix in the standard way for vector operator \mathbf{A} with zero expectation values in state $|\psi\rangle$,

$$(\text{cov}[\mathbf{A}])_{jk} = \frac{1}{2} \langle \psi | \{A_j^\dagger, A_k\} | \psi \rangle. \quad (3.30)$$

We can deduce from Eq. (3.29) that an arbitrary Gaussian state of the matrix \mathbf{Z} can be accurately considered as a cluster state of the matrix \mathbf{V} iff

- (i), the error matrix \mathbf{U} is diagonal [23, 24] and,
- (ii), it verifies $\text{tr}[\mathbf{U}] \rightarrow 0$ in the limit of infinite squeezing [36].

In that case, $\mathbf{P} - \mathbf{V}\mathbf{Q}$ are squeezed, uncorrelated Hermitian operators.

We are now ready to determine the Gaussian graph matrix \mathbf{Z} from the covariance matrix. The relation between the two is [36]

$$\mathbf{\Sigma}_x = \text{cov}[\mathbf{x}] = \frac{1}{2} \begin{pmatrix} \mathbf{U}^{-1} & \mathbf{U}^{-1}\mathbf{V} \\ \mathbf{V}\mathbf{U}^{-1} & \mathbf{U} + \mathbf{V}\mathbf{U}^{-1}\mathbf{V} \end{pmatrix}, \quad (3.31)$$

where the block structure coincides with the definition of \mathbf{x} . Note in the case of infinite squeezing, $\mathbf{U} \rightarrow 0$ and $\mathbf{U}^{-1} \rightarrow \infty$, the covariance matrix Σ_x becomes ill-defined. This result is corresponding to the quadrature eigenstates at infinite squeezing have $\Delta P \rightarrow 0$ and $\Delta Q \rightarrow \infty$, and the quadrature eigenstates are non-normalizable. For a free field, the Hamiltonian is proportional to $P^2 + Q^2$, and the energy becomes infinite when squeezing is infinite. Therefore, the infinitely squeezed CV cluster states are not achievable. The covariance matrix can also be represented by quadratures as the following

$$\Sigma_x = \begin{pmatrix} \text{cov}[\mathbf{Q}] & \text{cov}[\mathbf{Q}, \mathbf{P}] \\ \text{cov}[\mathbf{P}, \mathbf{Q}] & \text{cov}[\mathbf{P}] \end{pmatrix}. \quad (3.32)$$

As an example, for the case of two modes, $\mathbf{x} = (\mathbf{Q}, \mathbf{P})^T$, $\mathbf{Q} = (Q_1, Q_2)^T$, $\mathbf{P} = (P_1, P_2)^T$, and the covariance matrix in terms of quadratures is

$$\Sigma_x = \left\langle \begin{pmatrix} Q_1^2 & Q_1 Q_2 & \frac{1}{2}(Q_1 P_1 + P_1 Q_1) & Q_1 P_2 \\ Q_2 Q_1 & Q_2^2 & Q_2 P_1 & \frac{1}{2}(Q_2 P_2 + P_2 Q_2) \\ \frac{1}{2}(P_1 Q_1 + Q_1 P_1) & P_1 Q_2 & P_1^2 & P_1 P_2 \\ P_2 Q_1 & \frac{1}{2}(P_2 Q_2 + Q_2 P_2) & P_2 P_1 & P_2^2 \end{pmatrix} \right\rangle. \quad (3.33)$$

One final remark highlights the importance of \mathbf{U} . The covariance matrix can be rewritten, using the rewritten symplectic vector $\mathbf{y} = (\mathbf{Q}, \mathbf{P} - \mathbf{V}\mathbf{Q})^T$, as

$$\Sigma_y = \text{cov}[\mathbf{y}] = \frac{1}{2} \begin{pmatrix} \mathbf{U}^{-1} & \mathbf{0} \\ \mathbf{0} & \mathbf{U} \end{pmatrix}. \quad (3.34)$$

An allowable strategy for diagonalizing \mathbf{U} so that it verifies (i,ii) above is to apply local symplectic operations, which are equivalent to local unitaries (LU), to qumodes [36, 23] since these cannot change the state's entanglement. We will be making abundant use of this property.

Remark: When dealing with a sequence of unitary operations, one can apply Eq. (3.26) directly, or another, equivalent way to treat the cascading case is the Möbius transformation [36]

$$\mathbf{Z}' = (\mathbf{C} + \mathbf{DZ})(\mathbf{A} + \mathbf{BZ})^{-1}. \quad (3.35)$$

where \mathbf{Z}' is the resulting adjacency matrix by the action of second symplectic matrix, which is in the form $\mathbf{S} = \begin{pmatrix} \mathbf{A} & \mathbf{B} \\ \mathbf{C} & \mathbf{D} \end{pmatrix}$.

3.2 Cluster State Generation in the Phase-Modulated QOFC

In this section, I will first introduce the phase modulation achieved by an electro-optical modulator (EOM). And then, I will present the output state in the phase-modulated QOFC.

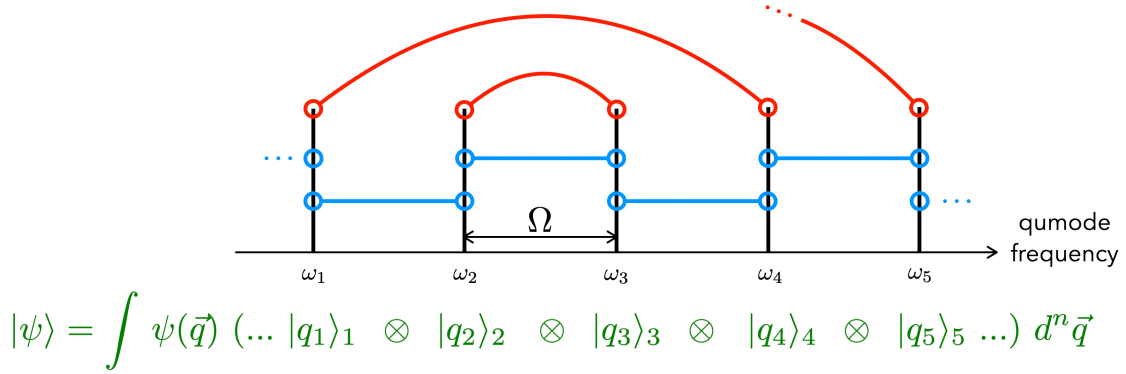


Figure 3.4: Quantum description of PM at frequency Ω (blue lines) of the two-mode-squeezed (red lines, pump frequency $\omega_2 + \omega_3$) QOFC: because the modulation frequency equals the qumode spacing, there is no vacuum input and a unitary operation can be realized solely on the initial comb state $|\psi\rangle$.

3.2.1 Phase Modulation

When a monochromatic light field of frequency ω_0 has been phase modulated, say by an electro-optical modulator, the sidebands at frequencies $\omega_n = \omega_0 + n\Omega$ ($n \in \mathbb{Z}$) having amplitudes given by the Bessel functions of the first kind can be generated

$$e^{i[\omega_0 t + m \sin(\Omega t + \phi)]} = e^{i\omega_0 t} \sum_{n=-\infty}^{\infty} J_n(m) e^{in(\Omega t + \phi)}, \quad (3.36)$$

where m is the modulation index and ϕ the PM phase. An effective quantum model of PM [11] is the multiport frequency-domain beamsplitter Hamiltonian

$$H_{PM} = \hbar \frac{\alpha}{\tau} e^{-i\phi} \sum_{j=-\infty}^{\infty} a_j a_{j+\Omega}^\dagger + \text{H.c.}, \quad (3.37)$$

where $\alpha = m/2$, τ is the interaction time in the phase modulator, and a_j is the annihilation operator of the qumode of frequency j in units of the qumode spacing, i.e., of the free spectral range (FSR) of the OPO. We take Ω in units of the FSR from Eq. (3.37) on. The use of a QOFC input to PM replaces vacuum inputs with QOFC qumodes when Ω is an integer, figure 3.4.

By solving the Heisenberg equation and following the procedure in subsection 3.1.6, we can obtain, for $\phi = \pi/2$ in Eq. (3.37), the analytic expression of the PM symplectic matrix

$$\mathbf{S}^{(PM)} = \begin{pmatrix} \mathbf{M} & \mathbf{0} \\ \mathbf{0} & \mathbf{M} \end{pmatrix}, \quad (3.38)$$

where we have, for $\Omega = 1$,

$$\mathbf{M}_{jk} = J_{k-j}(m) - (-1)^j J_{k+j}(m). \quad (3.39)$$

This gives the well-known phase modulation spectrum, as was first obtained by Capmany and Fernández-Pousa [11]. Note that $\mathbf{S}^{(PM)}$ may not be block-diagonal for other values of ϕ , which will lead to couplings between amplitude and phase quadratures. These are therefore totally controllable by setting ϕ experimentally.

3.2.2 Cluster State Generation in the Phase-Modulated EPR QOFC

We now demonstrate cluster state generation by external phase modulation of the EPR QOFC emitted by a monochromatically pumped OPO below the threshold. Figure 3.5 depicts the experimental configuration.

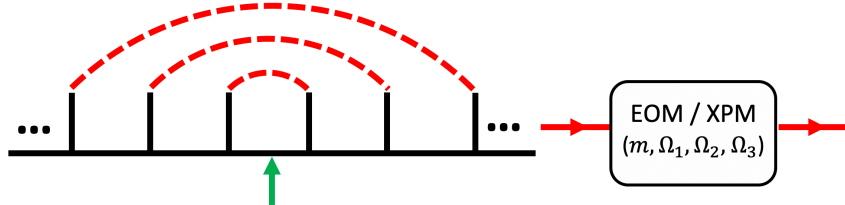


Figure 3.5: Phase modulation of a single QOFC. An OPO with a single pump frequency, whose half is denoted by the green arrow, creates TMS qumode pairs as indicated by the red dashed lines. Electro-optic phase modulation, or Kerr-medium cross phase modulation, is then done at index m and frequencies $\Omega_{1,2,3}$.

A doubly resonant OPO is pumped at a single frequency ω_p such that frequency $\omega_p/2$ is set exactly halfway between 2 OPO mode frequencies (usually by a phase lock loop [48, 13]), as per the green arrow in figure 3.5. This generates independent EPR qumode pairs in two-mode-squeezed (TMS) states [41, 52], a.k.a. the EPR QOFC. While entanglement scalability is already present in this case, it manifests itself only as of the scaling of the number of copies of a bipartite EPR state, rather than as the scaling of the size of a multipartite state. Phase modulation by the EOM of the OPO QOFC will change that: by modulating at one, two, or three frequencies, we can knit up 1-d, 2-d (square-grid), 3-d (cubic) cluster states. We postulate that this extends to n -hypercubic cluster states, using n modulation frequencies.

Note that, for every graph presented in this paper, we conducted a thorough analysis of the errors due to finite squeezing and imperfections due to nonlocal modulation couplings. This analysis is detailed in [70].

3.2.2.a Generation of 1-d cluster states:

Following the steps in subsection 3.1.5 and 3.1.6, we derive the complex adjacency matrix \mathbf{Z} of the created Gaussian state for $\Omega_1=1$, $r=2,3$, and for $m=0, 0.1, 0.2, 0.5$, and 1 rad. Figure 3.6 displays the real and imaginary parts of \mathbf{Z} (\mathbf{V} and \mathbf{U} , respectively) after the appropriate LUs were applied; these LUs are Fourier transforms, i.e., rotations by $\pi/2$ in quadrature phase space (Q, P) , exerted on the lower-frequency-half qumodes, i.e., on all qumodes left of the green arrow in figure 3.5.

We can immediately see that phase modulation yields multipartite entanglement. We now examine the particular graphs that can be generated by this method, turning first to the effect of the modulation index parameter m . The initial case $m = 0$ corresponds to EPR pairs from the OPO with no phase modulation. When the latter is turned on, additional edges are created, whose weights increase with m , as the EPR weights decrease. The classical FM spectra in the left column of figure 3.6 give a good illustration of the effect on the quantum graph of the oscillations with

3.2. CLUSTER STATE GENERATION IN THE PHASE-MODULATED QOFC

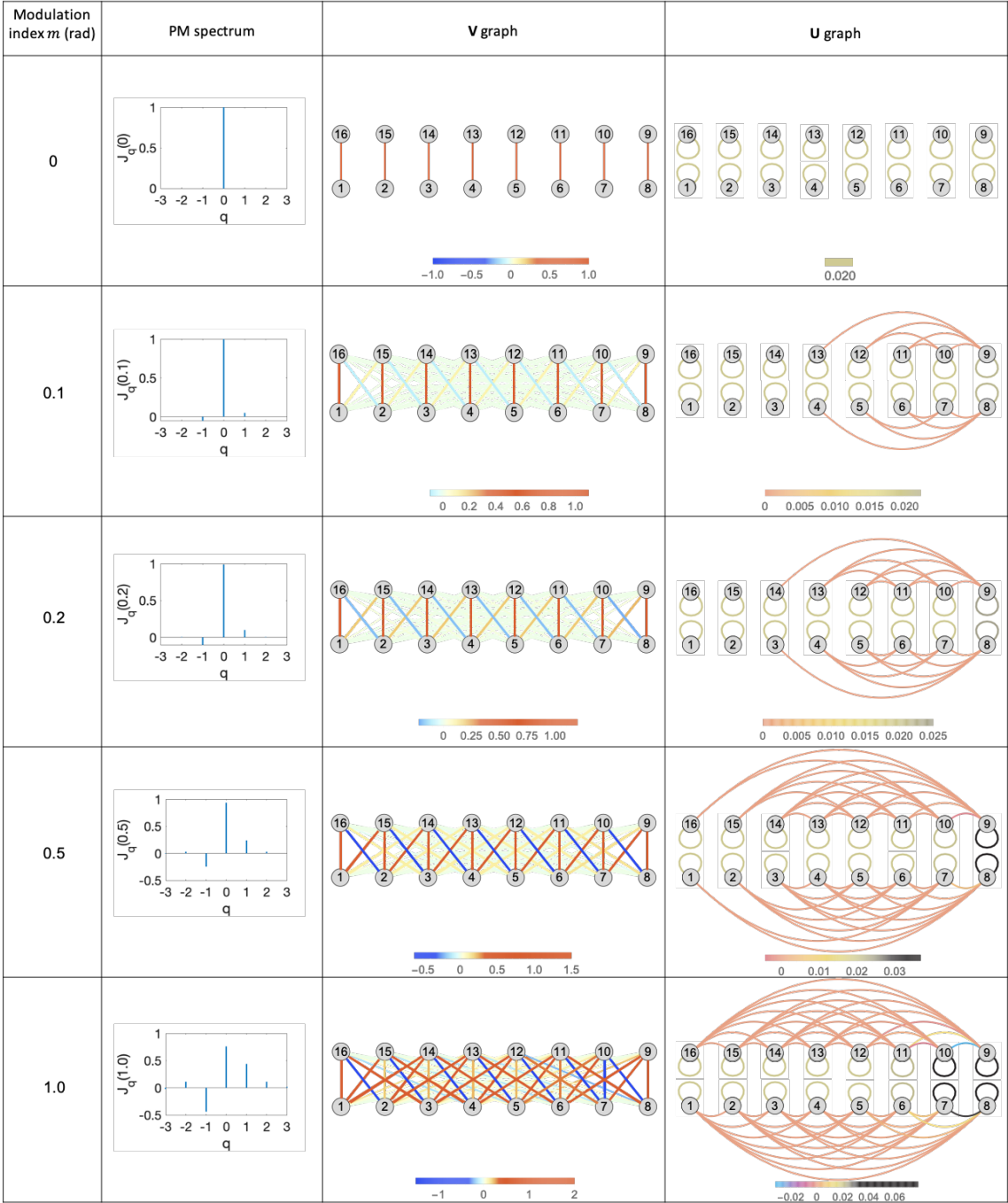


Figure 3.6: \mathbf{V} and \mathbf{U} graphs for the state generated by OPO-extrinsic PM at $\Omega_1=1$ and $r=2,3$, for different values of m . The pump frequency is equal to the sum of the frequencies of all vertical qumode pairs in the \mathbf{V} and \mathbf{U} graph columns. Note that the qumode labeled “0” in the PM spectrum column is any of the QOFC qumodes in the \mathbf{V} and \mathbf{U} graph columns.

m of the Bessel-function amplitudes. The onset of next-nearest neighbor couplings in the quantum graph coincides, unsurprisingly, with the growth of the first-order modulation sidebands, decrease of the carrier, and rise of the second harmonic sidebands. Such non-local graph edges are a known hindrance to one-way quantum computing [3, 25, 7]. However, this problem can be circumvented upon closer, rigorous inspection of the edges’ weights, which can always be found to be too small

to be observable when m isn't too large [70]. Note that this optimal m will decrease as the squeezing parameter r increases.

Remarkably, the imaginary part of the graph (rightmost column of figure 3.6), given by the error matrix \mathbf{U} , complements the \mathbf{V} graph, which tends toward a complete bipartite graph with increasing m . In a sense, \mathbf{U} leaves \mathbf{V} globally invariant in terms of its bipartite structure, i.e., while \mathbf{V} only connects qumode set $\{1, \dots, 8\}$ to qumode set $\{9, \dots, 16\}$ in figure 3.6, \mathbf{U} only connects qumodes within each of these two sets.

Note the self-loops in the \mathbf{U} denote the main diagonal matrix elements of \mathbf{U} matrix.

The same property that spurious edges can always be made small enough will appear in the \mathbf{U} graph. In [70], we will show that \mathbf{U} is weak enough to validate this experimental technique.

Another crucial point that can be made immediately is that $\text{tr}\{\mathbf{U}\} \rightarrow 0$ when $r \gg 1$, as required and illustrated in figure 3.7, where $\text{tr}\{\mathbf{U}\}$ is plotted and shown to adhere to the theoretical value obtained analytically for two-mode squeezed states [36]. This point is important: it means that PM of two-mode-squeezed pairs

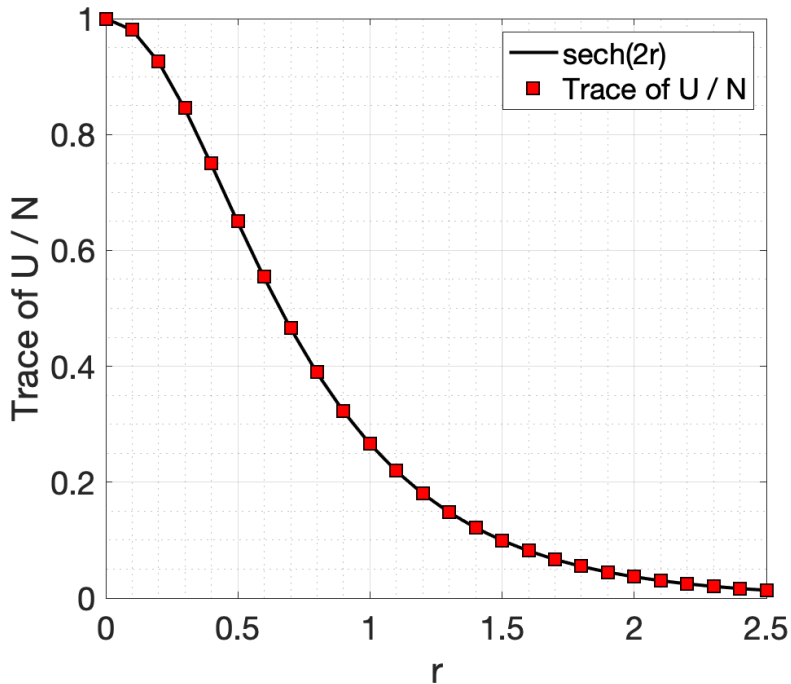


Figure 3.7: Plot of the average trace of \mathbf{U} versus the squeezing parameter r , compared to the function $\text{sech}(2r)$. This \mathbf{U} matrix is for the externally modulated QOFC at $\Omega_1=1$.

doesn't detract from the fact that the overall cluster state error is solely determined by the amount of initial squeezing. One should indeed remember that \mathbf{U} , being symmetric positive semidefinite, must tend to zero as a whole when its trace tends to zero as per requirement (ii). (Note that requirement (i) remains crucial as we cannot reach this infinite squeezing limit experimentally and, again, a fault-tolerance threshold has been proven to exist in this case of finite squeezing [34].)

At this point, we anticipate the conclusions of the rigorous error analysis [70]

and ignore the weak edges in the whole complex graph to focus on the cluster states constructed by the dominant edges. We only have to limit the modulation index m to low enough a value, keeping the PM couplings nearest-neighbor so as not to get nonlocal edges. The resulting graph is given by figure 3.8(a). Swapping every

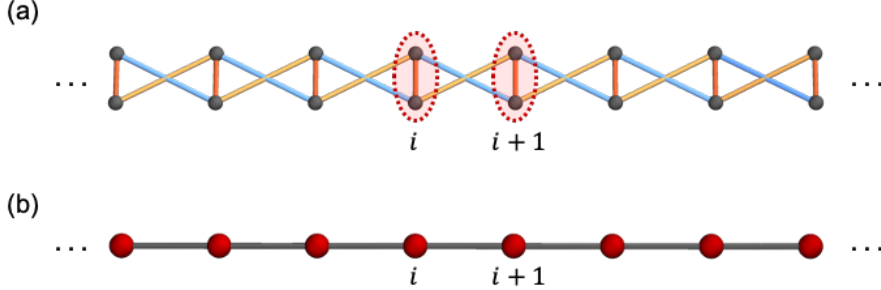


Figure 3.8: (a) \mathbf{V} graph of figure 3.6, revealing its typical structure for 1D cluster state. Two modes that are in the red dashed circle are the EPR-qumodes. (b) compact representation of the graph using EPR macronodes.

other vertical pair of qumodes shows the graph to be a 1-d “ladder” whose rungs are the initial EPR-pair qumodes. This dual graph structure connected by the initial EPR pairs will actually be a feature of the 2-d and 3-d graphs as well. In order to simplify the graph rendering, in this case, we will bunch these EPR pairs into “EPR macronodes,” as in figure 3.8(b). This ladder state spans the whole phasematching bandwidth of the OPO, which can reach 10 THz in our previous work [61]. With a typical mode spacing of 1GHz [48, 13], this yields on the order of 10^4 entangled qumodes in this linear cluster state.

As is well known, the 1-d graph isn’t enough to generate the universal gate set in one-way quantum computing, for which a 2-d graph is required.

3.2.2.b Generation of 2-d ClusterStates:

The experimental configuration of figure 3.5 is surprisingly versatile: just adding modulation frequencies allows to increase the dimension of the graph lattice. Again, see [70] for a detailed analysis of all graph imperfections and why they are negligible.

Driving the EOM with two modulation signals at frequencies $\Omega_{1,2}$ transforms Eq. 3.37 into

$$H_{PM2} = \hbar \left[\frac{\alpha_1}{\tau} e^{-i\phi_1} \sum_{j=-\infty}^{\infty} a_j a_{j+\Omega_1}^\dagger + \frac{\alpha_2}{\tau} e^{-i\phi_2} \sum_{j=-\infty}^{\infty} a_j a_{j+\Omega_2}^\dagger \right] + \text{H.c.} \quad (3.40)$$

Here we set $\phi_1 = \phi_2 = \pi/2$, $\alpha_1 = \alpha_2$, and follow the same procedure as in the 1-d case, which yields the square-grid cluster state of figure 3.9. One can interpret this case in the following way: PM at frequency $\Omega_1=1$ creates next-neighbor coupling in the QOFC which forms a ladder graph; PM at frequency $\Omega_2=10$ then introduces additional coupling every 10 modes which is tantamount to spiraling the ladder into the two-layer square-grid cluster state of figure 3.9(a). As in figure 3.8(b), a more streamlined version of the graph can be obtained by considering EPR macronodes; see figure 3.9(b).

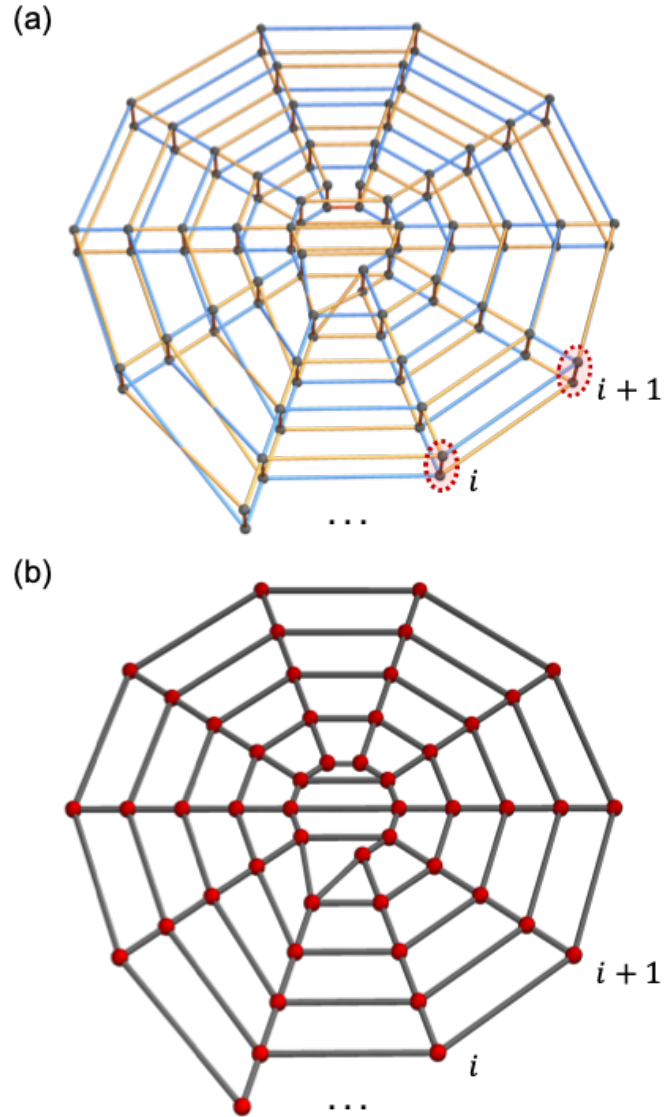


Figure 3.9: (a), square-grid cluster state created with $\Omega_1=1$, $\Omega_2=10$. Two modes circled by red dashed lines are EPR-qumodes, one of which is on the upper layer and the other one is on the bottom layer. (b), same graph, over EPR macronodes. The width of this square lattice is the number of “spokes” in the graph: $\Omega_2/\Omega_1 = 10$.

As was mentioned earlier, the width of the square lattice, which is the number of “spokes”, is simply the ratio Ω_2/Ω_1 , the total number N of qumodes being determined by the phasematching bandwidth of the OPO’s nonlinear medium. In the case of our previous experiments [48, 13], for which we estimated $N \sim 10^4$ [61], a 100×100 square cluster grid could therefore be created with PM at 1 and 100 GHz for a 1 GHz mode spacing. Note also that, in this case, the quasi-phasematching bandwidth can be further engineered to be larger.

This is an important result because the square-grid cluster state is a resource for universal quantum computing. Note that this is true even though the cluster state is a Gaussian state and that universal quantum computing requires non-Gaussian resources for exponential speedup and quantum error correction. This is strictly equivalent to the qubit case where cluster states stabilized by Pauli operators, globally invariant under Clifford operations (just like CV clusters are stabilized by Weyl-Heisenberg displacements, globally invariant under Gaussian operations), even though non-Clifford resources are required to achieve exponential speedup. In both cases, the necessary respective non-Gaussian and non-Clifford gates are realized by like measurements on the cluster state.

3.2.2.c Generation of 3-d Cluster States:

At this point, we make the general claim that simply adding another modulation frequency adds another dimension to the EPR-macronode graph, extending this procedure to yield hypercubic cluster graphs. We illustrate this in the 3-d case, which is relevant to quantum computing because the 3-d architecture is a known base for implementing topological error encoding over cluster states [50].

With modulation frequencies, $\{\Omega_1, \Omega_2, \Omega_3\} = \{1, 8, 80\}$, the quantum derivation yields the graph state pictured over EPR macronodes in figure 3.10. The six-edge valence of each graph vertex is clear in their vast majority. Note that, as always for cluster states, any local imperfections (graph center) in the graph can be removed by single-qumode measurements [8, 68, 26].

Finally, the ratio of PM frequencies determines the graph's structure, which here is cylindrical: the number of "spokes" is set by Ω_3/Ω_2 and the length of the cylinder is set by Ω_2/Ω_1 . The radius of the spokes increases with the mode number N as N/Ω_3 . In the example of figure 3.10, a cubic cluster state is created over 400 macronodes in a cylindrical shape with 10 "spokes", five set of macronodes in the radial direction, and a cylinder 8 macronodes long.

3.2.3 Graph Error Analysis:

As we mentioned earlier, an arbitrary Gaussian state is a valid cluster state iff

- (i), the error matrix \mathbf{U} is diagonal [23] and,
- (ii), it verifies $\text{tr}\{[\mathbf{U}]\} \rightarrow 0$ in the limit of infinite squeezing [36].

While requirement (ii) has been systematically fulfilled in all previous realizations of CV cluster states [65, 48, 13, 64, 2, 30], requirement (i) had not been considered until very recently [23], largely because all previous experimental realizations of cluster states had, in theory, a diagonal \mathbf{U} (in practice, they might not have). In this thesis, \mathbf{U} is not always diagonal, which can be seen as the price to pay for the considerable simplification of the experimental setup. As Eq. 3.34 makes clear, an off-diagonal element of \mathbf{U} has the general physical meaning of a correlation between two cluster-state nullifiers. Such covariances must be zero in order for the cluster state to be adequate for one-way quantum computing. We evaluate the contribution of off-diagonal elements of \mathbf{U} and determine the precise conditions under which they can be neglected, which amounts to relaxing requirement (i) to

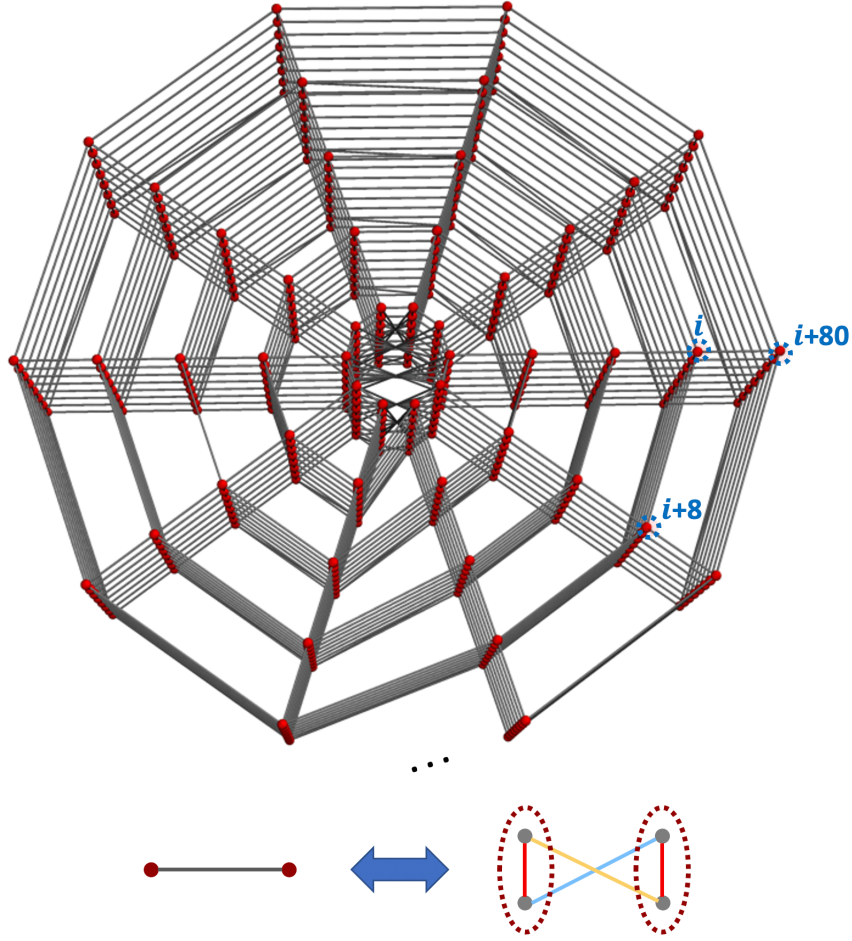


Figure 3.10: Cubic cluster state, over $N=400$ EPR macronodes, obtained from $\{\Omega_1, \Omega_2, \Omega_3\} = \{1, 8, 80\}$. Number of "spokes"=10. Length= 8 macronodes. Spoke length= 5 macronodes.

(i'), the error matrix \mathbf{U} is diagonally dominant.

Before we deal with error matrix \mathbf{U} , we first assume it fulfills both (i) and (ii) and focus on the effect of the weak, undesirable edges in \mathbf{V} that can be seen in figure 3.6 but not in figure 3.8.

Effect of a spurious graph edge – bipartite case:

We first take the simplest example of a canonical cluster state: in the unphysical limit of infinite squeezing, a single qumode 1 has, by definition, nullifier P_1 . In the realistic case of finite squeezing, the exact nullifier of qumode 1 in a single-mode squeezed (SMS) state of squeezing parameter r_1 is

$$\mathcal{N}_{s1} = S_1(r_1) a_1 S_1^\dagger(r_1) = P_1 - ie^{-2r_1} Q_1. \quad (3.41)$$

These nullifiers are given by the complex \mathbf{Z} graph, which always exists, but they are non-Hermitian, which makes the graph unsuited for quantum computing. A cluster state can be well defined as long as the imaginary part of \mathbf{Z} , \mathbf{U} , fulfills requirements (i,ii). Finite squeezing is not a problem so long as it reaches a fault tolerant value, which has been theoretically proven to be within experimental reach [34].

Two phase-squeezed qumodes coupled by gate $C_Z = \exp(i\varepsilon Q_1 Q_2)$ form a Gaussian cluster state of nullifiers

$$\mathcal{N}_1 = C_Z \mathcal{N}_{s1} C_Z^\dagger = P_1 - i e^{-2r_1} Q_1 - \varepsilon Q_2 \quad (3.42)$$

$$\mathcal{N}_2 = C_Z \mathcal{N}_{s2} C_Z^\dagger = P_2 - i e^{-2r_2} Q_2 - \varepsilon Q_1, \quad (3.43)$$

where \mathbf{U} is diagonal and vanishes with increasing squeezing. We now ask the following question: if we wrongly assumed qumode 1 to be isolated when it is, in fact, linked to qumode 2 by a graph edge of small weight ε , how large could ε be before its effects are detectable?

To answer this question, we must first relate it to the actual physical measurements we can make on qumode 1.

Under the assumption that we have two single-mode phase-squeezed states, the lowest measurement noise should be obtained by measuring the phase quadrature operator P_1 , typically by homodyne detection. In the case of a phase-squeezed qumode 1, observable P_1 has squeezed noise given by

$$(\Delta P_1)^2 = {}_1\langle 0 | S_1(r_1)^\dagger P_1^2 S_1(r_1) | 0 \rangle_1 = \frac{1}{2} e^{-2r_1}. \quad (3.44)$$

We now assume P_1 when qumode 1 also has a C_Z graph edge of weight ε with qumode 2 (squeezed by r_2), then we have

$$\begin{aligned} (\Delta P_1)^2 &= {}_{12}\langle 00 | S_2^\dagger S_1^\dagger C_Z^\dagger P_1^2 C_Z S_1 S_2 | 00 \rangle_{12} \\ &= {}_{12}\langle 00 | (P_1 e^{-r_1} - \varepsilon Q_2 e^{r_2})^2 | 00 \rangle_{12} \\ &= \frac{1}{2} e^{-2r_1} [1 + \varepsilon^2 e^{2(r_1+r_2)}]. \end{aligned} \quad (3.45)$$

Comparing Eq. 3.44 and 3.45, we deduce the condition for neglecting a graph edge of weight ε :

$$\varepsilon \ll \varepsilon_{\min} = e^{-(r_1+r_2)} \quad (3.46)$$

where ε_{\min} is the edge weight at which the quantum noise is raised by 3 dB on a single qumode quadrature measurement. Short conclusions from the bipartite case are: (1) Eq. 3.44 implies the effect of omitting the spurious graph edge is a decrease in the squeezing of qumode 1. And (2) Eq. 3.45 indicates the amount of squeezing determines how weak the spurious graph edge weight can be measured: the higher the squeezing, the smaller the graph edge weight can be detected.

The above analysis can be generalized to find out the effect of spurious graph edges on the multipartite case, but the short conclusions from the bipartite case still hold. Readers who are interested in learning about the full graph error analysis can check Xuan Zhu's Ph.D. thesis or reference [70]. We now turn to the details of how to generate EPR QOFC in the laboratory.

Chapter 4

The Optical Parametric Oscillator

This chapter will introduce the optical parametric oscillator (OPO), an optical cavity with at least one nonlinear medium inside. OPO is a crucial element in this experiment because it generates the two-mode squeezed state, used as the building block for generating larger cluster states. I will also talk about how we lock the OPO and make the cavity resonance follow the locking laser. Lastly, I will discuss how to measure the parametric gain to estimate the maximal of squeezing. An excellent reference I use here is Moran Chen's thesis [12].

4.1 Optical Cavity

An optical cavity is an arrangement of at least two mirrors, and light waves bounce back and forth between those mirrors to do the interference. Hence, only some light that matches the cavity eigenmodes (transverse modes) can be confined inside the cavity. The cavity also imposed another condition on the frequency of light: only light satisfies the resonance condition (longitudinal modes) of the cavity can pass through the cavity.

In the experiment, we use a four-mirror one-sided cavity, which implies one mirror, output coupler (OC), has intensity reflection ($r_1'^2 = 5\%$) and the rest have near unity reflection ($r_2'^2 = r_3'^2 = r_4'^2 = 99.995\%$). For the simplicity of theory, we can use a two-mirror cavity to model it without loss of generality. Assuming the cavity is lossless, some of the important features and definitions are listed in the following:

- **Reflected field, field inside the cavity, and transmitted field:**

for a field $E_i = E_0 e^{i\omega t}$ incident to a two-mirror cavity with field reflection coefficient r_1 (incident mirror) and r_2 , the total reflected field is

$$E_r = \frac{r_2 e^{i\delta} - r_1}{1 - r_1 r_2 e^{i\delta}} E_i, \quad (4.1)$$

the total field inside the cavity is

$$E_c = \frac{t_1}{1 - r_1 r_2 e^{i\delta}} E_i, \quad (4.2)$$

and the total transmitted field is

$$E_t = \frac{t_1 t_2 e^{i\delta/2}}{1 - r_1 r_2 e^{i\delta}} E_i, \quad (4.3)$$

where $\delta = \frac{\omega L}{c}$ is the round trip phase shift, L is the round trip cavity length, $t_1 = \sqrt{1 - r_1^2}$ and $t_2 = \sqrt{1 - r_2^2}$ are the field transmission coefficient, and c is the speed of light in vacuum. Figure 4.1 illustrates the incident, total reflected, total internal, and total transmitted field for a two-mirror cavity.

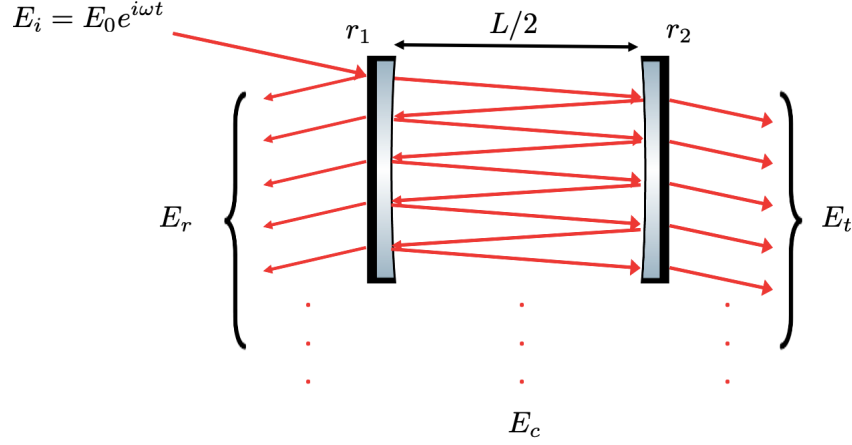


Figure 4.1: The total reflected, total internal, and total transmitted field of a two-mirror cavity when the incident beam is injected from r_1 mirror side. L is the round trip length of the cavity

Therefore, we can find the reflection

$$R = \left(\frac{E_r}{E_i} \right)^2, \quad (4.4)$$

and the phase response

$$\theta_R = \arctan \left(\frac{E_r}{E_i} \right). \quad (4.5)$$

Similarly, for the total internal field and total transmitted field, we have

$$C = \left(\frac{E_c}{E_i} \right)^2, \quad (4.6)$$

$$\theta_C = \arctan \left(\frac{E_c}{E_i} \right), \quad (4.7)$$

$$T = \left(\frac{E_t}{E_i} \right)^2, \quad (4.8)$$

$$\theta_T = \arctan \left(\frac{E_t}{E_i} \right). \quad (4.9)$$

Figure 4.3 illustrates the lossless cavity response for case of cavity with $r_1^2 = 0.95$ and $r_2^2 = 0.99995$. Due to the fact of the lossless cavity, one can see $T + R = 1$ holds. One can also notice the internal intensity can be built up to a very large amount. Lastly, when the frequency of the incident field differs from the resonance frequency of the cavity (frequency detuning), the reflected and transmitted fields always have phase shifts. The phase response is the key to the Pound-Drever-Hall (PDH) cavity locking, which will be discussed later.

Remark The four-mirror cavity is slightly more complicated than the two-mirror cavity due to (1) the light is bouncing back and forth between four mirrors instead of two mirrors; (2) the four-mirror cavity has three transmitted fields rather than one. For the above two reasons, the total reflected fields, total fields inside the cavity, and the total transmitted fields are changed accordingly. Figure 4.2 shows a four-mirror cavity with an incident field E_i to the OC. $r'_1, r'_2, r'_3,$ and r'_4 are the field reflection coefficients. $l'_1, l'_2, l'_3,$ and l'_4 are the distances between mirrors. The total cavity length is L' and $L' = l'_1 + l'_2 + l'_3 + l'_4$.

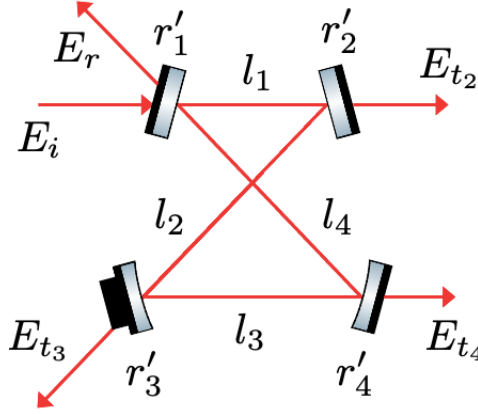


Figure 4.2: Four-mirror cavity. $r'_1, r'_2, r'_3,$ and r'_4 are the field reflection coefficients. $l'_1, l'_2, l'_3,$ and l'_4 are the distances between mirrors.

The total reflected field is

$$E_r = \frac{r'_2 r'_3 r'_4 e^{i\delta'} - r'_1}{1 - r'_1 r'_2 r'_3 r'_4 e^{i\delta'}}, \quad (4.10)$$

the total field inside the cavity is

$$E_c = \frac{t'_1}{1 - r'_1 r'_2 r'_3 r'_4 e^{i\delta'}} E_i, \quad (4.11)$$

and the total transmitted fields are

$$E_{t_2} = \frac{t'_1 t'_2 e^{i\delta'_1}}{1 - r'_1 r'_2 r'_3 r'_4 e^{i\delta'}} E_i, \quad (4.12)$$

$$E_{t_3} = \frac{t'_1 r'_2 t'_3 e^{i(\delta'_1 + \delta'_2)}}{1 - r'_1 r'_2 r'_3 r'_4 e^{i\delta'}} E_i, \quad (4.13)$$

$$E_{t_4} = \frac{t'_1 r'_2 r'_3 t'_4 e^{i(\delta'_1 + \delta'_2 + \delta'_3)}}{1 - r'_1 r'_2 r'_3 r'_4 e^{i\delta'}} E_i, \quad (4.14)$$

where $\delta' = \frac{\omega L'}{c}$ is the total trip phase shift, $\delta'_i = \frac{\omega l'_i}{c}$ is the phase shift due to l'_i , $t'_i = \sqrt{1 - r'^2_i}$ is the field transmission coefficient, and $i \in \{1, 2, 3\}$. One can use the above five field equations to find the cavity responses, similar to what I did for the figure 4.3. Note by setting $r_1 = r'_1$ and $r_2 = r'_2 r'_3 r'_4$, Eqs. (4.10) and (4.11) become Eqs (4.1) and (4.2) for the two-mirror cavity case.

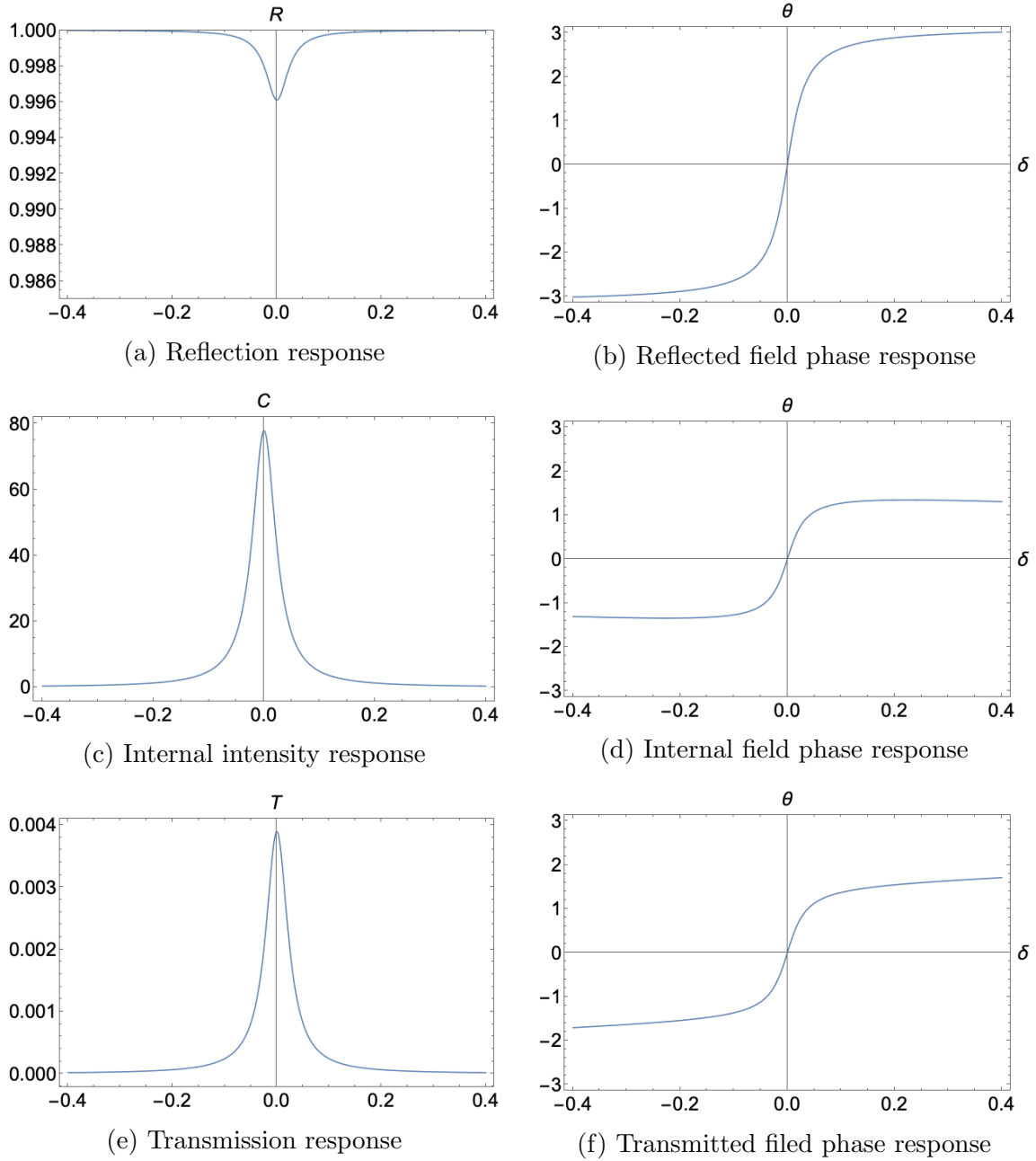


Figure 4.3: Illustration of the cavity response for a lossless cavity with $r_1^2 = 0.95$ and $r_2^2 = 0.99995$. On the left side is the intensity response and on the right side is the phase response. The x-axis in all the subfigures is the round trip phase shift, which is proportional to the frequency detuning.

- **Linewidth, free spectral range (FSR), finesse:**

Now, let's focus on the transmitted light from a cavity. Suppose the incident light has a continuous frequency distribution and mode matched to the cavity. In that case, the transmitted light has a comb-like distribution, i.e., the cavity only allows light with frequencies satisfying resonance conditions to pass through. Each comb line has a distribution in the frequency domain, which is called linewidth. The linewidth is defined by the full-width at half-maximum of each comb line:

$$f_{FWHM} = \frac{2c}{\pi L} \arcsin \left(\frac{1 - \sqrt{R_1 R_2}}{2(R_1 R_2)^{1/4}} \right), \quad (4.15)$$

where $R_1 = r_1^2$ and $R_2 = r_2^2$.

Each transmitted comb line is separated from its neighbor by a certain spacing in the frequency domain. This is called the free spectral range (FSR), or mode spacing, and is defined as:

$$FSR = \frac{c}{L}. \quad (4.16)$$

The linewidth and FSR above are represented in the frequency domain, f , which is in units of Hz, and they can be converted from frequency domain to the phase domain, δ , which is in units of radian, by the relation between round trip phase shift and frequency, $\delta = \frac{2\pi f L}{c}$. We then have linewidth in the phase domain

$$\delta_{FWHM} = 4 \arcsin \left(\frac{1 - \sqrt{R_1 R_2}}{2(R_1 R_2)^{1/4}} \right), \quad (4.17)$$

and the FSR in phase domain

$$\Delta\delta = 2\pi. \quad (4.18)$$

Figure 4.4 plots the transmittance T as a function of round trip optical phase δ for a symmetric cavity with $R_1 = R_2 = 0.95$.

The finesse is defined as a ratio of the FSR over the FWHM:

$$\begin{aligned} Finesse &= \frac{\Delta\delta}{\delta_{FWHM}} = \frac{FSR}{f_{FWHM}} \\ &= \frac{\pi}{2 \arcsin \left[\frac{1 - \sqrt{R_1 R_2}}{2(R_1 R_2)^{1/4}} \right]}. \end{aligned} \quad (4.19)$$

Remark: a high finesse cavity is usually used as an optical filter, such cavity is called a filter cavity. For example, one can use a filter cavity to clean and narrow the spectra of a laser beam.

4.2 Nonlinear Medium

A great reference for the physics of nonlinear medium is the Nonlinear Optics by Robert W. Boyd and Pei Wang's thesis [59], and here I provide a brief recap.

In the case of conventional optics, the polarization depends linearly on the electric field strength:

$$P(t) = \epsilon_0 \chi^{(1)} E(t), \quad (4.20)$$

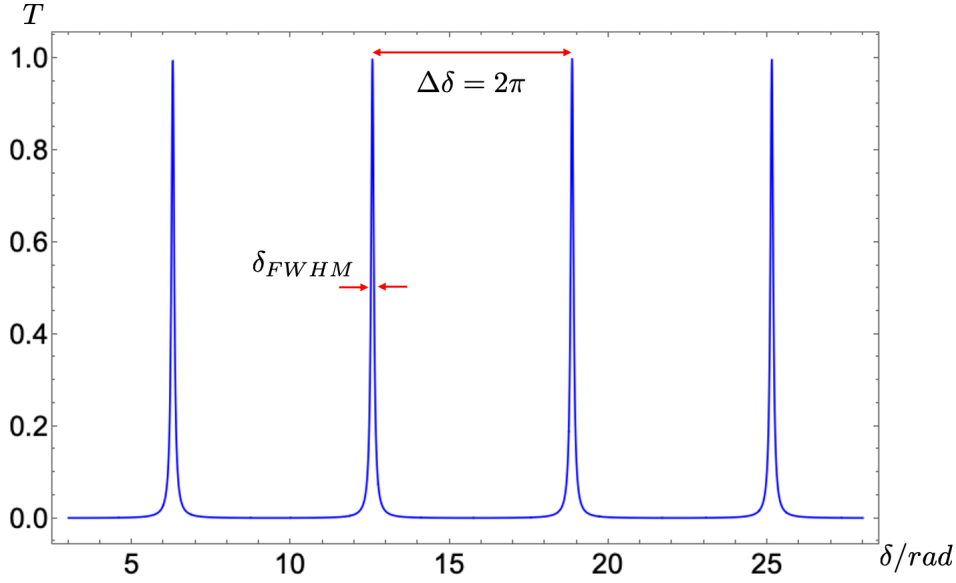


Figure 4.4: The transmittance T is a function of round trip optical phase δ for a symmetric cavity with $R_1 = R_2 = 0.95$.

where $\chi^{(1)}$ is the linear susceptibility, and ϵ_0 is the permittivity of free space. In nonlinear optics, the induced polarization $P(t)$ can be expressed by a power series in the field strength $E(t)$ as

$$\begin{aligned} P(t) &= \epsilon_0[\chi^{(1)}E(t) + \chi^{(2)}E^2(t) + \chi^{(3)}E^3(t) + \dots] \\ &= P^{(1)}(t) + P^{(2)}(t) + P^{(3)}(t) + \dots, \end{aligned} \quad (4.21)$$

where $\chi^{(2)}$ and $\chi^{(3)}$ are the second- and third-order nonlinear optical susceptibilities. $P^{(2)}(t)$ is referred to as the second-order nonlinear polarization and $P^{(3)}(t)$ is referred to as the third-order nonlinear polarization. The physical requirement for $P^{(2)}(t)$ to occur is distinct from the physical requirement for $P^{(3)}(t)$ to occur: the second-order nonlinear optical interaction cannot occur in crystals that do not display inversion symmetry (centrosymmetric crystals); the third-order nonlinear optical interaction can occur for both centrosymmetric and noncentrosymmetric media. In general, $P^{(1)} \gg P^{(2)} \gg P^{(3)}$, so when we consider the second-order nonlinear optical interaction, we can neglect the effect from third-order nonlinear interaction. Therefore, we can only consider the second-order nonlinear optical interaction in the following.

Consider two optical fields, $E_1e^{i\omega_1t}$ and $E_2e^{i\omega_2t}$, pass through a $\chi^{(2)}$ nonlinear crystal, the second-order nonlinear polarization becomes

$$\begin{aligned} P^{(2)} &= \chi^{(2)}(E_1e^{i\omega_1t} + E_2e^{i\omega_2t})^2 \\ &= 2\chi^{(2)}E_1E_2e^{i(\omega_1+\omega_2)t} + \chi^{(2)}(E_1^2e^{i(2\omega_1t)} + E_2^2e^{i(2\omega_2t)}). \end{aligned} \quad (4.22)$$

The first term implies there is a new field generated with a frequency equal to the sum of two input fields, so-called sum-frequency generation. A sum-frequency generation is an up-conversion process (from a frequency perspective) and it is a reversible process, which is called parametric down-conversion (PDC). Figure 4.5 illustrates the idea of the sum-frequency generation. The intensity of the new field:

$$I_3 \propto L^2 \text{sinc}^2(\Delta kL/2), \quad (4.23)$$

where L is the length of the nonlinear crystal and Δk is the phase match.

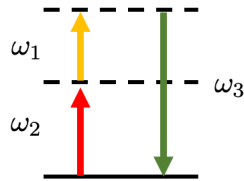


Figure 4.5: Sum frequency generation: converting two fields with frequencies ω_1 and ω_2 into new field with frequency $\omega_3 = \omega_1 + \omega_2$. It is also known as an up-conversion process.

Assume three waves are propagating collinearly, to maximize the intensity of the new field, i.e., maximize the conversion efficiency, the **phase matching conditions** needs to be satisfied, that is energy conservation:

$$\omega_3 = \omega_2 + \omega_1, \quad (4.24)$$

and momentum conservation:

$$\Delta k = k_1 + k_2 - k_3 = 0, \quad (4.25)$$

where ω_3 is the frequency of new filed and $k_i = \frac{n_i \omega_i}{c}$ is the wave vector for i -th field, $i = 1, 2$, or 3 .

However, due to the dispersion, $\Delta k \neq 0$. One way to circumvent this issue is **quasi-phase matching**. To achieve the quasi-phase matching, it is necessary to create additional spatial oscillation of nonlinear efficiency, for example, by periodically inverting the c axis of a ferroelectric material, thus flipping the sign of $\chi^{(2)}$ and generating a new term in wavevector to compensate the mismatch. Figure 4.6 shows schematic representations of a regular nonlinear crystal (4.6a) with a periodically poled crystal (4.6b). Therefore, the wavevector mismatch is given by

$$\Delta k_Q = k_1 + k_2 - k_3 - 2\pi/\Lambda. \quad (4.26)$$

The requirement of $\Delta k_Q = 0$ and Eq. (4.23) determine a continuous frequency range, also known as quasi-phase matching bandwidth (QPBW), for converting efficiently between field 1 and field 2 to field 3 (and vice versa). By using temperature-dependent Sellmeier equations [17, 21], one can find the suitable polling period and crystal temperature for particular frequencies with a very broad QPBW for efficient conversion.

4.3 Quantum Optical Frequency Comb

The OPO used in this thesis is a four-mirror one-sided cavity with a $\chi^{(2)}$ PPKTP nonlinear crystal inside. Figure 4.7 illustrates the schematic representations of OPO (4.7a) and the real setup when the pump beam is injected (4.7b). The OPO mirrors were fabricated by Advanced Thin Films. The cavity is constituted by two concave mirrors (50 mm radius) and two flat mirrors. One of the flat mirrors is the output coupler (1st mirror), which was a 5% transmittance mirror at 1064 nm and 0.05% at

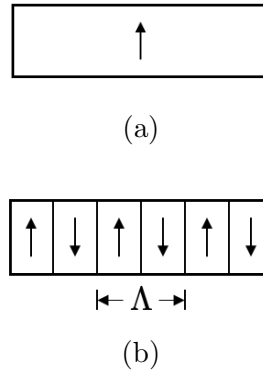


Figure 4.6: Schematic representations of a nonlinear crystal. (a) a homogeneous single crystal and (b) a periodically poled crystal. The arrows represent the positive c axis, and Λ represents the polling period.

532 nm. Later, the 1st mirror was changed to a 17% transmittance mirror at 1064 nm and less than 0.01% at 532 nm, for the purpose of increasing squeezing. All other mirrors have a transmittance of near-zero at 1064 nm and near-unity at 532 nm. The cavity has an FSR of about 1 GHz, and it is stabilized by Pound-Drever-Hall cavity lock to a weak counterpropagating beam, which is called a locking beam. The OPO linewidth was about 10 MHz before but increased to 36 MHz after changing the output coupler. The four-mirror one-sided cavity has two beam waists, based on eigenmode calculation, one waist is $35 \mu\text{m}$ (between 2nd and 3rd curved mirrors), and the other waist is $135 \mu\text{m}$ (between 1st and 4th flat mirrors). The PPKTP nonlinear crystal is placed at $35 \mu\text{m}$ waist place.

The PPKTP crystal is a $\chi^{(2)}$ nonlinear crystal and was provided by Raicol Crystals. The crystal is an x-cut, $1 \times 2 \times 10 \text{ mm}^3$ in size, and $9 \mu\text{m}$ polling period (at room temperature) so as to quasiphasematch zzz PDC [18, 46, 47] (zzz stands for the polarization of pump beam is in z-polarization, and the polarization of signal and idler are also in z-polarization). The crystal has antireflection coated by Advanced Thin Films at 1064 nm and 532 nm, and it is temperature-stabilized such that the PDC efficiency is maximized. The Quantum Fields and Quantum Information (QFQI) group at the University of Virginia has performed a theoretical and experimental investigation about the QPBW of the crystal [60], and it has been shown the QPBW is about 3.18 THz. The reset of the experiment detail can be found in Moran Chen's thesis [12].

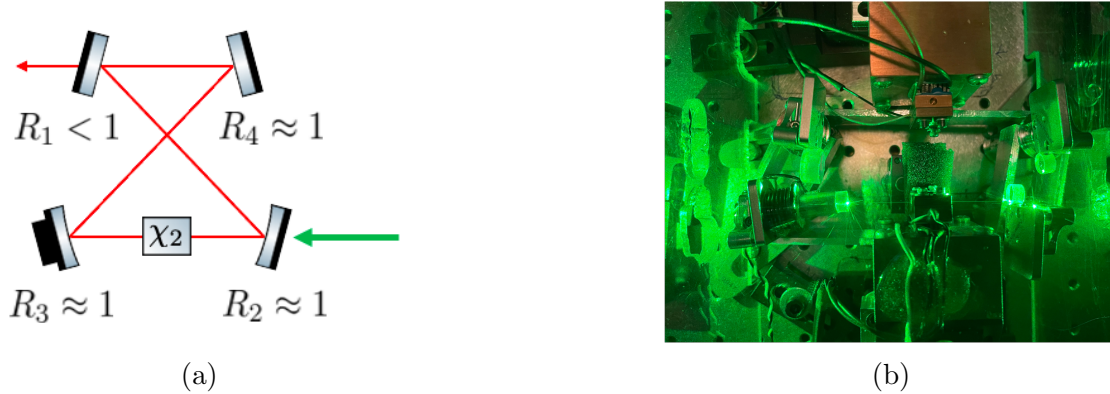


Figure 4.7: A four-mirror one-sided OPO. (a) a schematic representation of OPO. R_i is the intensity reflection of i -th mirror at 1064 nm. (b) a real setup of OPO when the pump beam is injected. The pump beam is at a wavelength of 532 nm.

The operation principle is in the following: by sending a 532 nm laser light as the pump field (field 3 in the previous section) with its power below the OPO lasing threshold, a spontaneous parametric down-conversion (SPDC) will happen. SPDC converts the pump beam photon into two photons with lower frequencies (field 1 and field 2 in the previous section), which are now called signal and idler. Figure 4.8a illustrates the idea of SPDC. The frequencies of signal and idler are the same as the quasi-phase matching bandwidth, which is a continuous distribution over 3.2 THz in this experiment. However, because there is an optical cavity surrounding the non-linear crystal, and the optical cavity only allows certain frequencies of fields (signal and idler) satisfying the resonance condition to build up. The fields building up in the cavity stimulate the down-conversion process and generate more resonance fields and then come out from the output coupler. Therefore, in the frequency domain, the emission spectrum of OPO looks like an optical frequency comb. The spacing between each comb line (FSR) is about 1 GHz. Considering the mechanism of PDC, creating the signal and idler photons by annihilating the pump photon, the Hamiltonian is, in general, the two-mode squeezing Hamiltonian, Eq. (2.80). There is some quantum correlation between signal and idler as discussed in subsection (2.6.2). The emission spectrum of OPO is actually a bunch of two-mode squeezing pairs, which are evenly distributed around the half frequency of the pump. Therefore the output modes are called quantum optical frequency comb (QOFC). Figure 4.8b illustrates the QOFC in the frequency domain, which is nothing but many two-mode squeezing pairs. The curved red lines represent the quantum correlation (entanglement) between the signal and idler fields, and the green arrow represents the half frequency of the pump.

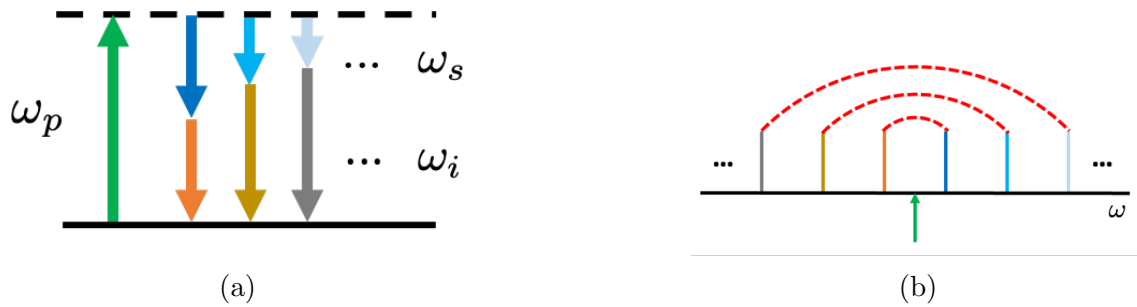


Figure 4.8: The principles behind the OPO output fields. (a) SPDC converts the pump photon into signal and idler photons, whose frequency range is the same as the QPBT; (b) The emission spectrum of OPO generates many two-mode squeezing pairs, which is called quantum optical frequency comb (QOFC). The dashed curved lines represent the entanglement. The green arrow in the center represents the half frequency of the pump.

4.4 Pound-Drever-Hall (PDH) Locking

4.4.1 Introduction of PDH Locking

The Pound-Drever-Hall (PDH) is an elegant and powerful approach to stabilize the frequency of laser light. In this experiment, the PDH locking is used to lock the OPO cavity to a 1064 nm laser light (locking beam), which is phase locked to a 532 nm pump laser, such that the cavity can follow the 1064 nm laser and stay resonance.

There are two advantages of using PDH locking rather than another kind of locking method:

- (1) PDH locking can lock the laser to the center of the resonance peak due to it providing a cavity phase response (as figure 4.3 shows) like an error signal.
- (2) PDH locking is insensitive to the slow drift of laser power.

Here I briefly summarize the paper by Eric D. Black for the introduction of PDH cavity locking [6].

Figure 4.9 shows the basic layout for a PDH cavity lock to a laser. The principle is when a monochromatic laser light (carrier) passes through a phase modulation device (ex: Pockels Cell or EOM), which generates sidebands around the carrier. When the modulation amplitude is small, we can only consider the first-order sidebands with frequencies blue-shifted and red-shifted from the carrier frequency by one modulation frequency. Moreover, one sideband is in phase with the carrier while the other sideband is out of phase with the carrier. As the carrier and two sidebands hit on the cavity, the reflection due to the cavity not only reflects the light in different magnitudes, it also introduces different phase responses (as figure 4.3 shows) to the carrier and two sidebands. By using a photodetector to receive the reflected carrier and two sidebands, we can get a signal containing a beat note signal. The beat note signal actually comes from the reflected carrier and reflected two sidebands. Thus the beat note frequency is the same as the modulation frequency. By using a mixer to demodulate the photodetector signal by the same modulation signal, the beat note signal can be extracted, which is very similar to the phase response of the

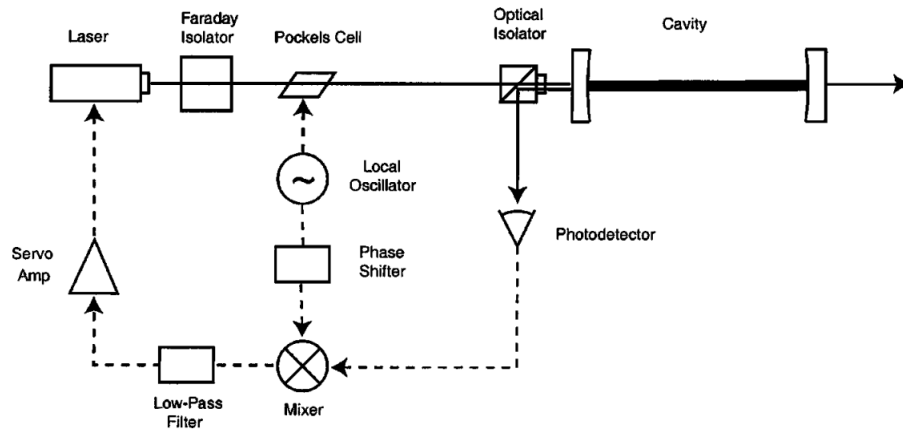


Figure 4.9: The basic layout for PDH cavity locking to a laser. Solid lines are optical paths, and dashed lines are signal paths. The signal going to the laser controls its frequency [6].

cavity. Depending on the frequency of modulation signal and linewidth of the cavity mode, the error signal might have a slight difference, as figure 4.10 shows. Hence, the demodulated beat note signal can be used as the error signal to lock the laser frequency to the center of the cavity mode, which is also the zero point of the error signal. The full mathematical treatment can be found in [5, 6, 15].

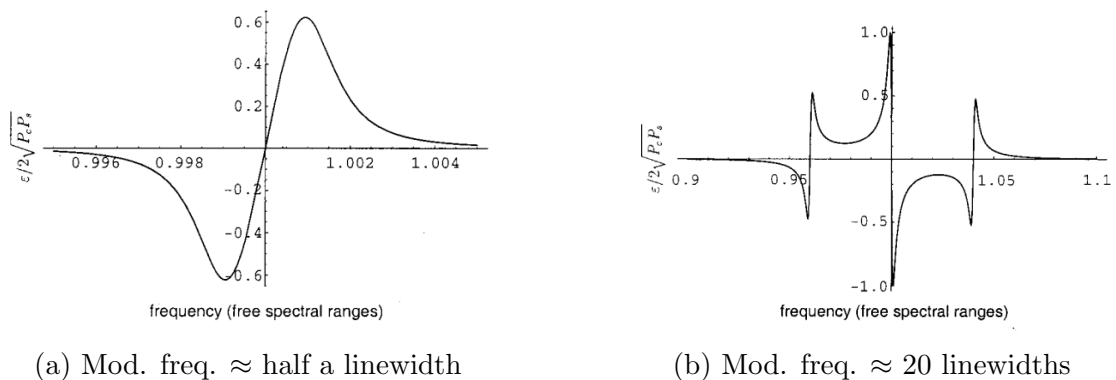


Figure 4.10: The PDH error signal v.s. modulation frequency (normalized to the linewidth of mode) when (a) the modulation frequency is low; (b) the modulation frequency is high. The cavity finesse is 500 [6].

The schematic setup for the OPO PDH cavity lock in the experiment is shown in figure 4.11a. The 532 nm pump beam and 1064 nm locking beam come from the same laser. Hence they are phase locked. The laser itself has a weak 12 MHz phase modulation that can be used to perform the PDH lock. The corresponding output quantum optical frequency comb looks like figure 4.11b, which is different from the QOFC in figure 4.8b.

Note: to generate the QOFC like figure 4.8b, one can install an EOM in the locking beam path. By setting the modulation frequency to 0.5 FSR with strong enough modulation depth, one can lock the OPO onto one of the first-order sidebands to generate QOFC as figure 4.8b.

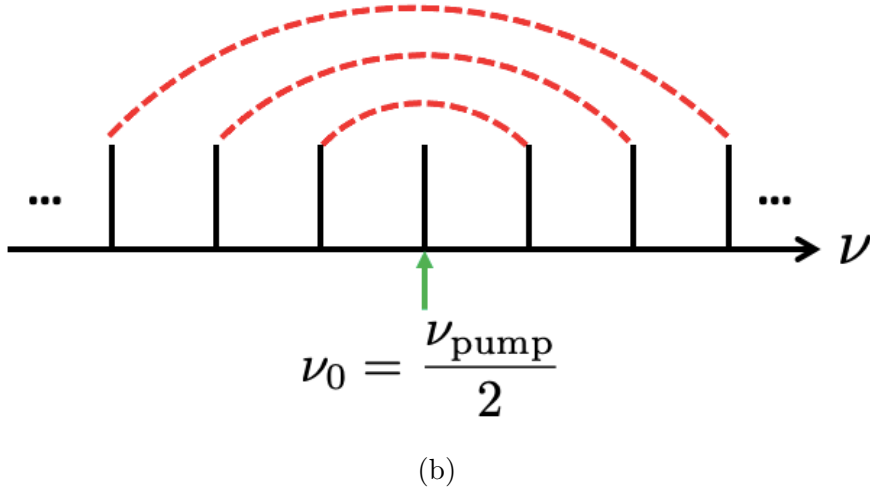
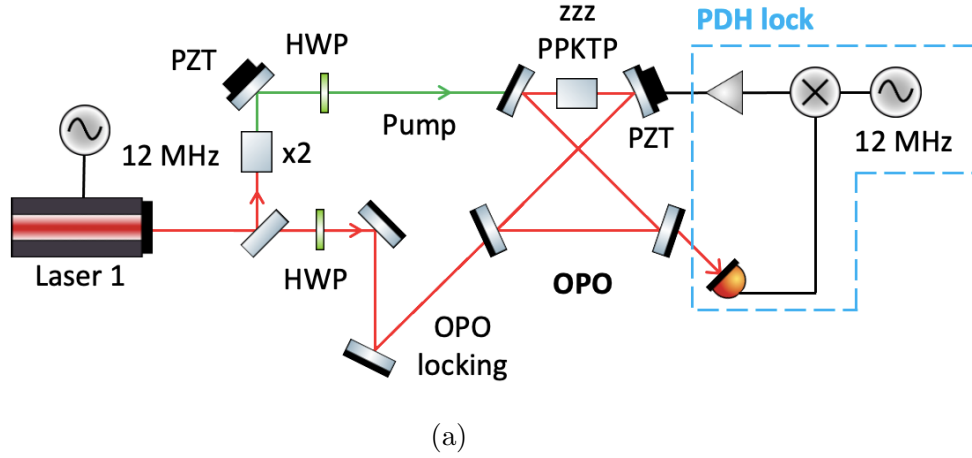


Figure 4.11: (a) schematic setup for OPO PDH cavity lock in the experiment. (b) the corresponding emission spectrum of OPO. The green arrow represents the half frequency of the pump.

4.4.2 Signal-to-Noise Ratio of PDH Lock

To minimize the phase noise coming from the OPO cavity (recall the cavity response showed in figure 4.3), the PDH lock needs to have the best possible signal-to-noise ratio (SNR). The higher the SNR of the PDH lock, the more stable the OPO cavity is and, thus, the more minor phase noise introduced by the OPO cavity to the squeezed light. The SNR of a PDH lock can be defined as follows

$$\text{SNR} = \frac{2\sqrt{2}V_{pp}}{V_{pp}^{\text{noise}}} = \frac{f_{FWHM}}{\delta_{lock}}, \quad (4.27)$$

where V_{pp} is the peak-to-peak value of the PDH lock error signal, V_{pp}^{noise} is the peak-to-peak value of the noise in PDH lock error signal, f_{FWHM} is the cavity linewidth,

Eq. (4.15) and δ_{lock} is residual locked frequency bandwidth, which is a quantity of how tight the PDH locking is.

4.5 Parametric Gain and Squeezing

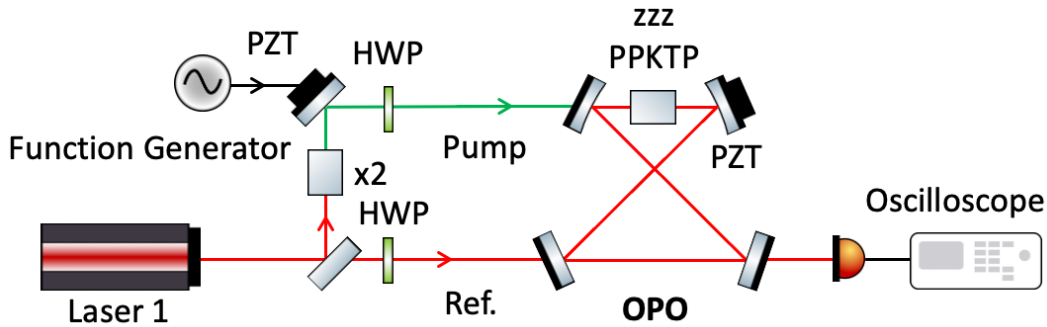


Figure 4.12: Schematic setup for measuring the parametric gain by injecting the 1064 nm reference beam (red line) and 532 nm pump beam (green line) to the OPO. The detector after the output coupler is measuring the reference beam power and monitors the signal by an oscilloscope. Ref.: reference beam.

Considering the following ideal scenario: when a stable and strong 532 nm pump beam and a stable 1064 nm beam, called reference beam, are both injected into a frequency stabilized OPO, if there is a relative phase change between two fields, the power of the transmitted reference beam will be amplified and deamplified depending on the relative phase. This phenomenon is called parametric amplification and deamplification. The ratio of the maximal power of the amplified transmitted reference beam to the power of reference beam with no pump is the (parametric) gain, and the strength of gain determines the maximal amount of squeezing. Figure 4.12 shows the schematic setup for measuring the parametric gain by injecting the 1064 nm reference beam (red line) and 532 nm pump beam (green line) to the OPO at the same time. Here, I will provide the derivation.

Start with the single-mode squeezing Bogoliubov transformation, Eq. (2.69), which describes the time evolution of the vacuum field influenced by the pump field. Here, we can rewrite the Eq. (2.69) to describe the time evolution of the reference beam influenced by the pump. Because the reference beam is a classical light, we can take

$$a \rightarrow \alpha e^{i\theta}, \quad (4.28)$$

where α is a real number, and assume $\theta = 0$ for simplicity, we then have

$$\alpha(t) = \alpha \cosh r + \alpha^* e^{i\phi} \sinh r. \quad (4.29)$$

By using a detector to collect the reference beam, we can get the photon number of the reference beam

$$\begin{aligned}
 & \alpha(t)\alpha^*(t) \\
 &= (\alpha \cosh r + \alpha^* e^{i\phi} \sinh r)(\alpha^* \cosh r + \alpha e^{-i\phi} \sinh r) \\
 &= |\alpha|^2(\cosh^2 r + \sinh^2 r) + (\alpha^2 e^{-i\phi} + (\alpha^*)^2 e^{i\phi}) \cosh r \sinh r \\
 &= |\alpha|^2(\cosh^2 r + \sinh^2 r) + |\alpha|^2 \sinh 2r \cos \phi.
 \end{aligned} \tag{4.30}$$

When $\phi = 0$, we can get the maximum photo number

$$\begin{aligned}
 (\alpha(t)\alpha^*(t))_{max} &= |\alpha|^2(\cosh 2r + \sinh 2r) \\
 &= |\alpha|^2 e^{2r}.
 \end{aligned} \tag{4.31}$$

Therefore, the gain due to the parametric amplification is defined as

$$\text{Gain} = \frac{(\alpha(t)\alpha^*(t))_{max}}{|\alpha|^2} = e^{2r}. \tag{4.32}$$

In fact, we can measure the gain even when the cavity is scanning as long as the phase of pump, ϕ , is changing faster than the cavity scan rate. Figure 4.13 is a real example of gain estimation. In the condition of OPO scanning by a 10 Hz and 3 V_{pp} ramp (to the PZT driver), figure 4.13a shows the reference beam signal without pump beam, and figure 4.13b shows the reference beam signal with pump beam, whose phase is scanned by a 123 Hz and 5 V_{pp} ramp to the PZT driver. By taking the ratio of maximum value in two different cases, we can conclude the $\text{Gain} = 194.25 \text{ mV}/46.5 \text{ mV} = 4.18 = e^{2r}$. Therefore, we can find out the squeezing parameter, r , is 0.72, and the corresponding squeezing (SQ) in dB can be calculated by

$$\text{SQ}(r) = 20 \log_{10} e^r, \tag{4.33}$$

and the squeezing is 6.2 dB.

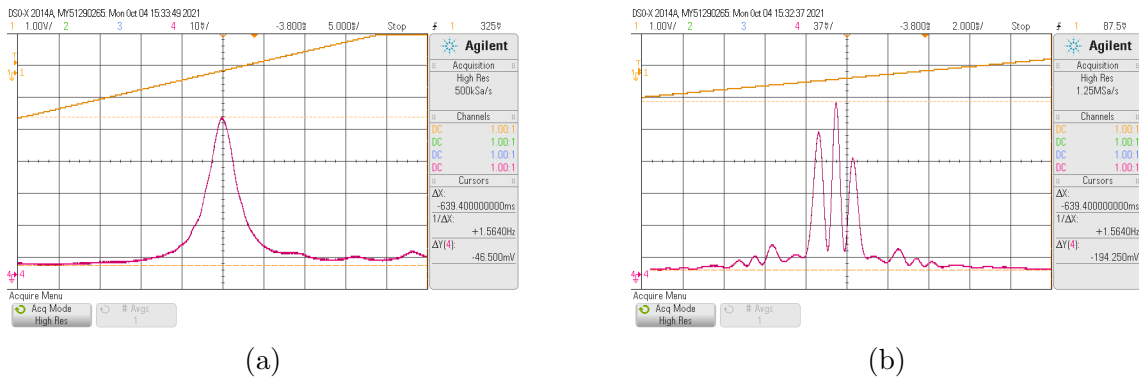


Figure 4.13: reference beam signal (red line) in the condition of (a) without pump beam and (b) with pump beam when OPO cavity is scanned by a 10 Hz and 3 V_{pp} ramp (yellow line) to the PZT driver. The pump beam phase is also scanned by a 123 Hz and 5 V_{pp} ramp to the PZT driver. The different peaks in (b) are because of the pump phase scanning faster than cavity scan rate. Also, notice the peak value in (a) is 46.5 mV while the peak value in (b) is 194.25 mV.

Chapter 5

Old OPO setup

In this chapter, the author will discuss the phase noise investigation and some performance improvements performed to the optical system to increase squeezing and provide preliminary evidence for our EOM method of generating 1-d cluster states.

5.1 Phase Noise Investigation

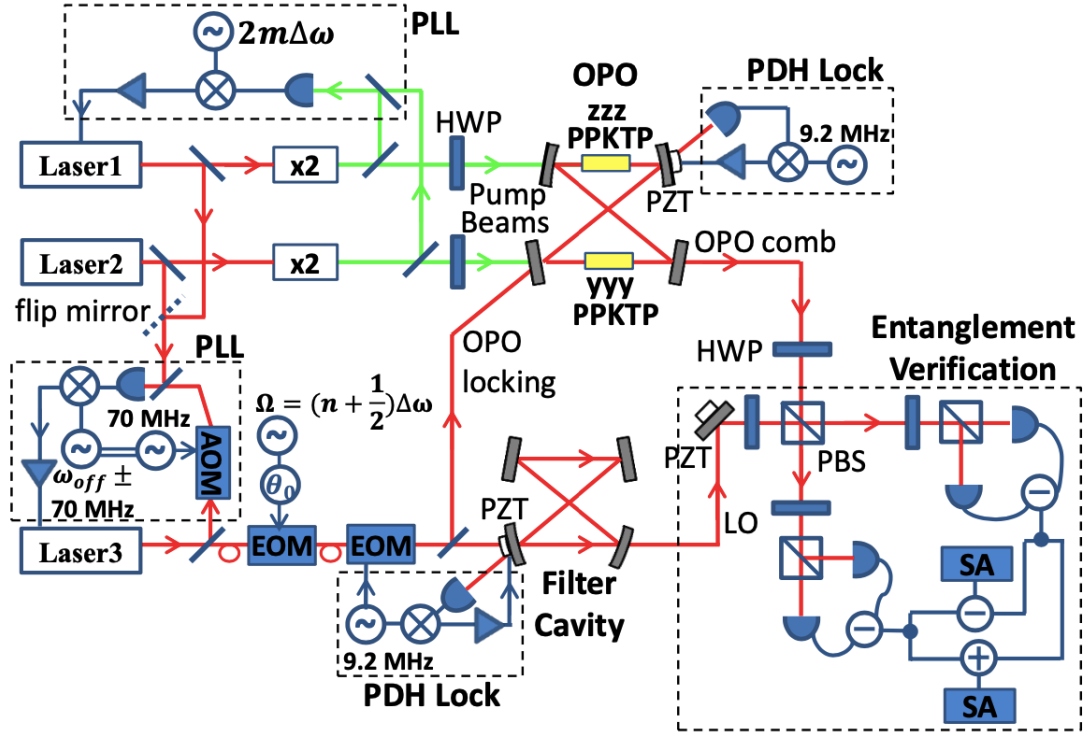


Figure 5.1: Former experimental setup for generating 1-d dual-rail wire cluster state [12, 13]. PLL: phase lock loop; HWP: half-wave plate; PZT: piezoelectric transducer; PBS: polarizing beam splitter; SA: spectrum analyzer; AOM: acousto-optic modulator; EOM: electro-optic modulator; PDH: Pound-Drever-Hall lock loop; x2: frequency doubling crystal.

Figure 5.1 shows the former experimental setup for generating a 1-d dual-rail wire cluster state, which was generated by entangling two QOFC in two different polar-

a phase noise that degraded the squeezing. A phase noise investigation was thus performed: by interfering two laser lights from two different PZT locations and scanning the relative phase slowly (0.2 Hz and 5 V_{pp} applied the PZT driver), we can directly measure the amount of phase noise and its corresponding frequency, as discussed in subsection 2.6.4. Figure 5.3 shows an example of measuring the phase noise between laser 1 before the OPO (purple square 1) and laser 3 after the filter cavity (blue square D).



Figure 5.3: Interference of laser 1 before OPO and laser 3 after the filter cavity: (a) interference fringe when relative phase scanned slowly; (b) zoomed-in of the half-maximal of the fringe, which is the average of fringe, and the phase noise can be measured directly. The peak to peak value of fringe is 357.5 mV while the noise peak to peak value at half-maximal of the fringe is 49.375 mV (denoted by two horizontal dashed cursor lines). By employing Eq. (2.102), the phase noise can be determined and it is 7.8°.

Table 5.1 summarizes the investigation results and a 9.5° of phase noise might hinder our squeezing measurement. Another interesting finding is that the phase noise increased after the laser beam passed through either cavity. As we discussed in subsection 4.4.2, the increasing phase noise after cavities is possibly due to the low SNR of the PDH lock for the two cavities. In the later section, we will show the improvement of the OPO PDH lock, which increased the SNR from 40 to more than 3000, and the corresponding phase noise can be further reduced. We can follow the discussion in subsection 2.6.4, and if we assume the squeezing generated by the OPO is 3.2 dB. Then, with a phase noise of 9.5°, the observed squeezing will be dropped to 2.8 dB, which is different from the 1 dB of squeezing we observed in figure 5.4.

The possible reasons why we only measured 1 dB of squeezing might come from (1) the imperfection in phase lock loop (PLL) between laser 1 and laser 3, and (2) the OPO and FC PDH lock. The PLL between laser 1 and laser 3 was used to make laser 1 and laser 3 have the same frequency. Figure 5.5 shows the simplified schematic experimental setup for the PLL between laser 1 and laser 3. The PLL was achieved by shifting the frequency of laser 3 by 70 MHz (with the aid of acousto-optic modulator (AOM)) and then combining the frequency-shifted laser 3 beam with laser 1 beam. A large bandwidth photodetector was used to measure the 70 MHz beat note and its photocurrent signal was sent to a servo loop to lock the 70 MHz beat note to a 70 MHz signal source. The error signal was feedback to laser 3 to stabilize its output frequency. Therefore, to check the performance of PLL, we sent the 70 MHz beat note and the 70 MHz signal source, which is coming from two phase-

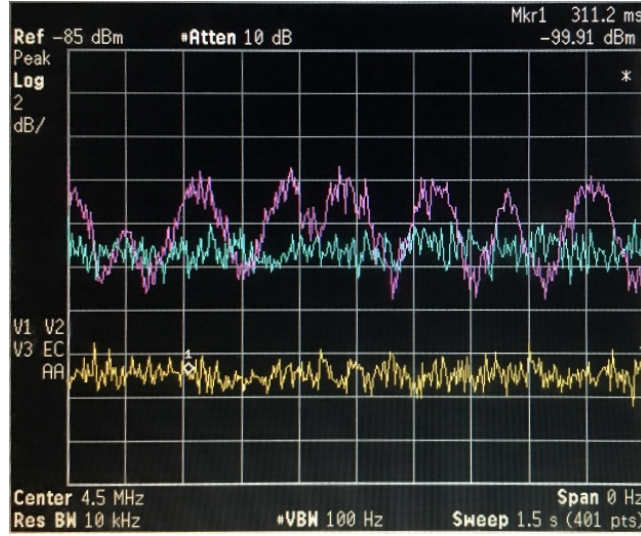


Figure 5.4: The first attempt to observe squeezing and the squeezing level is about 1 dB. Yellow trace: electronic noise; Blue trace: shot noise; Red trace: squeezing trace.

Results of Phase Noise Investigation			
Laser 1	Laser 3	Noise Freq./Hz	Noise Angle/degree
2	D	700	9.5
1	D	~ 100	7.8
1	A	170	2.9
1	B	200	2.9
1	C	200	2.9, 3.8
2	C	724, 180	2.9 (fast freq.) 7.19 (slow freq.)

Table 5.1: Results of phase noise investigation. The corresponding interference places for laser 1 and laser 2 are marked in figure 5.2 by purple boxes with numbers and blue boxes with letters. FC: filter cavity.

locked synthesizers (one for modulation purposes and the other for demodulation purposes), to a spectrum analyzer (SA). The detail of the PLL between laser 1 and laser 3 can be found in Moran Chen's thesis [12]. Figure 5.6 shows the measurement results from SA and one can see the three signals have exactly the same frequency within the SA 1 Hz resolution, which implies the PLL works quite well. However, as we switched the OPO locking beam from laser 1 to laser 3, and checked the squeezing again, we can observe more than 3 dB of squeezing, as figure 5.7 shows. The corresponding phase noise measured was about 3.8° . We can perform the phase noise analysis again: assuming the OPO generated 3.2 dB of squeezing, the 3.8° phase noise degrades the observed squeezing to 3.1 dB, which implies phase noise of 3.8° in the current case. These results implied there was some limitation on the PLL, thus some phase noise did exist.

In order to better understand the phase noise, we sent the interference signal from a detector to the spectrum analyzer to check the spectrum of phase noises. Figure 5.8a shows the spectrum of phase noises, which contains multiple noises with

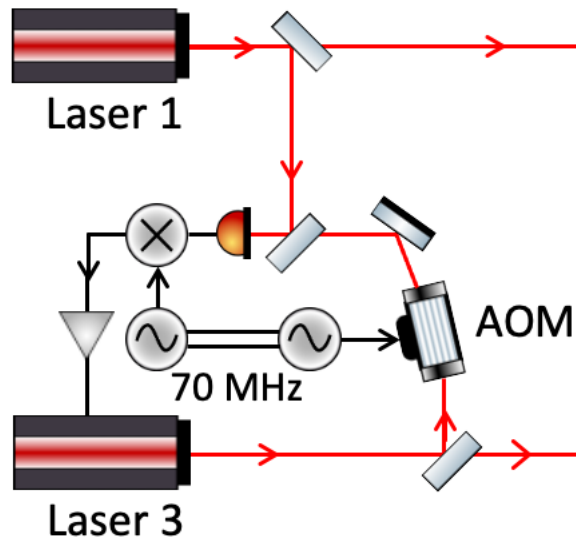


Figure 5.5: Simplified schematic experimental setup for the PLL between laser 1 and laser 3.

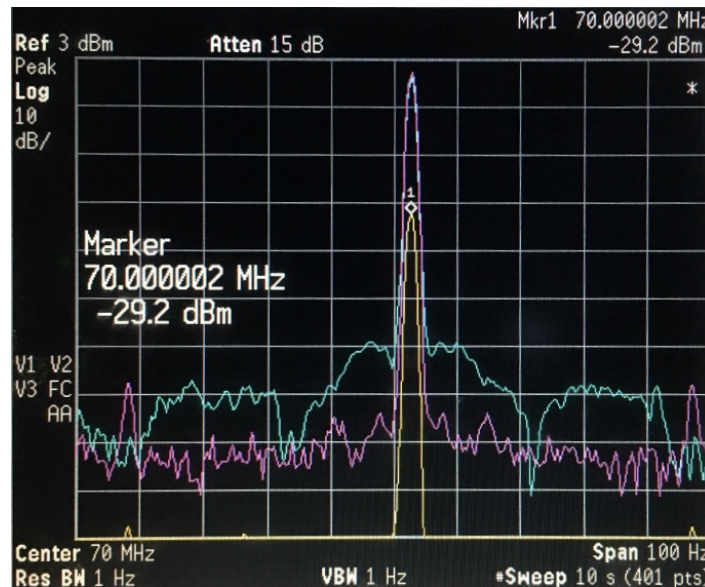


Figure 5.6: Checking the 70 MHz signals by a SA. Yellow trace: 70 MHz beat note; Blue and Red traces: 70 MHz signals from two synthesizers.

different frequencies as marked in the figure. To check the PLL, we sent the error signal, while the PLL was not activated, to the spectrum analyzer to check the error signal's spectrum. Figure 5.8b shows the spectrum of the PLL error signal and one can see it also contains multiple signals with different frequencies: By comparing figure 5.8a and 5.8b, we can conclude the phase noises mostly come from the PLL, and the frequencies of noises imply they are coming from the AC unit, which are power line noises and they are hard to get rid of. Therefore, we locked our OPO cavity and filter cavity by the same laser (laser 3) from now on, which was the original locking scheme as the former experimental setup, figure 5.1, to reduce the phase noise. Also note the noise on the laser 3 still matter, so for the work presented

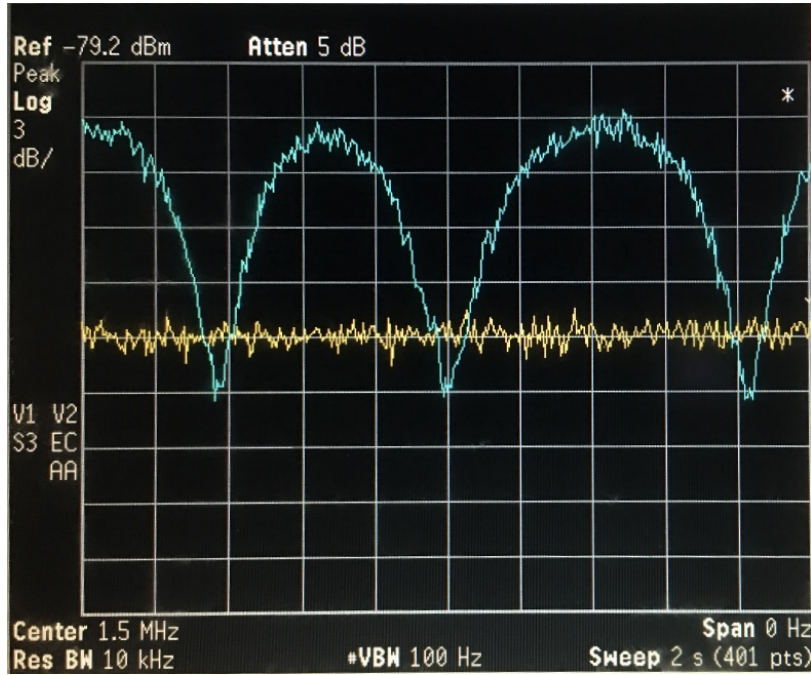


Figure 5.7: Squeezing measurement after switching the locking beam from laser 1 to laser 3. Yellow trace: shot noise; Blue trace: squeezing signal.

in chapter 6, we modified the optical system by removing the filter cavity and using laser 1 only for the OPO locking beam, reference beam, and LO.

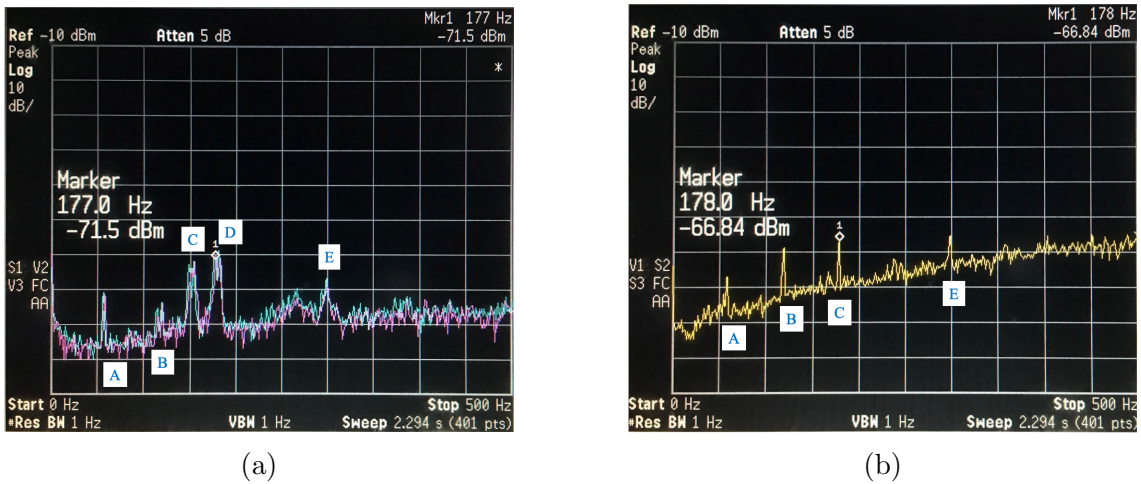


Figure 5.8: Spectra of (a) interference fringe signal and (b) PLL error signal when PLL was not activated. The frequencies of peaks are: (A) 60 Hz, (B) 120 Hz, (C) 200 Hz, and (E) 298 Hz. The blue trace and red trace are the cases of different gains in the filter cavity PDH lock servo.

5.2 OPO PDH Cavity Locking Improvement

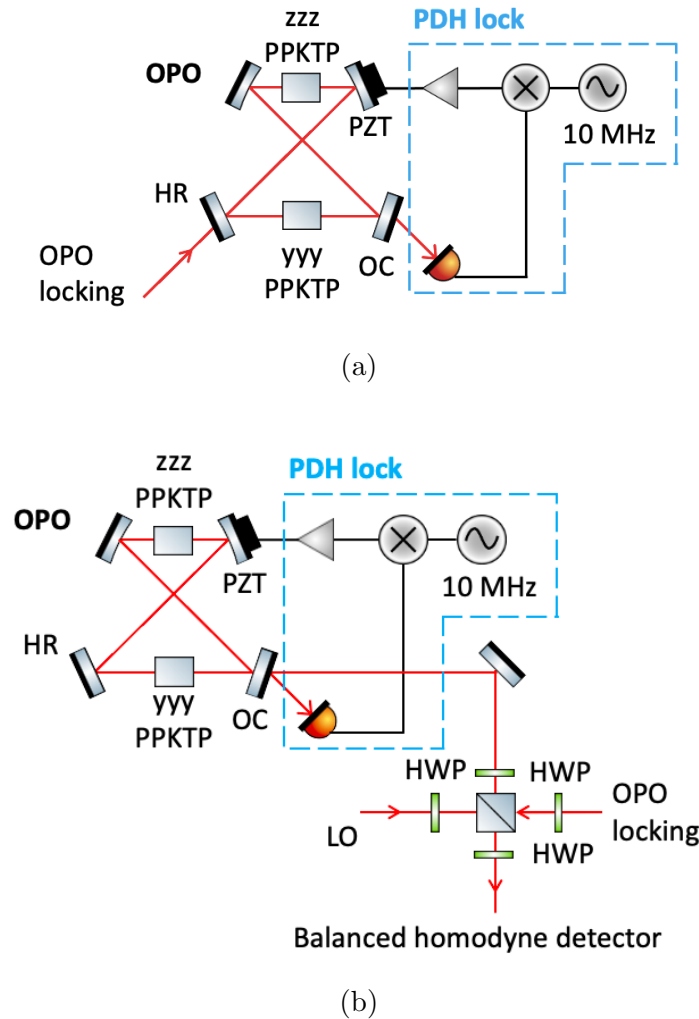


Figure 5.9: Two types of OPO locking beam injection. (a) locking beam is injected from one of the HR mirrors; (b) locking beam is injected from the unused port of PBS to the output coupler.

To minimize the phase noise coming from the OPO cavity (recall the cavity response showed in figure 4.3), the PDH lock needs to have the best possible signal-to-noise ratio (SNR). The higher the SNR of the PDH lock, the more stable the OPO cavity is. Previously, as figure 5.9a shows the simplified schematic setup, the locking beam was in the same polarization as the pump beam and was injected from one of the HR mirrors, thus the transmitted signal was quite weak due to weakly transmitted carrier and sidebands. Therefore, the SNR was about 40. To increase the PDH locking SNR, it was natural to inject the locking beam from the output coupler mirror, due to the fact that the sidebands are off-resonance and hence sidebands are much more reflected than transmitted. Moreover, the carrier gets reflected less at the output coupler, so the beat note signal is stronger when measuring the reflected signal than the transmitted signal. To achieve the goal, we sent the locking beam from the unused port of PBS, therefore, the locking beam was counter-propagating

with respect to the squeezed light. But, in this way, the polarization of the locking beam was in y-polarization while the squeezed was in z-polarization. Due to the birefringence, the y-polarization and z-polarization wouldn't resonate at the same cavity length. As we discussed in the previous section, since laser 2 was not in service, we don't need to pay too much attention to the birefringence. However, for our new locking beam in different polarization from the polarization of squeezed light, we thus need to compensate the birefringence as we did in generating dual-rail cluster state, figure 5.1: by tuning the temperature of the yyy PPKTP crystal, such that the y-polarization and z-polarization can resonate at the same cavity length. Figure 5.9b shows the schematic setup.

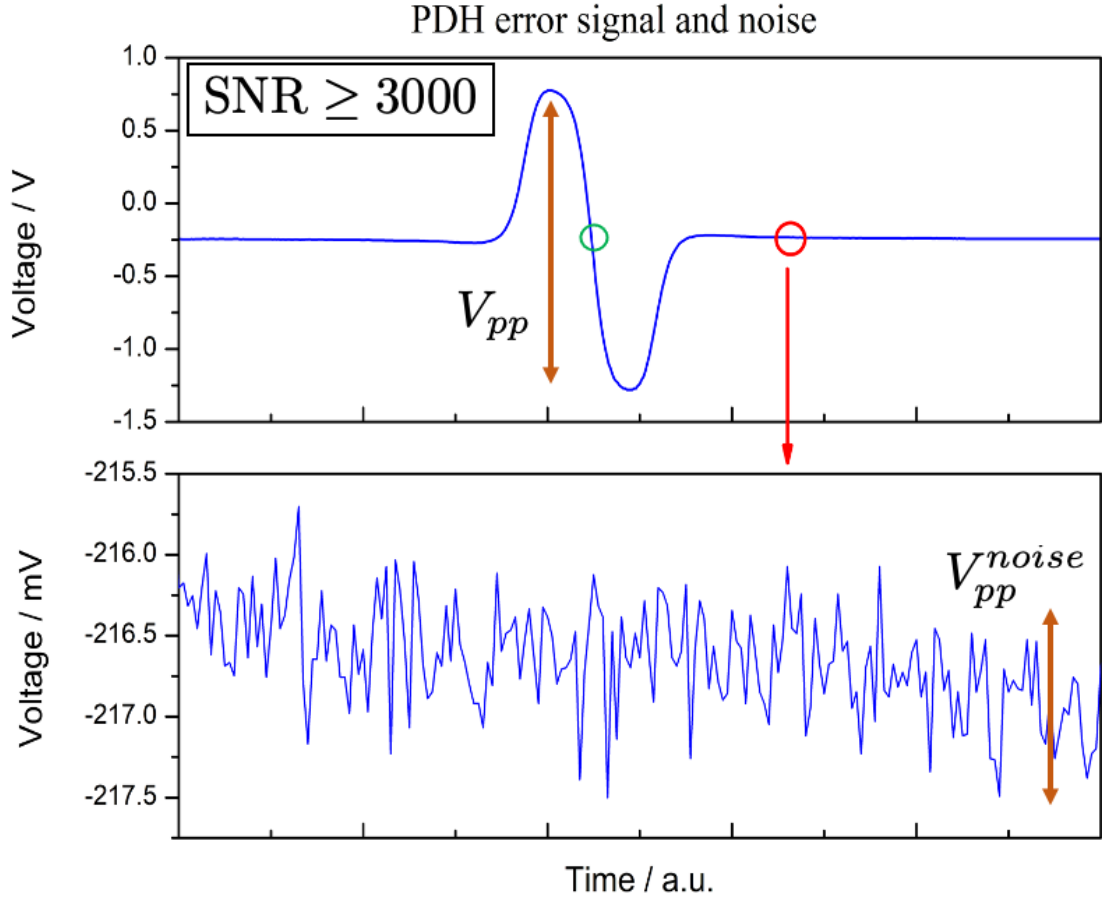


Figure 5.10: The improved PDH cavity locking signal was recorded when OPO cavity length was scanning, therefore, the x-axis is time. Top panel: measured error signal. The green circle represents the locking point, and V_{pp} is the peak-to-peak value of the error signal. Bottom panel: zoomed-in noise (red circle in the top panel). V_{pp}^{noise} is the peak-to-peak value of noise.

The improved PDH cavity locking signal is presented in figure 5.10, and the corresponding SNR is more than 3,000. By using the Eq. (4.27), with the OPO linewidth of about 10 MHz, the δ_{lock} is about 3.3 kHz, which is very close to the linewidth of the CW lasers used in the experiment.

Although the SNR of the cavity lock had been improved, the observed squeezing didn't improve much. As discussed at the end of section 5.1, the phase noise of 3.8° can only decrease the squeezing from 3.2 dB to 3.1 dB, which means a further

Comparison of Old and New PDH Lock		
	Old PDH Lock	New PDH Lock
Properties	LB is injected from OPO HR mirror LB is in the same pol. as QOFC	LB is injected from OPO OFC LB is in the diff. pol. as QOFC
Pros	Doesn't care about the temp. of yyy crystal Better long term stability	High SNR (>3000) Lower phase noise
Cons	Low SNR (~40) Larger phase noise	Require better temp. stability Poor long term stability

Table 5.2: Comparison of old PDH lock and new PDH lock. pol.: polarization; diff.: different; temp.: temperature.

improvement of phase noise wouldn't significantly increase the squeezing. However, it was still worthwhile to improve the PDH locking to prepare for the situation where squeezing is larger, therefore we want to minimize the phase noise as much as we can. In the case of larger squeezing, which is more sensitive to the phase noise, as we discussed in subsection 2.6.4, the improvement showed above can be applied and reduce the phase noise from the cavity.

The other issue about this new OPO PDH lock is the long-term stability: when there was a temperature drift in the two nonlinear crystals, the y-polarization and z-polarization modes wouldn't resonant at the same cavity length. Therefore, with a y-polarization locking beam, that implies the z-polarization is slightly off-resonance, which is equivalent to the loss. Therefore, the observed squeezing can drop from 3.1 dB to 2.7 dB, and the temperature of the crystal needed to readjust. For the squeezing measurement, we can either actively tune the temperature of yyy crystal or simply wait for a long time until the temperature is correct.

Table 5.2 shows the comparison between the old PDH lock and new PDH lock with pros and cons. We will use the new PDH locking scheme from now on until we discuss the covariance matrix measurement setup in section 6.2. Two reasons make us switch the OPO locking scheme and pull out the yyy nonlinear crystal: (1) Reconstructing the covariance matrix requires better long term stability due to the data will be taken for a certain amount of time; (2) We can use the other port of PBS, which is used to inject the new LB, to accomplish the phase lock between the reference beam and pump. See section 6.2 for more details.

Remark: the squeezing we observed here was only about 3.2 dB, comparing it to the 15 dB squeezing paper [56], one major reason is the pump power. In our setup, the pump power we use is 190 mW and the pump is single-passed through the OPO. On the other hand, in the 15 dB paper, the pump power they use is 160 mW and the pump beam resonant to the cavity. Considering the cavity is one-sided and the OC reflection $R = 97.5\%$, the intra-cavity strength of the pump is about 6400 mW, which is about 34 times stronger than the pump power we use. On the other hand, the OC we use is with $T = 5\%$ at 1064 nm, while in the 15 dB paper, they use OC with $T = 12.5\%$ at 1064 nm. The higher the T , the larger the escape efficiency, Eq. (2.116), the better the detection efficiency and the larger the squeezing. Therefore, a relatively simple way (compared to changing the cavity from single resonance to double resonance) to increase the squeezing for our optical system is to increase the escape efficiency by increasing the OPO OC's T , which will be discussed in subsection 6.1.1.

5.3 Preliminary Evidence for Multipartite Entanglement Generation by Phase Modulation of the QOFC

The \mathbf{V} and \mathbf{U} graphs for the state generated by OPO-extrinsic PM at $\Omega_1 = 1$ and $r = 2.3$, for different values of m are presented again in figure 5.11. From figure 5.11, one can see as the m increases, more and more graph edges appear in the \mathbf{V} graph. As a reminder, from the bipartite case of the effect of a spurious graph edge in section 3.2.3, we showed that omitting the spurious graph edge is fine as long as the spurious graph edge weight is small enough, which means Eq. (3.46) holds. As the Eq. (3.46) doesn't hold, then omitting the spurious graph edge decreases the squeezing. From Eq. (3.45), one can also see that if the weight of the spurious graph edge keeps increasing, then the squeezing will keep decreasing. When the edge weight reaches $\varepsilon_{\min} = e^{-(r_1+r_2)}$, then the squeezing will disappear and we only can get vacuum noise.

With these properties of spurious graph edge in mind, let's go back to figure 5.11. When modulation index $m = 0$, suppose one performs a two-mode squeezing measurement on one of the two-mode squeezed pairs, then, ideally, one should get the same amount of squeezing generated by the OPO. As m starts to increase, spurious edges appear but with very weak weights. If the spurious graph edge weights are small enough, recall Eq. (3.46), then omitting those spurious edges wouldn't affect the amount of squeezing. But, as the spurious graph edge weights get larger and larger, the Eq. (3.46) doesn't hold, then from Eq. (3.45), we can expect the squeezing will start to decrease when omitting the spurious graph edges. Therefore, we would like to perform a two-mode squeezing measurement on one of the EPR QOFC phase-modulated by an EOM with one modulation frequency. If we can observe the two-mode squeezing decreasing as modulation index m increases, then that would be preliminary evidence indicating our theory might be right.

Figure 5.12 shows the schematic experimental setup. Laser 1 and laser 3 are phase locked, such that the two lasers have the same frequency at IR. The laser 1 IR beam passes through a doubling crystal and generates a 532 nm light as an OPO pump beam. The pump beam is in z-polarization and passes through the OPO and zzz PPKTP crystal directly. The zzz PPKTP crystal turns the 532 nm photon into two-mode squeezed pairs. The two-mode squeezed pairs pass through an EOM (Qubig PM9-NIR) with modulation frequency equal to the OPO FSR and then enter the balanced homodyne detector. The output of the balanced homodyne detector is sent to a spectrum analyzer for squeezing trace measurement. The OPO is PDH locked by laser 3, whose locking beam is injected from the unused port of PBS, hence in y-polarization, and is counter-propagating with respect to the two-mode squeezed light. By tuning the temperature of yyy PPKTP crystal, the birefringence has been compensated, so light in y-polarization and z-polarization can be resonant at the same cavity length. The laser 3 passes through two EOMs: the first EOM has modulation frequency $\Omega' = (n + \frac{1}{2}) \times \text{FSR}$ to generate strong first-order sidebands, where $n \in \mathbb{N}$. By locking the OPO and filter cavity onto the first-order sidebands, the value of n can decide which of the two-mode squeezing pairs is observed; the 2nd EOM is used for FC PDH locking purposes. The filter cavity filter out the carrier, two sidebands can pass through and act as LO for the homodyne detection.

5.3. PRELIMINARY EVIDENCE FOR MULTIPARTITE ENTANGLEMENT GENERATION BY PHASE MODULATION OF THE QOFC

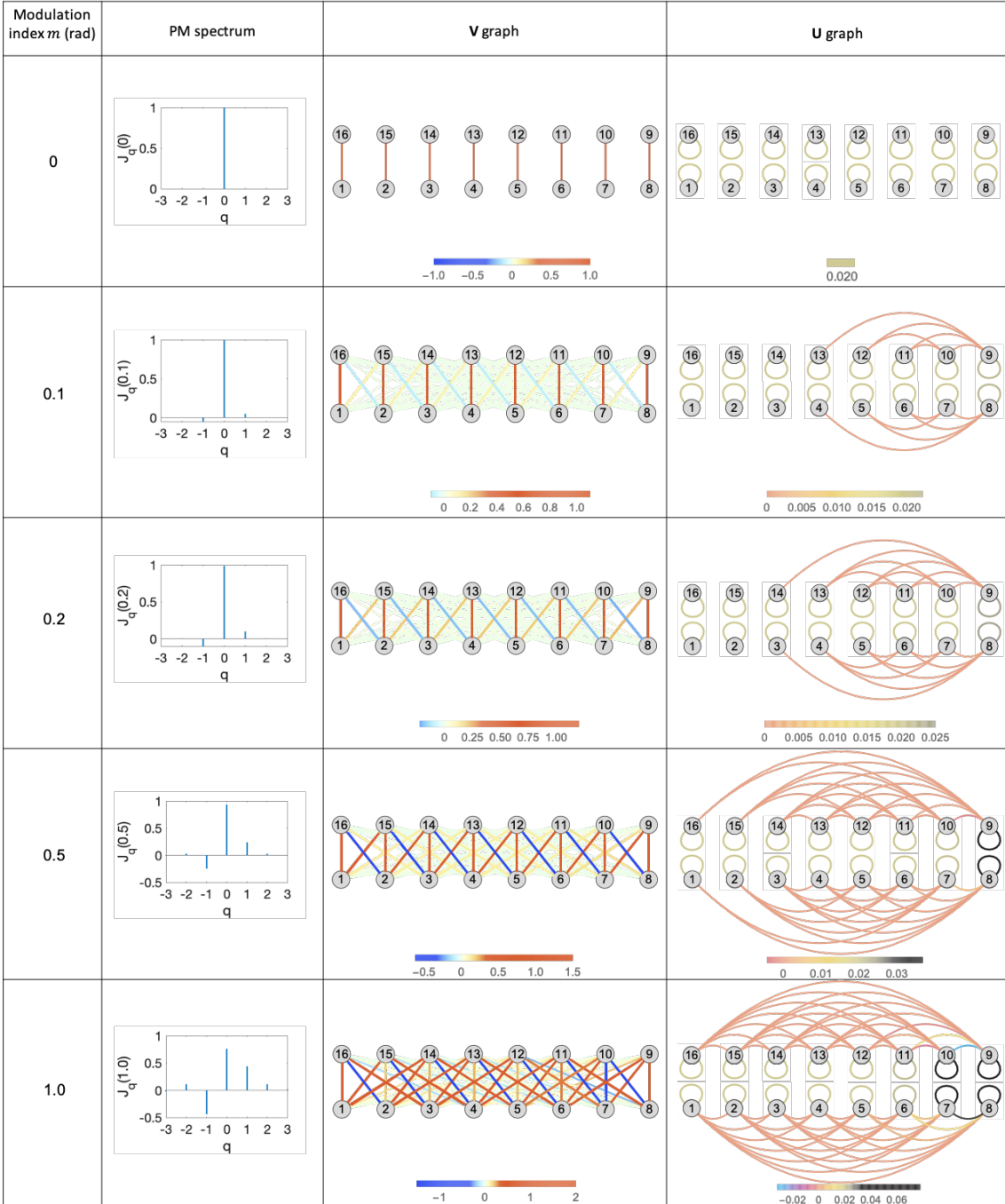


Figure 5.11: \mathbf{V} and \mathbf{U} graphs for the state generated by OPO-extrinsic PM at $\Omega_1=1$ and $r=2,3$, for different values of m . The pump frequency is equal to the sum of the frequencies of all vertical qumode pairs in the \mathbf{V} and \mathbf{U} graph columns. Note that the qumode labeled “0” in the PM spectrum column is any of the QOFC qumodes in the \mathbf{V} and \mathbf{U} graph columns.

Figure 5.13 shows the preliminary result. The modulation frequency for EOM1 is $\Omega' = 5.5$ FSR, thus it's the two-mode squeezing pairs, which have the sixth smallest frequency difference between the two modes. As the modulation index m increases, the corresponding squeezing level drops, which agrees with figure 3.6 implies: as the modulation index increase, more entanglement edges appear. We can extend the model for the bipartite case to a slightly complicated one and compare it with the

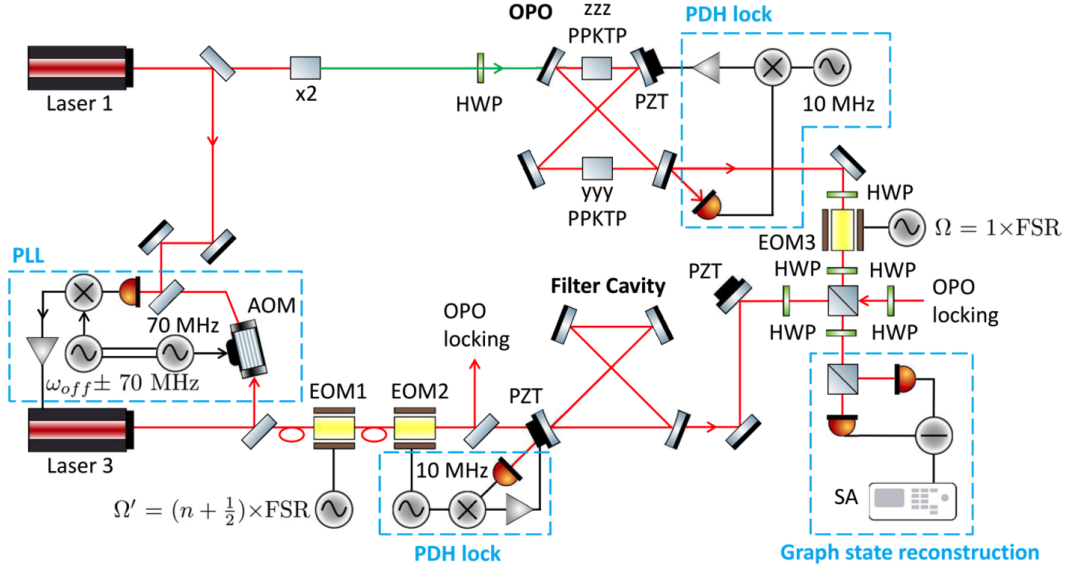


Figure 5.12: Schematic experimental setup for the preliminary experiment. PLL: phase lock loop; HWP: half-wave plate; PZT: piezoelectric transducer; AOM: acousto-optic modulator; EOM: electro-optic modulator; PDH: Pound-Drever-Hall lock loop; SA: spectrum analyzer.

result of two-mode squeezing measurement.

Considering the following canonical cluster state scenario: When $m = 0$, qumode a and qumode b are two phase-squeezed qumodes with squeezing parameter r coupled by gate $C_Z = \exp(i\varepsilon Q_a Q_b)$, thus have an edge weight ε between them, as figure (5.14a) shows. Then the observable $N_1 = P_a - Q_b$ (or $N_2 = P_b - Q_a$) has squeezed noise given by

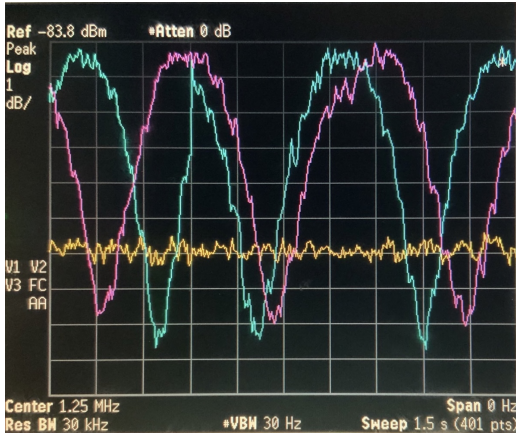
$$(\Delta N_1)^2 = \langle 00 | [(P_a - \varepsilon Q_b)e^{-r}]^2 | 00 \rangle = \frac{1}{2}e^{-2r}. \quad (5.1)$$

When modulation index $m \neq 0$, we assume there are n single-mode squeezed qumodes with the same squeezing parameter r connecting to the qumode a or qumode b by C_Z gates, so that there are also some extra edges connected to qumode a or qumode b, as figure (5.14b) shows. The number of actual extra qumodes and their edge weights are based on the theoretical result for 1-d cluster states generation. Then we perform the same measurement on qumode a and qumode b as we did in the $m = 0$ case, and thus we have

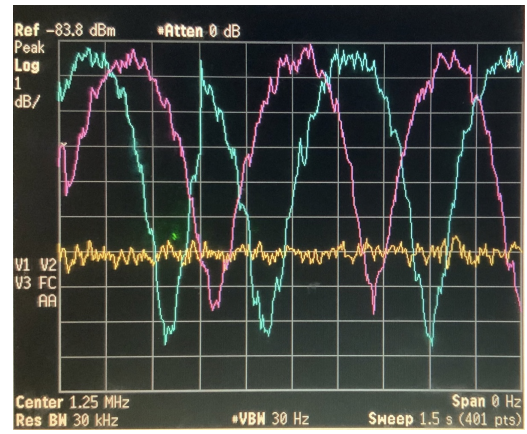
$$\begin{aligned} (\Delta N_1)^2 &= \langle 00 | \left[(P_a - \varepsilon Q_b)e^{-r} + \sum_{i=1}^n \varepsilon_i Q_i e^r \right]^2 | 00 \rangle \\ &= \frac{1}{2} \left[e^{-2r} + \left(\sum_{i=1}^n \varepsilon_i^2 \right) e^{2r} \right]. \end{aligned} \quad (5.2)$$

An accurate model would require knowing the exact number of extra edges, i.e., the size of the quantum comb. We only have an estimate of this, based on the work of former student Pei Wang [59]. Therefore, to completely verify our theoretical results, we will need to measure all the entanglement edges and fully characterize the cluster state. For this purpose, we are planning to reconstruct the covariance matrix of the cluster state, which will be discussed in a later chapter.

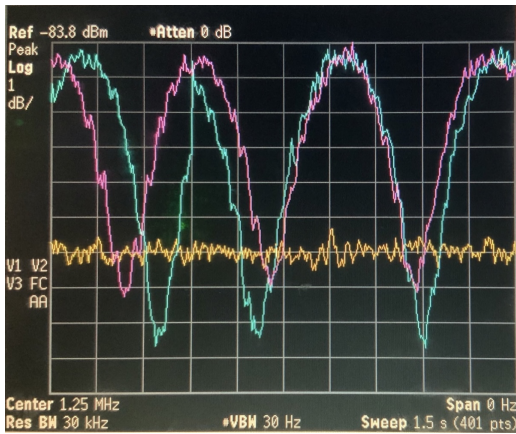
5.3. PRELIMINARY EVIDENCE FOR MULTIPARTITE ENTANGLEMENT GENERATION BY PHASE MODULATION OF THE QOFC



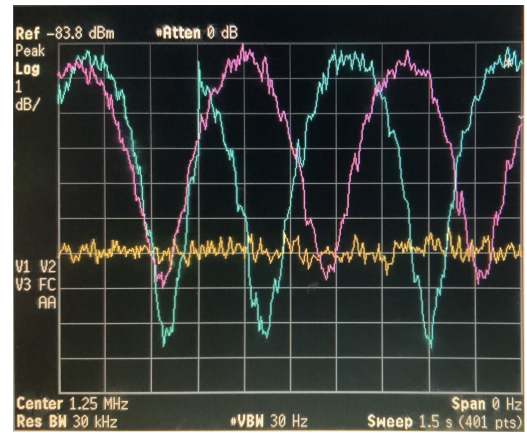
(a) $m = 0.35$ rad



(b) $m = 0.85$ rad



(c) $m = 1.25$ rad



(d) $m = 1.35$ rad

Figure 5.13: Preliminary results of two-mode squeezing with different EOM modulation index. Yellow trace: shot noise; Blue trace: two-mode squeezing with $m = 0$; Red trace: two-mode squeezing affected by modulation index m . The error bar in m is ± 0.05 rad. Note we set $\Omega' = 5.5$ FSR in figure 5.12, so we are detecting the sixth two-mode squeezing pair if we assume the most center pair is the first pair.

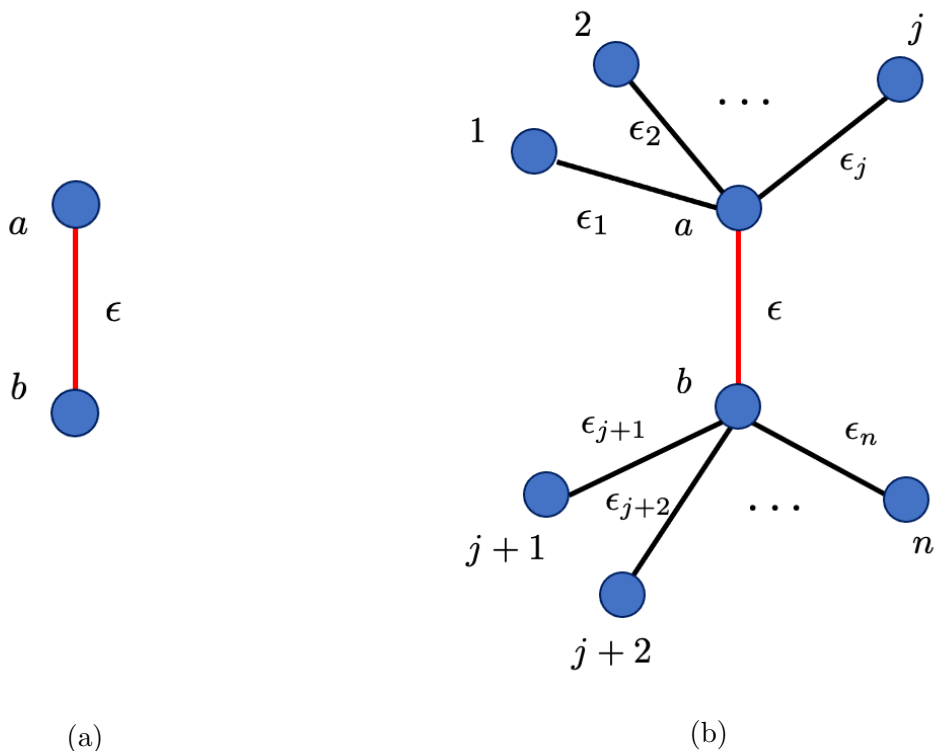


Figure 5.14: (a) two-mode squeezed canonical cluster state when $m = 0$; (b) two-mode squeezed canonical cluster state with n extra qumodes with edge weight ϵ_i , $i \in \{1, n\}$. The edge between qumode a and qumode b is in red color to emphasize the measurement is performed on qumode a and qumode b.

Chapter 6

New OPO setup

6.1 OPO Improvements

6.1.1 Squeezing Improvement and Calibration

Squeezing Improvement by Changing the OC: The level of squeezing is important for quantum computing and characterizing the cluster states. For the former, squeezing is related to determining the fault tolerance thresholds for GKP encoding [34, 44]; for the latter, squeezing determines how small the graph edges we can observe [70]. Therefore, it is desired to have squeezing as large as possible. Previously, we observed at most 3.2 dB of squeezing by an OPO with transmittance of output coupler 5% [13]. One thing we can do to increase the squeezing is to increase the escape efficiency of OPO. Recall the escape efficiency, Eq. (2.116), is defined as the following

$$\eta_{esc} = \frac{T}{T + L}, \quad (6.1)$$

where T is the cavity output coupler's transmittance and L is the round-trip loss. The round-trip loss in our system is 0.08%. Since the escape efficiency is related to the loss, we thus desire to have escape efficiency as large as possible. While decreasing the round-trip loss requires better cavity mirrors' reflectivity. It is relatively easier to increase the escape efficiency by increasing the transmittance of the OPO output coupler. But this is at the expense of larger OPO lasing threshold power, which is proportional to the T^2 . From the analytical expression for squeezing in [62], the strongest squeezing is happening when the pump power is just below the lasing threshold. Another advantage of increasing the transmittance of output coupler is the increasing of OPO linewidth, Eq. 4.15. Because the squeezing can only be observed with the cavity linewidth, this is beneficial, especially for intra-mode cluster states generation (see next section for more detail).

Hence, we changed the output coupler from 5% of transmittance to 17% of transmittance at IR, the corresponding lasing threshold thus changed from 190 mW to 2200 mW. The escape efficiency can increase from 98.4% to 99.5%, which is beneficial for obtaining high squeezing. Our 532 nm pump lasers, laser 1 and laser 2, can provide 1 W from each laser. So, our original plan was to fix laser 2, such that we can have total pump power of 2 W. But, unfortunately, we couldn't fix laser 2. Moreover, after the laser 1 pump beam passes through many optics and the EOM is installed for the pump and reference beam lock, only 630 mW can enter the OPO

cavity. With pump power 630 mW, the measured gain is 4.83 and the corresponding squeezing is 6.8 dB. With the visibility equals to 95.1%, transmission loss 4%, the quantum efficiency of PDs near 1, and phase noise 1.8° (this is due to the setup has been changed: shortening the optical path, removing the filter cavity, and using Laser 1 to lock OPO. See the next section for the modified schematic setup), the estimated observed squeezing is 5.0 dB.

Suppose we can get a new laser with high enough 532 nm power, then in principle, we can get higher squeezing when using $T = 17\%$ OC. Due to the squeezing parameter r is proportional to the strength of pump field, α , we can relate the squeezing parameter at 630 mW, r_1 , to the squeezing parameter at 2200 mW, r_2 , by $r_2 = \sqrt{17/5} \times r_1 = 1.84 \times r_1$. From Eq. (4.33), the corresponding squeezing for pump power 2200 mW, $SQ(r_2)$, is related to the squeezing for pump power 630 mW, $SQ(r_1)$, as the following:

$$\begin{aligned} SQ(r_2) &= 20 \log e^{r_2} = 20 \log e^{1.84 \times r_1} \\ &= 1.84 \times 20 \log e^{r_1} = 1.84 \times SQ(r_1) \\ &= 1.84 \times 6.85 \text{ dB} = 12.6 \text{ dB}. \end{aligned} \quad (6.2)$$

However, as we consider the escape efficiency 99.5%, visibility 95.1%, transmission loss 4%, and phase noise 1.8° (taking the quantum efficiency to be 1 for simplicity), the squeezing will drop to 7.3 dB. The squeezing drops for pump power 2200 mW (12.6 dB \rightarrow 7.3 dB) more than pump power 630 mW (6.8 dB \rightarrow 5.0 dB) is mainly due to the high squeezing is much more sensitive to the loss and phase noise, as we discussed in subsection 2.6.4. Therefore, to obtain high squeezing from a measurement, we not only need to increase the pump power, but also need to decrease the loss, increase the visibility and decrease the phase noise as much as we can.

On the other hand, suppose we can get a new OC with suitable transmission T_2 , such that the lasing threshold is close to the maximal pump power we can provide. As we know the lasing threshold is proportional to the T_2^2 , the new OC should have $T_2 = 9.1\%$. The corresponding escape efficiency is 99.1%. To estimate the amount of squeezing we can get, we need a better theory to estimate it. Here, I directly use the squeezed ($-$) and antisqueezed ($+$) quadrature variances for an OPO below threshold formula in [56]

$$V_{\pm} = 1 \pm \eta_{\text{total}} \frac{4\sqrt{P/P_{\text{thr}}}}{(1 \mp \sqrt{P/P_{\text{thr}}})^2 + (\frac{2\pi f}{\gamma})^2}, \quad (6.3)$$

where η_{total} is the total detection efficiency, Eq. (2.116), P is the pump power, P_{thr} is the lasing threshold for pump laser, and f is the sideband frequency of the measurement. γ is the cavity decay rate and $\gamma = c(T + L)/l$, with the speed of light c , the cavity round-trip length l , the OPO output coupler's power transmissivity T , and the round-trip loss L . In the estimation, I use $P/P_{\text{thr}} = 0.99$ (right below lasing threshold), $\eta_{\text{total}} = \eta_{\text{esc}}$, f is 1.22 MHz (so that in $T = 5\%$ case, the estimated squeezing is 3.2 dB), and $L = 0.08\%$ for the round-trip loss, the estimated squeezing for $T_2=9.1\%$ without phase noise and any other loss is 5.8 dB. However, as we consider the visibility 95.1%, transmission loss 4%, and phase noise 1.8° , the squeezing will drop to 4.4 dB.

Squeezing Calibration: The squeezing trace obtained by the spectrum analyzer is shown in figure 6.1a, and the observed squeezing is about 4.7 dB on average.

The observed squeezing is lower than the expected squeezing, 5 dB. This is due to the fact that the measured squeezing and measured shot noise are actually containing the electronic noise (also known as dark noise) inside, as figure 6.1b shows, so we need to perform calibration to find out the actual squeezing.

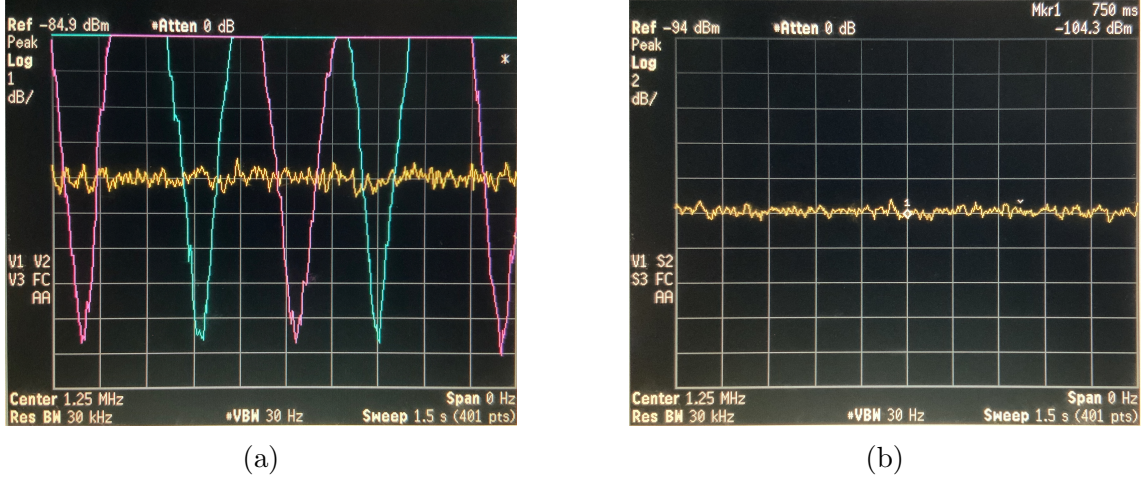


Figure 6.1: Squeezing trace after changing the output coupler mirror from 5% of transmittance to 17% of transmittance. (a) squeezing trace. Shot noise (yellow trace).; (b) electronic noise. The setting is center frequency 1.25 MHz, zero spans, resolution bandwidth 30 kHz, video bandwidth 30 Hz, and sweep time 1.5 seconds.

The dark noise contaminated squeezing obtained from the experiment is

$$S_{\text{exp}} = 10 \log_{10} \left(\frac{V_{\text{sq}} + V_{\text{dn}}}{V_{\text{sn}} + V_{\text{dn}}} \right), \quad (6.4)$$

while the actual squeezing level is

$$S_{\text{act}} = 10 \log_{10} \left(\frac{V_{\text{sq}}}{V_{\text{sn}}} \right), \quad (6.5)$$

where V_{sq} is the variance of the squeezing, V_{sn} is the variance of the shot noise, and V_{dn} is variance of dark noise. (As a reminder, the spectrum analyzer measures the power spectrum, i.e. the variance of noise.) We then can obtain an equation connecting the S_{exp} and S_{act} as

$$S_{\text{act}} = 10 \log_{10} \left[\left(10^{\frac{S_{\text{exp}}}{10}} - 1 \right) \frac{10^{\frac{S_{\text{dn}}}{10}}}{10^{\frac{S_{\text{sn}}}{10}}} + 10^{\frac{S_{\text{exp}}}{10}} \right], \quad (6.6)$$

where $S_{\text{dn}} = 10 \log_{10} V_{\text{dn}}$ and $S_{\text{sn}} = 10 \log_{10} V_{\text{sn}}$ which converting the variance of noises to dB unit. Figure 6.2 shows the relation between the squeezing obtained from experiment and the actual squeezing. Hence, in our case, with observed squeezing 4.7 dB, the actual squeezing is 5.0 dB, which is the same as what we predicted above.

6.1.2 The Anomalous OPO Reflected Mode

While checking the OPO beam profile by beam profiler (Newport LBP2-HR-VIS3, 190-1100 nm Silicon CCD, 1624 × 1224 Pixels), we noticed the OPO reflected beam

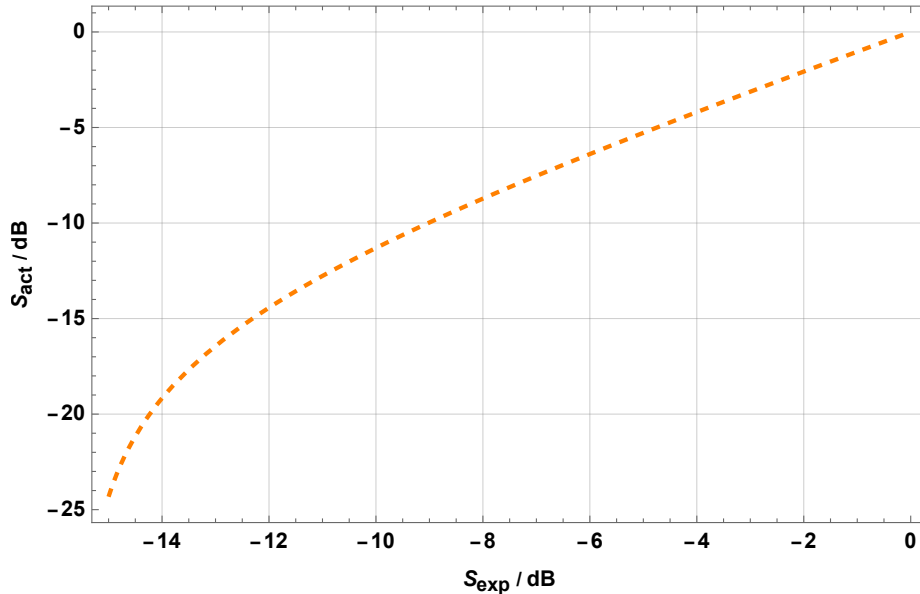


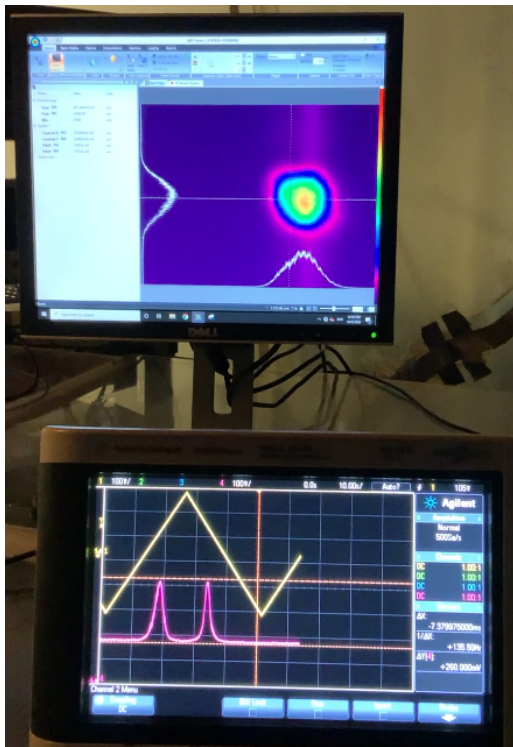
Figure 6.2: Calibration of the squeezing obtained experimentally from the actual squeezing. The horizontal axis is the observed squeezing from 0 dB to 15 dB and the vertical axis is the squeezing after calibration. Note the negative sign represents squeezing.

from the output coupler, which is a combination of partially reflected input beam and the OPO output beam (the input beam partially entered to the OPO and then came out), looks quite anomalous when OPO was near- and on-resonance. Figure 6.3 shows the reflected beam profiles at four different conditions, and one can see how the profile changes (the recorded video can be watched on Youtube by clicking here).

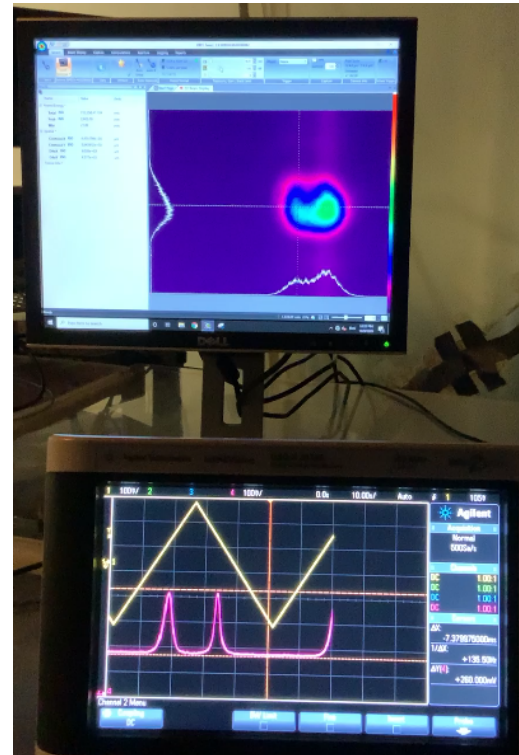
This phenomenon is confusing to us because for a good mode matched beam injected to a cavity ($> 90\%$ mode matched), we expect the injected beam inside the OPO is very similar to the OPO eigenmode. Therefore, the reflected beam should be very close to the OPO transmitted mode as well and the reflected mode shouldn't change when OPO is near- and on-resonance. We thus want to understand what causes such anomalous reflected beam and can we regard the reflected beam as the OPO output mode. Knowing how to obtain the OPO output mode is important for us to estimate the visibility between quantum light and LO. The quantum light is quite weak, and we have to use another coherent light that has the same wavefront, waist, polarization, and propagating direction as quantum light, to mimic the quantum light and couple to the LO before entering the balanced homodyne detector. Due to the OPO reflected beam being stronger, mW , than OPO transmitted beam, μW , it is tempting and easier to use the OPO reflected beam to mode match to LO than use OPO transmitted beam.

Figure 6.4 shows the schematic setup of observing the anomalous OPO reflected beam profile by a beam profiler while monitoring the second harmonic generation (SHG) by a power meter. The SHG monitor is used to tell when the OPO is on resonance. The laser used here is laser 1. Few things we can see from figure 6.3 and video. First of all, the profile changes when OPO is off-, near- and on-resonance. Secondly, the near-resonance profiles are not the same. As a reminder, the reflected beam profile is actually an interference by the directly reflected beam from the

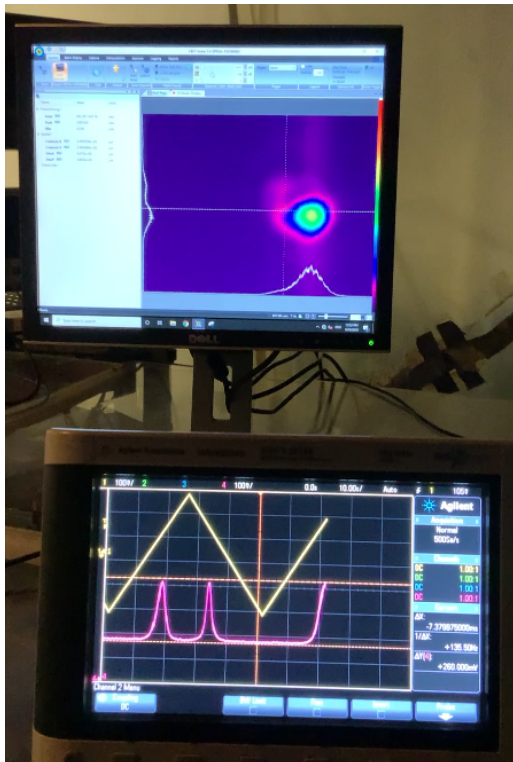
6.1. OPO IMPROVEMENTS



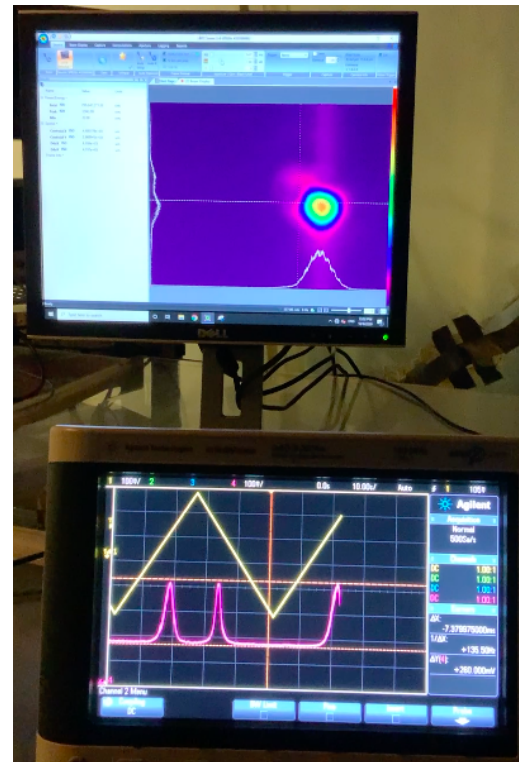
(a) Off-resonance beam profile.



(b) Near-resonance beam profile (left).



(c) On-resonance beam profile.



(d) Near-resonance beam profile (right).

Figure 6.3: Reflected beam profiles at four different resonance conditions, which are shown on the screen in the pictures. The oscilloscope monitors the SHG powers (red trace) and ramp signal for driving the OPO PZT (yellow trace).

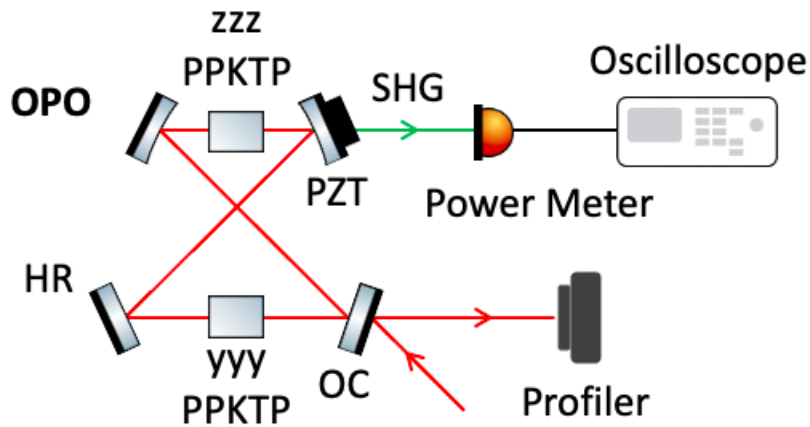


Figure 6.4: Schematic experimental setup for observing the anomalous OPO reflected beam profile while scanning the cavity length by a ramp signal. SHG: second-harmonic generation of the injected IR beam (as denoted by green beam); OC: output coupler; HR: high reflection mirror.

output coupler and the output beam from the OPO. Therefore, the profile change might be due to incomplete interference. This phenomenon doesn't exist for the filter cavity's reflected beam or the OPO's transmitted beam (when input beam was injected from HR mirror, as figure 6.5 shows: the beam profiles remain the same no matter whether the cavity is off-, near- or on-resonance. It's not entirely clear what physics causes this anomalous OPO reflected profile, but one thing suspicious is the OPO nonlinear medium, i.e. nonlinear effect, such as, for example, a self-focusing effect from the third-order nonlinearity. If so, lowering the incident beam power in figure 6.4 should dramatically change the effect. But, unfortunately, we tried different incident power from 12 mW down to 12 μ W, the strangeness of the OPO reflected beam still exists.

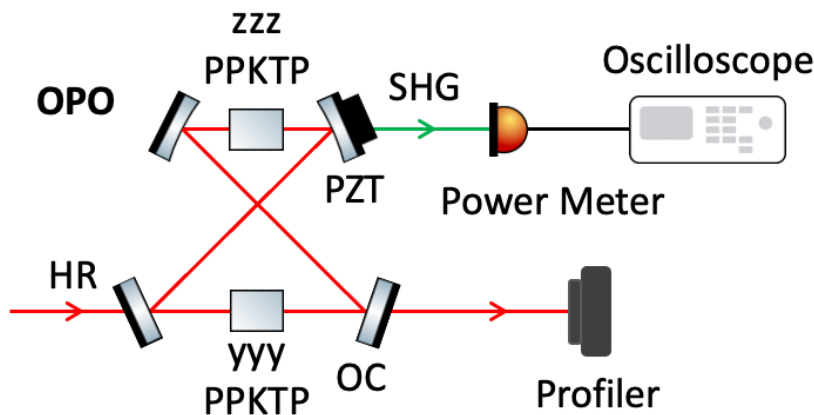


Figure 6.5: Schematic experimental setup for observing the OPO transmitted beam profile while scanning the cavity length by a ramp signal. SHG: second-harmonic generation of the injected IR beam (as denoted by green beam); OC: output coupler; HR: high reflection mirror.

Hence, based on the above discussion, we believe the OPO output mode can not be obtained by injecting the input beam from OC of the OPO, as figure 6.4 shows. To obtain the OPO output mode, we have to use the OPO transmitted beam injected from HR, as figure 6.5 shows. Then, we can use such transmitted OPO mode, which mimics the quantum light, to mode match it to the LO.

6.1.3 Using reference beam as Local Oscillator

Figure 6.6 shows the schematic setup of using the reference beam as the LO. The advantage of this method is because the reference beam is transmitted through the OPO cavity, it must have the same mode as the mode of quantum light. Due to the reference beam is propagating collinearly with the quantum light, the mode matching between the reference beam and quantum light should be perfect, and the visibility would be as good as 100%. But we can't measure the visibility to confirm it because the quantum light is too weak to detect by a photodetector.

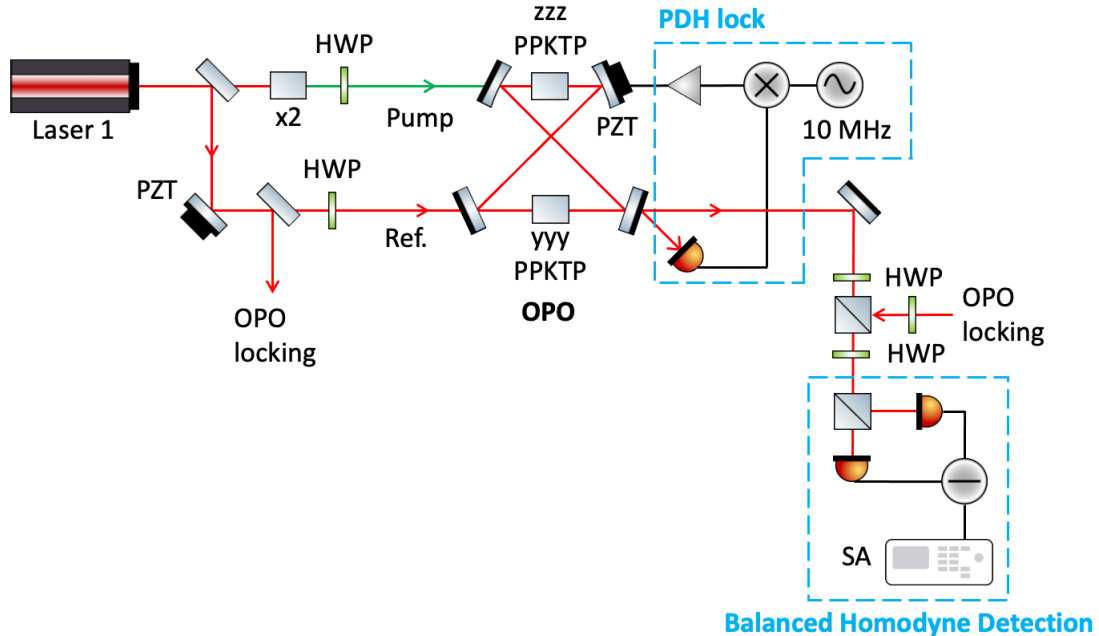


Figure 6.6: Schematic experimental setup for using the reference beam as the LO to observe the squeezing. Note the OPO locking beam and reference beam are coming from laser 1. Ref.: reference beam.

There are a few disadvantages of using a reference beam as LO.

- 1. weak OPO transmitted reference beam.** As we discussed before, the reference beam is injected from the HR mirror side of OPO, so with the incident reference beam 20 mW, we only can get 20 μ W. Therefore, we need a balanced homodyne detector that can measure 20 μ W and still have good SNR. See the next subsection for the balanced homodyne detector sensitivity improvement work.
- 2. balanced homodyne detector not balancing.** One of the reasons that we like to use a balanced homodyne detector, from subsection 2.6.3, is it can remove the DC term. But this statement is only true when the two fields, LO and quantum light, are coming from two adjacency sides of the beam splitter, such that the interference

terms in the photon number representation of two output fields have π phase shift. However, as the LO and quantum light enters from the same beam splitter port, the interference terms in the two output fields' photon number representation don't have π phase shift. Therefore, the "balancing" kills all the signals.

3. wrong relative phases between reference beam, quantum light, and pump beam. To observe the phase quadrature squeezing, the required phase between the reference beam and the quantum light is

$$\phi_{\text{ref}} - \phi_{\text{q}} = \frac{\pi}{2}, \quad (6.7)$$

where ϕ_{ref} is the phase of reference beam and ϕ_{q} is the phase of quantum light. We can only introduce this phase difference to the reference beam before it enters the OPO or the pump beam. As we discussed in section 6.2.2.a, the pump determines the phase of quantum light, and their phase relation is

$$\phi_p - 2\phi_q = 0, \quad (6.8)$$

By rewriting the Eq. (6.7), we can obtain the phase relation between pump and reference beam from Eq. (6.8) as

$$\begin{aligned} \phi_p - 2\phi_q &= 0 \\ \Rightarrow \phi_p - 2\phi_{\text{ref}} + \pi &= 0 \\ \Rightarrow \phi_p - 2\phi_{\text{ref}} &= -\pi, \end{aligned} \quad (6.9)$$

which implies a parametric deamplification for the reference beam. In the experiment, this deamplification on the reference beam depletes the reference beam power, which is under the sensitivity limit of OPA818 based balanced homodyne detector.

Therefore, due to the above three reasons, we have to use other approaches to observe squeezing.

6.1.4 Balanced Homodyne Detector Sensitivity Improvement

As discussed in the previous section, when we tried to use the reference beam as the LO, the usable power dropped and the signal to noise ratio (SNR) also dropped. The SNR is also called shot-to-electronic noise clearance or clearance [32], and is defined as the ratio of the shot noise (measured in the presence of LO) and the electronic noise of BHD (measured with the LO blocked). Figure 6.7 shows the spectra of balanced homodyne detector signal at two different LO powers. The SNR dropped from 16 dB for 2 mW LO power to 2 dB for 20 μ W. Due to the reference beam being injected from the HR mirror side, and the laser we used already reaching its maximal output power, therefore, we can't further increase the power of the reference beam anymore. With an SNR of 2 dB, this is not enough for us to detect 3 dB of squeezing. Hence, we need to increase the SNR of BHD by decreasing the (dark) noise from the detector. Note one may notice the signal from a single PD starts to fall below the shot noise after 5.5 MHz in figure 6.7a and 2 MHz in figure 6.7b, which seems counterintuitive. This is because when there is uncorrelated noise in the two PDs' signals, the subtraction in the balanced homodyne detector can not remove but actually add the noise up. Therefore, the shot noise signal is larger than the single PD signal.

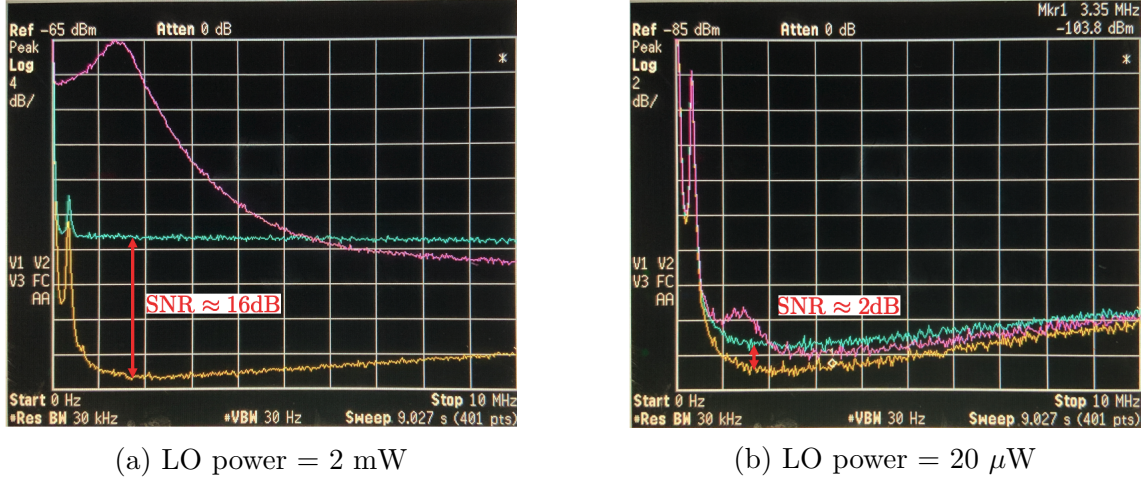


Figure 6.7: Spectra of balanced homodyne detector signal at (a) 2 mW and (b) 20 μ W. The SNR, the difference between shot noise and dark noise, dropped from 16 dB (a) to 2 dB (b). Yellow trace: dark noise; Blue trace: shot noise; Red trace: single PD signal.

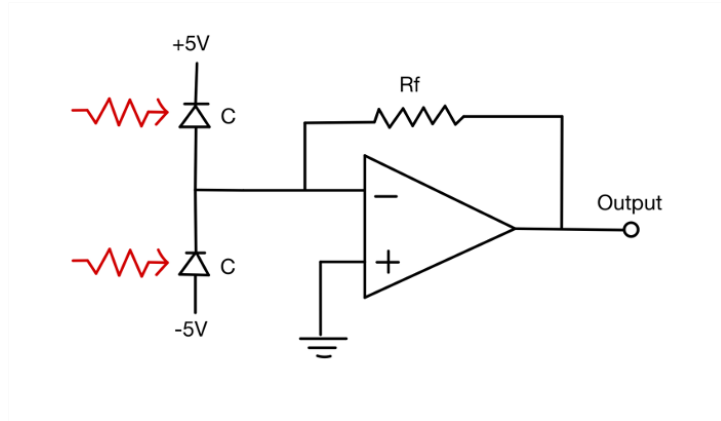


Figure 6.8: Transimpedance amplifier converts the photo-current difference into voltage. C: capacitance of PD; R_f: feedback resistance.

For the balanced homodyne detector, we use a transimpedance amplifier to convert the photo-current difference into voltage, as figure 6.8 shows. The op-amp we used is the OPA686. We can use the model in the OPA686's manual to estimate the SNR for the BHD. Specifically, for the electronic noise part

$$i_{eq}^2 = i_n^2 + \frac{e_n^2}{R_f^2} + \frac{4k_B T}{R_f} + \frac{(e_n 2\pi 2Cf)^2}{3} + 2qI_d, \quad (6.10)$$

where i_{eq} is equivalent input noise current if the output current is band-limited to $F < \frac{1}{2\pi R_f C}$, F is the bandlimiting frequency in Hz, i_n is the input current noise for the op-amp inverting input, e_n is the input voltage noise for the op-amp, R_f is the feedback resistance, C is the PD capacitance, f is frequency in unit of Hz, q is the elementary electric charge, and I_d is the dark current. The i_{eq} is in the unit of A²/Hz. For the signal part, which is the shot noise, the model is

$$i_{shot}^2 = 2qRP, \quad (6.11)$$

where R is the responsivity of PD with a unit of A/W and P is the optical power of LO. The responsivity is related to quantum efficiency η as follows

$$\eta = R \frac{1.24}{\lambda}, \quad (6.12)$$

where λ is the wavelength of incident field and is in units of μm . Same as the i_{eq}^2 , i_{shot}^2 is in the unit of A^2/Hz . The SNR in decibel can be defined as

$$\text{SNR} = 10 \log_{10} \left(\frac{i_{shot}}{i_{eq}} \right)^2. \quad (6.13)$$

With this model in hand, we now can tune parameters and hunt for an op-amp with smaller i_n or e_n . Qualitatively speaking, for the electronic noise, the input current noise i_n dominates at low frequency and the input voltage noise e_n dominates at high frequency. A way to reduce i_n is using a MOSFET op-amp and we found an op-amp, OPA818, that provides smaller current noise and enough bandwidth. The voltage noise is also related to the capacitance: the smaller the capacitance, the smaller the voltage noise. We thus also changed the photodiodes with smaller sensing areas and smaller capacitance. The former photodiodes we used are high quantum efficiency InGaAs photodiodes (quantum efficiency $> 99\%$ at 1064 nm) with a sensing area of 0.5 mm diameter. Later, we changed the photodiodes to Fermionics InGaAs PIN photodiodes (quantum efficiency $> 99\%$ at 1064 nm) with a sensing area of 0.15 mm diameter. Figure 6.9 shows the model results of SNR by using OPA686 and OPA818, and the corresponding parameters used can be found in table 6.1.

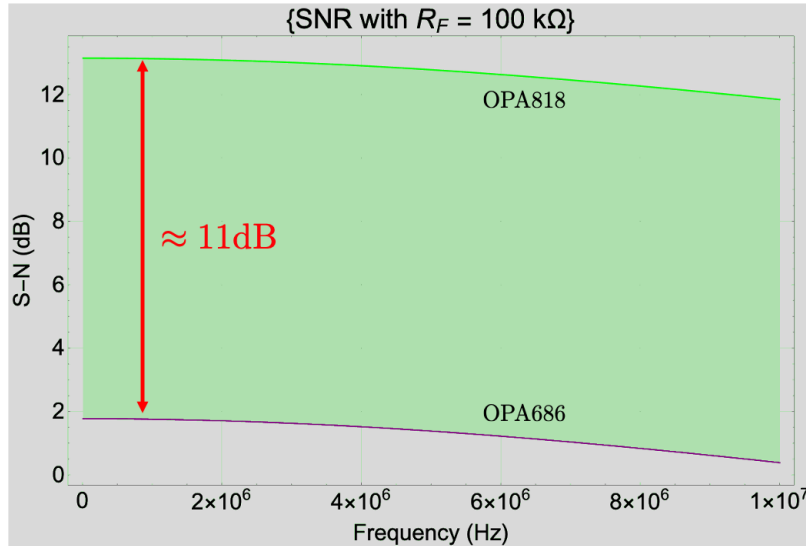


Figure 6.9: Model results: SNR by using OPA686 (purple line) and OPA818 (green line) with feedback resistance 100 k Ω . Other parameters and noise values can be found in table 6.1. The OPA818 with proper settings can provide higher SNR than OPA686 by 11 dB around.

We modified the OPA818 demo board (from Texas Instruments) based on the parameters used in the model, as figure 6.10a shows. The new BHD's spectra of signal with 15 μW LO power is also shown in figure 6.10b. One can see the new

	P	i_n	e_n	C
OPA686	$20 \mu\text{W}$	$1.8 \text{ pA}/\sqrt{\text{Hz}}$	$1.3 \text{ nV}/\sqrt{\text{Hz}}$	12 pF
OPA818	$15 \mu\text{W}$	$0.145 \text{ pA}/\sqrt{\text{Hz}}$	$2.2 \text{ nV}/\sqrt{\text{Hz}}$	1.6 pF

Table 6.1: Noises of op-amps and parameters used in the model.

BHD has 10 dB SNR, which is higher than the SNR from the OPA686 based BHD (figure 6.7b). However, this is limited to frequencies 2 MHz and there is some discrepancy between the model result and the measurement result. The discrepancy may be due to the fact that the model is quite simple, and there are some residual inductance and capacitance in the circuit.

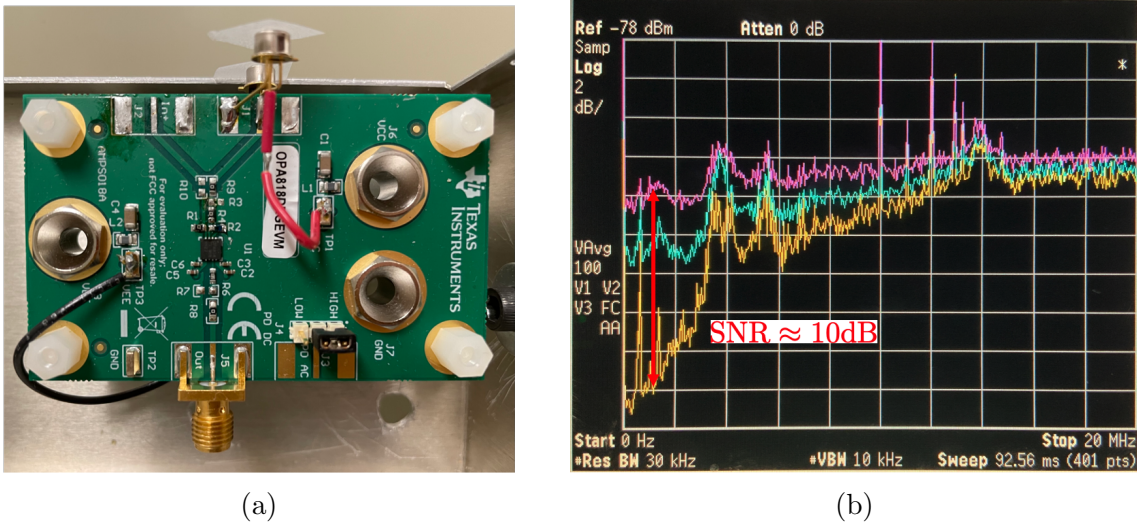


Figure 6.10: New BHD circuit and its performance. (a) the new BHD is modified from the OPA818 demo board. (b) the spectra of signal with $15 \mu\text{W}$ LO power. Yellow trace: dark noise; blue trace: single PD signal; Red trace: shot noise.

6.1.5 Lifting the Bandwidth of a Balanced Homodyne Detector

In the previous subsection, we were trying to increase the SNR of a balanced homodyne detector by lowering the electronic noise, due to the power of reference beam can't be further increased to more than $20 \mu\text{W}$. Note the reference beam is injected from the HR mirror of the OPO. However, in the normal case, the power of LO is about 2 mW and its power can be easily increased, because the LO doesn't pass any cavity. In this case, the LO is combined with the quantum light by a BS (or polarizing BS) before entering a balanced homodyne detector, and we can increase the SNR of a balanced homodyne detector by increasing the power of LO. From Eq. (6.11) in the previous subsection, we know the shot noise is proportional to the optical power of LO. Therefore, suppose we can increase the power of LO by 4 times from 2 mW to 8 mW, then the SNR should be increased by 6 dB. The bandwidth of the OPA686 based balanced homodyne detector is shown in figure 6.11 with 2 mW

and 8 mW LO power. One can see, within 33 MHz, the shot noise increased by 6 dB as expected. As frequency goes higher, the increased SNR becomes smaller and smaller, which might be caused by the bandwidth of electronics. Another benefit of increasing the LO power is the bandwidth of the balanced homodyne detector is also increased: the bandwidth with $\text{SNR} > 3$ dB is increased from 50 MHz for 2 mW LO to 95 MHz for 8 mW LO. Therefore, it is usually desired to have the optical power of LO as large as possible. The increased detector bandwidth is beneficial for the covariance matrix reconstruction by heterodyne measurement, which will require a detector with bandwidth about 70 MHz (half of OPO linewidth, 20 MHz, plus the frequency difference between LO and center of target comb line, 50 MHz). The detail of covariance matrix reconstruction will be discussed in section 6.2.

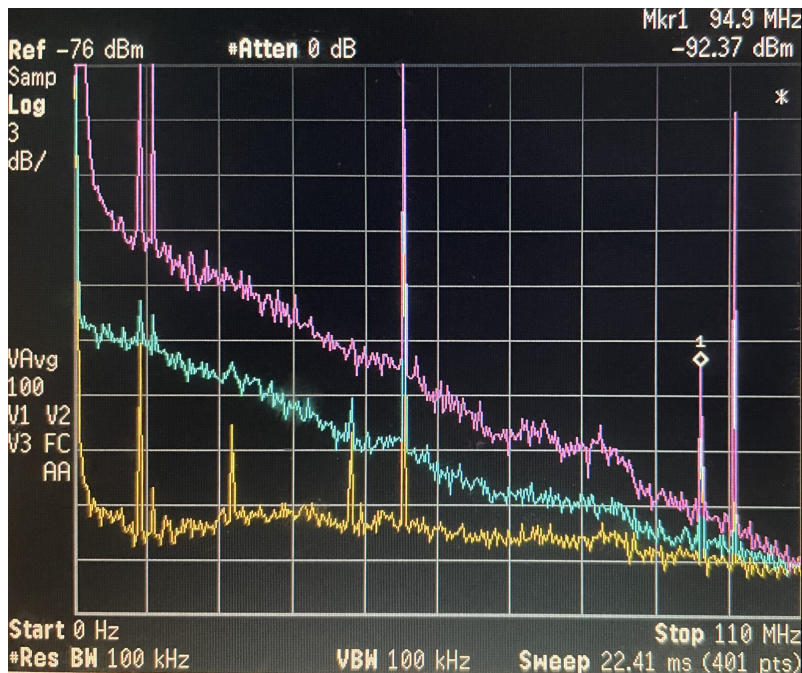


Figure 6.11: The bandwidth of the OPA686 based balanced homodyne detector. Yellow trace: dark noise; Blue trace: shot noise with the power of LO 2 mW; Red trace: shot noise with the power of LO 8 mW. The bandwidth with $\text{SNR} > 3$ dB is increased from 50 MHz (blue trace) to 95 MHz (red trace).

6.2 Covariance Matrix Measurement Setup

6.2.1 Measurement Principle and Plan

From inter-mode cluster states to intra-mode cluster states: In chapter 3, we introduced a simple method to generate cluster states by phase-modulated QOFC, which requires the EOM modulation frequency to be an integer of OPO FSR. This is what we called inter-mode cluster states generation: generating cluster states by entangling comb lines. However, considering the linewidth of each comb line is actually a 40 MHz continuous distribution in the frequency domain, with the half frequency of pump is aligned with one comb line, as figure 6.12a shows, we can apply our phase-modulation method to entangle the modes, which are called

intra-modes, within this comb line, as figure 6.12. Since the comb line distribution is continuous, we can define the modulation frequency at will in principle, but due to the linewidth of the LO laser being about 1 kHz, we need to set the EOM modulation frequency to at least 10 kHz. In this way, we can have at most 4000 qumodes to build the cluster states.

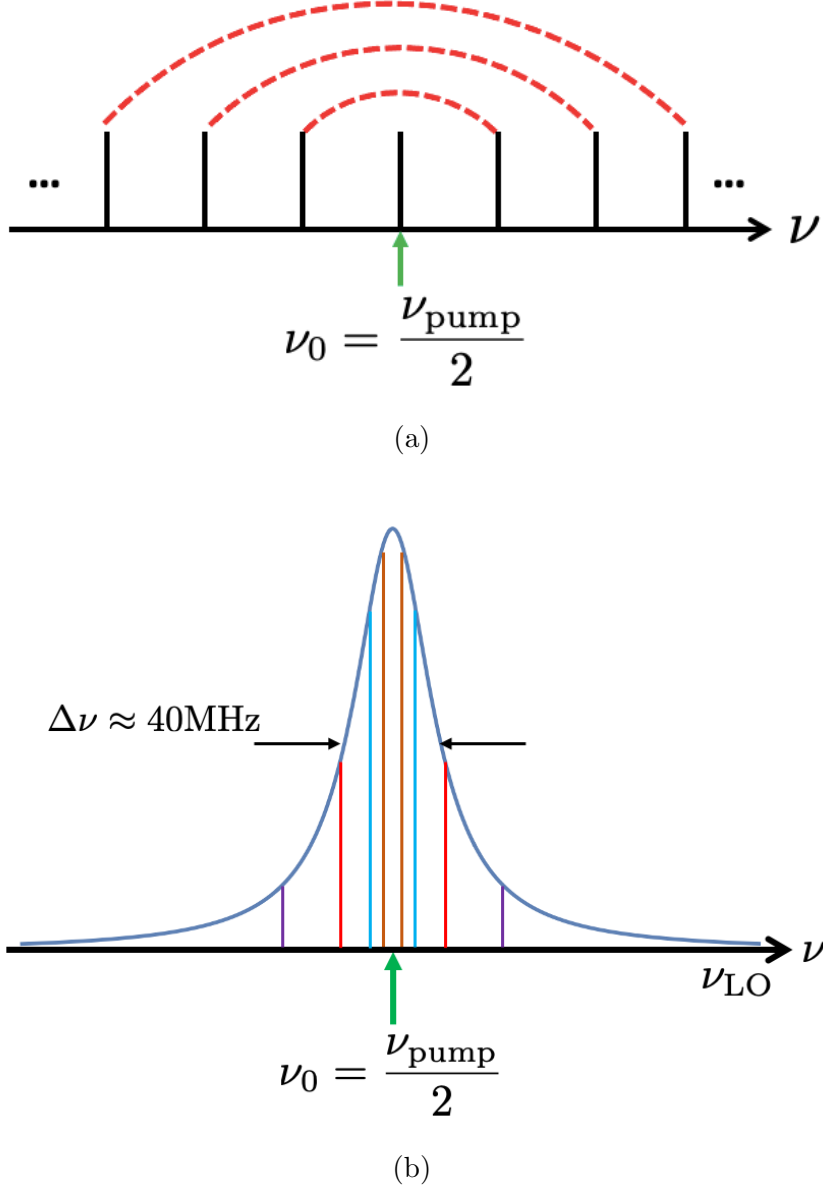


Figure 6.12: The idea of intra-modes in QOFC. (a) The half frequency of the pump (green arrow) is set to align with one of the QOFC combs. (b) The half frequency of pump aligned QOFC comb line zoomed-in, which is a Lorentzian lineshape with FWHM about 40 MHz. The comb line is composed of continuous two-mode squeezed pairs, which only showed 4 pairs with 4 different colors for simplicity.

Cluster states verification via heterodyne measurement: In the two-mode squeezed state case, we can verify the two-mode squeezed state by performing a squeezing measurement. We can set the frequency of LO to half of the frequency sum of the two modes or use two LOs with their frequencies the same as the frequencies of

two modes, and then measure the beat note to observe the squeezing. The squeezing implies there is an entanglement between the two modes. But this type of verification becomes harder to perform if there are entangled edges between other two-mode squeezed pairs, such as the preliminary result shown in section 5.3. Therefore, we need another type of measurement scheme to fully characterize all the entanglements in cluster states. One way to achieve this goal is to reconstruct the covariance matrix, Eq. 3.32, of the state. Practically, instead of setting the LO to the center of the target comb line, we will shift the frequency of LO by 50 MHz, then measure the beat note between LO and target comb line by a balanced heterodyne detector. To illustrate the idea, let's consider the case of reconstructing the two-mode covariance matrix, Eq 3.33, which is

$$\Sigma_x = \left\langle \left(\begin{array}{cccc} Q_1^2 & Q_1 Q_2 & \frac{1}{2}(Q_1 P_1 + P_1 Q_1) & Q_1 P_2 \\ Q_2 Q_1 & Q_2^2 & Q_2 P_1 & \frac{1}{2}(Q_2 P_2 + P_2 Q_2) \\ \frac{1}{2}(P_1 Q_1 + Q_1 P_1) & P_1 Q_2 & P_1^2 & P_1 P_2 \\ P_2 Q_1 & \frac{1}{2}(P_2 Q_2 + Q_2 P_2) & P_2 P_1 & P_2^2 \end{array} \right) \right\rangle. \quad (6.14)$$

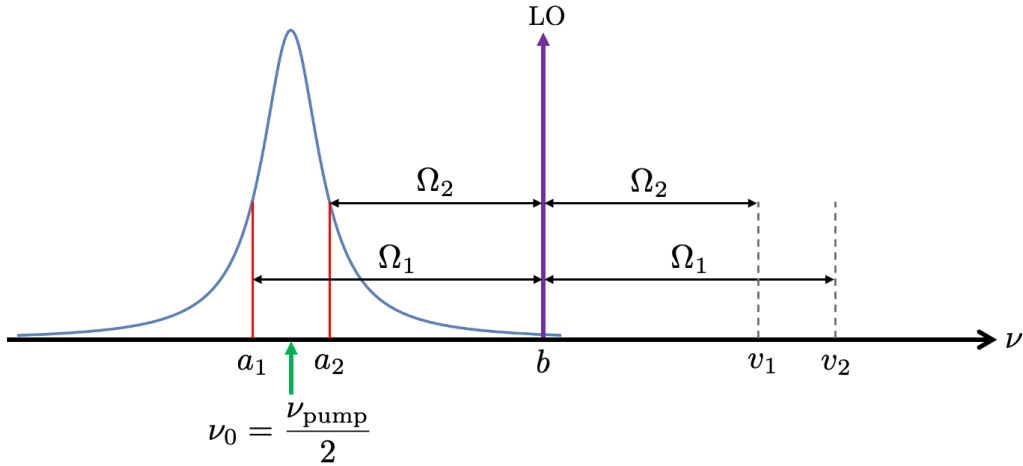


Figure 6.13: The idea of two-mode covariance matrix reconstruction from a balanced heterodyne measurement. a_i is the operator of mode i , b is the operator of LO, v_i is the operator for vacuum mode i , Ω_i is the frequencies difference between a_i (and v_i) and LO, and $i \in \{1, 2\}$

Figure 6.13 represents the idea of two-mode covariance reconstruction from a balanced heterodyne measurement. The photocurrent difference is

$$N_- = b^\dagger(a_1 + a_2 + v_1 + v_2) + (a_1^\dagger + a_2^\dagger + v_1^\dagger + v_2^\dagger)b. \quad (6.15)$$

Because the LO is a classical field and it's a frequency reference, we take $b \rightarrow |\beta|e^{i\theta}$. Here θ is the relative phase between LO and target fields, which are two quantum fields and two vacuum fields in current scenario. The other four operators become

$$\begin{aligned} a_1 &\rightarrow a_1 e^{i\Omega_1 t} \\ a_2 &\rightarrow a_2 e^{i\Omega_2 t} \\ v_1 &\rightarrow v_1 e^{i\Omega_1 t} \\ v_2 &\rightarrow v_2 e^{i\Omega_2 t}. \end{aligned} \quad (6.16)$$

The photocurrent difference thus become

$$\begin{aligned}
 N_- &= |\beta| \left[(a_1 e^{i\Omega_1 t} + a_2 e^{i\Omega_2 t} + v_1 e^{i\Omega_1 t} + v_2 e^{i\Omega_2 t}) e^{-i\theta} \right. \\
 &\quad \left. + (a_1^\dagger e^{i\Omega_1 t} + a_2^\dagger e^{i\Omega_2 t} + v_1^\dagger e^{i\Omega_1 t} + v_2^\dagger e^{i\Omega_2 t}) e^{i\theta} \right] \\
 &= \sqrt{2} |\beta| \left\{ \cos(\Omega_1 t) [\cos \theta (Q_1 + Q_{v_1}) - \sin \theta (P_1 + P_{v_1})] \right. \\
 &\quad + \sin(\Omega_1 t) [\cos \theta (-P_1 + P_{v_1}) + \sin \theta (-Q_1 + Q_{v_1})] \\
 &\quad + \cos(\Omega_2 t) [\cos \theta (Q_2 + Q_{v_2}) - \sin \theta (P_2 + P_{v_2})] \\
 &\quad \left. + \sin(\Omega_2 t) [\cos \theta (-P_2 + P_{v_2}) + \sin \theta (-Q_2 + Q_{v_2})] \right\}. \tag{6.17}
 \end{aligned}$$

Eq. 6.17 indicates the heterodyne measurement gives Q_i and P_i with $i \in \{1, 2\}$ together with vacuum quadratures at two different beat note frequencies. Hence, we can separate those two beat note frequencies by a fast Fourier transform (FFT) of the photocurrent difference N_- . If the relative phase between LO and interested modes is stable, then a FFT yields cosine and sine demodulated quadratures, for example, $[\cos \theta (Q_1 + Q_{v_1}) - \sin \theta (P_1 + P_{v_1})]$ and $[\cos \theta (-P_1 + P_{v_1}) + \sin \theta (-Q_1 + Q_{v_1})]$ for Ω_1 frequency. This is exactly the same as a demodulated signal at the different beat note frequencies by using RF local oscillators. Therefore, it is very important to know the value of phase of LO, θ , and make sure it doesn't change while recording the photocurrent difference. Here I set the $\theta = 0$ for the reason of showing how we can obtain the two-mode covariance matrix, but the θ can be any value for the covariance matrix reconstruction, as long as it is stable. The photocurrent difference with $\theta = 0$ is:

$$\begin{aligned}
 N_- &= \sqrt{2} |\beta| \left[\underbrace{\cos(\Omega_1 t) (Q_1 + Q_{v_1})}_{\text{term 1}} + \underbrace{\sin(\Omega_1 t) (-P_1 + P_{v_1})}_{\text{term 2}} \right. \\
 &\quad \left. + \underbrace{\cos(\Omega_2 t) (Q_2 + Q_{v_2})}_{\text{term 3}} + \underbrace{\sin(\Omega_2 t) (-P_2 + P_{v_2})}_{\text{term 4}} \right]. \tag{6.18}
 \end{aligned}$$

We then can reconstruct the covariance matrix from the four terms indicated in Eq. (6.18), by taking the averaged product of two terms. For example, we can take the averaged product of term 1 and term 3 to obtain the matrix elements $Q_1 Q_2$ follows

$$\begin{aligned}
 &\langle (Q_1 + Q_{v_1})(Q_2 + Q_{v_2}) \rangle \\
 &= \langle Q_1 Q_2 + Q_1 Q_{v_2} + Q_{v_1} Q_2 + Q_{v_1} Q_{v_2} \rangle \\
 &= \langle Q_1 Q_2 \rangle, \tag{6.19}
 \end{aligned}$$

which we used the average of vacuum quadratures are zero $\langle Q_{v_1} \rangle = \langle Q_{v_2} \rangle = 0$. The generalized and detailed calculations will be included in Xuan Zhu's Ph.D. thesis.

Because we plan to record the data for a certain amount of time, chop the data into smaller time windows, then perform FFT and average to reconstruct the covariance matrix, we need to make sure the relative phase between LO and target lights is stable. Therefore, we inject a reference beam to the OPO via the HR mirror side, for the purpose of (1) providing a frequency reference for two phase lock loops; (2) finding out the phase change due to the reference beam and quantum light are in the same path and in the same polarisation. The frequency of the reference beam is set to be the same as the half frequency of the pump. Figure 6.14 represents the

LO and reference beam with respect to the interested comb line in the frequency domain. The detail of the phase lock between those three fields will be discussed later.

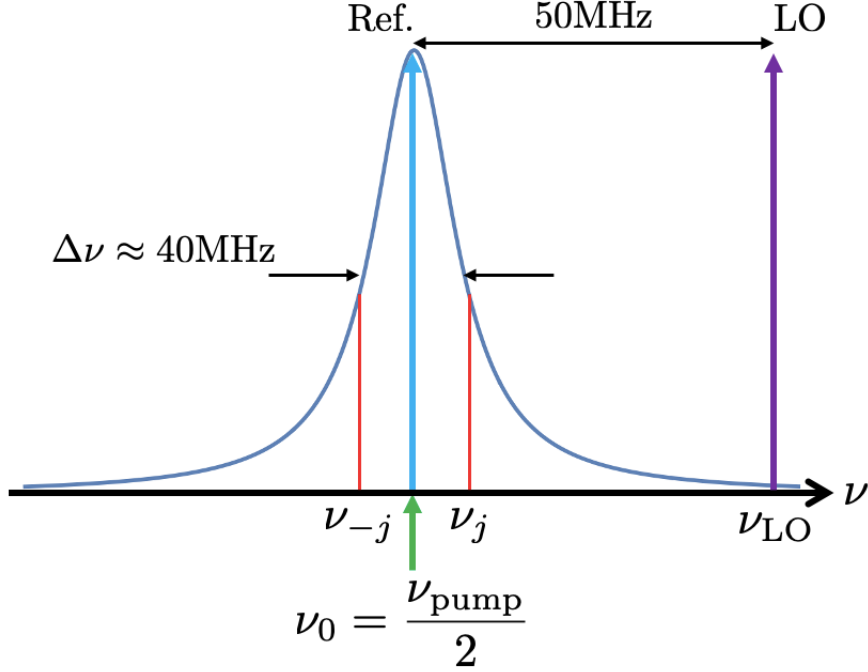


Figure 6.14: Representation of using frequency-shifted LO (purple arrow) and reference beam (sky blue arrow) with respect to the interested comb line in the frequency domain to reconstruct the covariance matrix. Green arrow: half frequency of pump; Blue Lorentzian curve: target comb line; Two Red lines: two intra-modes j and $-j$.

Current experiment setup: Figure 6.15 shows the modified experimental setup. Compared to figure 5.12, a few modifications are performed in order to increase the system stability and to fix the relative phase between quantum light and LO for the covariance matrix construction:

- (1) phase lock between the reference beam and pump beam;
- (2) phase lock between the reference beam and LO;
- (3) the yyy PPKTP crystal has been removed and OPO PDH locking is locked by a transmitted locking beam which is in the same polarization as QOFC;
- (4) removed laser 3 from the experiment and only use laser 1 for LO, the reference beam, and the OPO locking beam.

The principle of the first two modifications will be discussed in the next two sections, but the basic idea is the reference beam acts as a frequency reference for the two phase locks. The pump beam, which determines the phase of quantum light, is locked to the reference beam. The LO is also phase locked to the same reference beam. Therefore, the relative phase between quantum light and LO is fixed. Moreover, to achieve the two phase locks in modification (1) and (2), one common equipment the author would like to mention is the Moku. Moku stands for the Liquid Instruments Moku:Lab, which is a reconfigurable hardware platform that combines the digital signal processing power of an FPGA with versatile analog inputs and outputs. Here, we use the Laser Lock Box function to accomplish the two phase lock loops. Moreover, the two Moku:Labs and function generators for 100 kHz (from Moku 1), 10.5 MHz (Hewlett Packard 3314A function generator), and 50

MHz (two Hewlett Packard 8648A signal generator) signals are all phase locked by the 10 MHz build-in reference signal.

For the third modification, as discussed in the covariance matrix reconstruction above, due to the reason of averaging, it is required to have better stability. We have to switch the OPO locking back to the old one. By doing so, it frees the other port of PBS, which was used for the new PDH lock section 5.2. We thus send 9% power of squeezed light (and reference beam) to a detector, Thorlab PDA10CF InGaAs Amplified Detector, to accomplish the phase lock loop (1).

The reason for the last modification is simply to reduce the phase noise as much as we can, as we discussed in section 5.1.

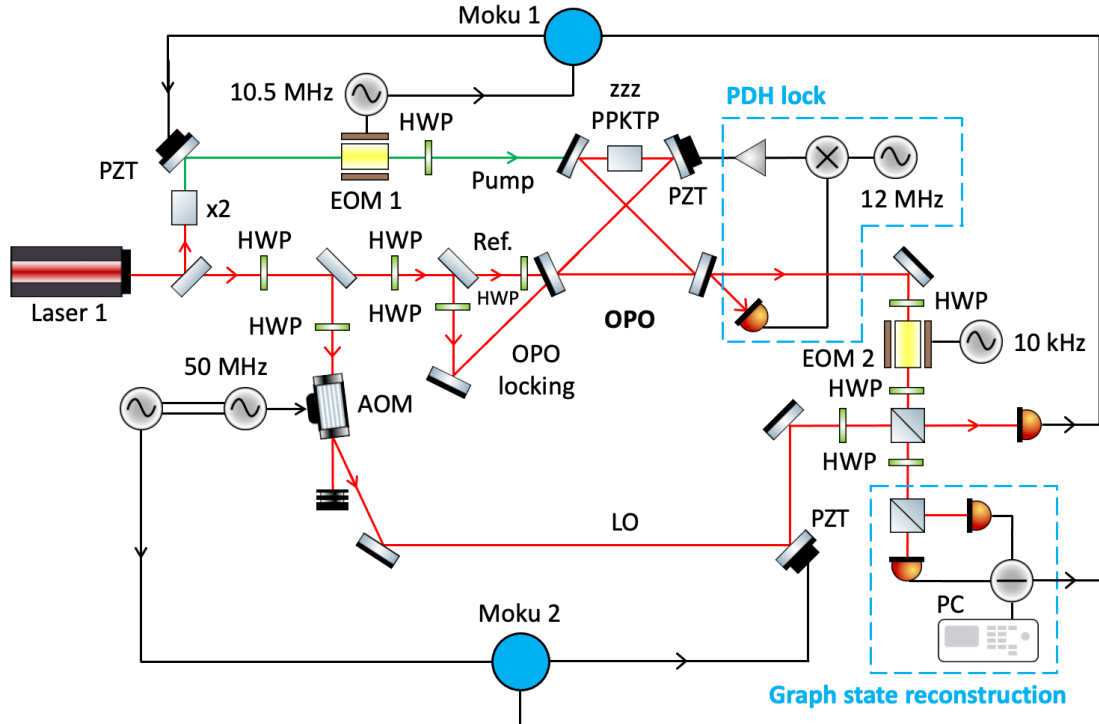


Figure 6.15: Phase stability improved experimental setup. One of the reasons we injected the reference beam is that the reference beam can act as a frequency reference for accomplishing two phase locks. Also note the OPO locking beam, reference beam, and Lo are coming from laser 1. Ref.: reference beam; EOM: electro-optic modulator; AOM: acousto-optic modulator; PDH: Pound-Drever-Hall lock loop; HWP: half-wave plate; PZT: piezoelectric transducer; Moku: Moku:Lab; PC: personal computer.

For the OPO PDH lock, the detector to receive the transmitted locking beam is also a Thorlab PDA015C InGaAs Fixed Gain Amplified Detector. To frequency shift the LO, an IntraAction AOM-402AF3 AOM is used. The EOM 1 is the Conoptics 350-52, which does the phase modulation on the 532 nm pump beam with modulation frequency 10.5 MHz. The EOM2 is the Thorlabs EO-PM-NR-C2 Electro-Optic Phase Modulator, which is used to phase modulate the two-mode squeezed intra-mode pairs. The output signal of the OPA686 based balanced "homodyne" detector with 8 mW LO power is split into two ports by two power splitters, one-fourth of the signal is sent to the Moku 2 to accomplish the phase lock (2), half of the signal is collected by an AlazarTech ATS9440 waveform Digitizer installed in the PC.

6.2.2 Two Optical Phase Locks

6.2.2.a Pump and reference beam phase lock

Derivation of error signal for phase lock: In order to lock the relative phase between the reference beam and QOFC, we utilize the fact that the phase of QOFC is determined by the pump phase. Their phase relations are

$$\phi_p - 2\phi_q = 0 : \text{ parametric down-conversion; } \quad (6.20)$$

$$\phi_p - 2\phi_q = \pi : \text{ parametric up-conversion, } \quad (6.21)$$

where ϕ_p is the phase of the pump beam and ϕ_q is the phase of the QOFC. However, since the whole parametric process starts with a vacuum (no QOFC), if there are QOFC fields, then it implies Eq. (6.20) must hold and ϕ_p can be an arbitrary value. Therefore, the phase of the pump controls the phase of the QOFC mandatorily. On the other hand, since the reference beam doesn't start from the vacuum, then we have the following relations

$$\phi_p - 2\phi_s = 0 : \text{ parametric amplification; } \quad (6.22)$$

$$\phi_p - 2\phi_s = \pi : \text{ parametric deamplification, } \quad (6.23)$$

where ϕ_s is the phase of the reference beam. The Eqs. (6.22) and (6.23) suggest the relative phase between the pump and reference beam led to the amplification and deamplification of the power of the reference beam. We then can apply a phase modulation to the pump, then control their phase. Here is the derivation: Recall the classical form of single-mode squeezing Bogoliubov transformation, Eq. (4.29), due to the phase modulation on the pump (we assume the phase of the reference beam is zero for simplicity), the phase of the pump becomes

$$\phi \rightarrow \phi_0 + m \sin(\Omega t + \theta), \quad (6.24)$$

where $\phi = \phi_p$, ϕ_0 is the initial phase of the pump, m is the modulation index, Ω is the modulation frequency, whose frequency is 10.5 MHz and it is smaller than the linewidth of comb line, 40 MHz, and θ is the initial phase of the RF signal for the modulation. The photon number of the reference beam becomes

$$\begin{aligned} n_s(t) &= |\alpha|^2 (\cosh^2 r + \sinh^2 r) + |\alpha|^2 \sinh 2r \cos \phi \\ &= |\alpha|^2 (\cosh^2 r + \sinh^2 r) + |\alpha|^2 \sinh 2r \cos [\phi_0 + m \sin(\Omega t + \theta)] \\ &= \underbrace{|\alpha|^2 (\cosh^2 r + \sinh^2 2r \cos \phi_0)}_{\text{DC signal}} - \underbrace{m |\alpha|^2 \sinh 2r \sin \phi_0 \sin(\Omega t + \theta)}_{\text{AC signal}}. \end{aligned} \quad (6.25)$$

The photon number of the reference beam can be regarded as a DC signal plus an AC signal, which is a signal with modulation frequency. We can extract the AC signal by demodulating the photon number signal by a signal with frequency Ω and phase δ with the aid of a mixer. The demodulated signal, which is the error signal, becomes

$$\begin{aligned} & -\frac{m}{2} |\alpha|^2 \sinh 2r \sin \phi_0 \cos(\delta + \theta) \\ & \xrightarrow{\theta=0} -\frac{m}{2} |\alpha|^2 \sinh 2r \sin \phi_0 \cos(\delta) \\ & \xrightarrow{\delta=0} -\frac{m}{2} |\alpha|^2 \sinh 2r \sin \phi_0, \end{aligned} \quad (6.26)$$

where we take $\theta = 0$ for simplicity, and $\delta = 0$ due to the demodulated signal phase can be changed to zero easily. We don't take $\phi_0 = 0$ here, because, in experiment, we apply a ramp signal to a PZT mounted mirror in the pump beam path to change ϕ_0 , such that we can see the error signal and lock the phase of pump. The modulation frequency we used in experiment is 10.5 MHz and the ramp signal is typically 10 Hz around. Figure 6.16a shows the calculated error signal with different m with $r = 0.4$ and ϕ_0 from 0 to 4π . Figure 6.16b shows the calculated error signal with different r with $m = 0.2$ and ϕ_0 from 0 to 4π . One can see the larger the value of m or r , the larger the error signal. Note the locking point is the error signal equals to zero, so from figure 6.16, we can lock the relative phase at 0 or π in principle. However, in practice, we can't lock the relative phase at π , due to the reference beam being depleted, so we only can lock at phase of 0, which is the power of reference beam being amplified the most.

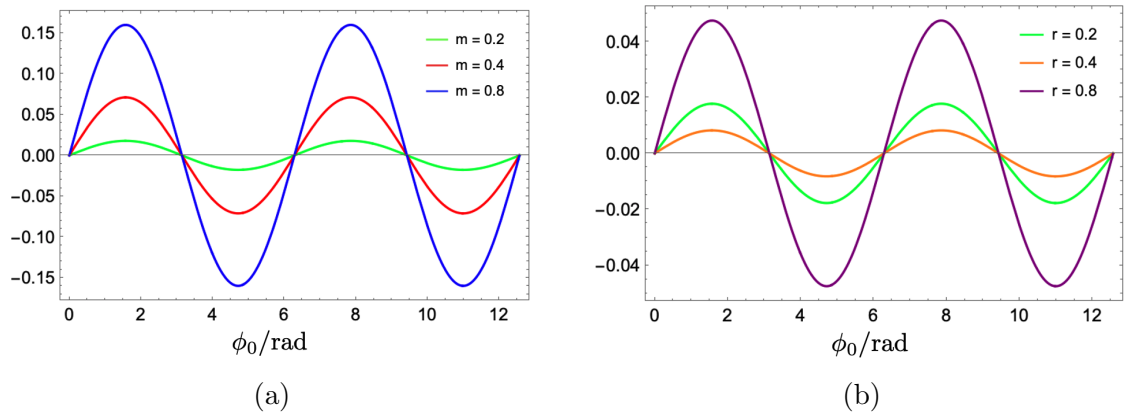


Figure 6.16: Calculated error signals plot against ϕ_0 from 0 to 4π : (a) with $m = 0.2, 0.4,$ and 0.8 while $r = 0.4$; (b) with $r = 0.2, 0.4,$ and 0.8 while $m = 0.2$.

Physical implementation and results: Figure 6.17 shows the simplified schematic experimental setup for the phase lock of the pump and a reference beam. The 10.5 MHz modulation is sent to the EOM 1 implemented in the pump beam path for modulating the pump phase and also sent to the Moku 1 for demodulation. By detecting the reference beam, and demodulating it at the Moku 1, we then can obtain the error signal to PZT mounted mirror to stabilize the relative phase between the pump and reference beam.

Figure 6.18 shows the reference beam power and error signal as the pump phase is scanned by a ramp applied on the pump PZT mirror. Figure 6.18 also shows the XY mode of reference beam power and error signal, whose result is a horizontal ellipse, which indicates the phase between error signal and reference beam power is 90° . And the zero point of the error signal is happening when the reference beam power is amplified the most, which agrees with our prediction.

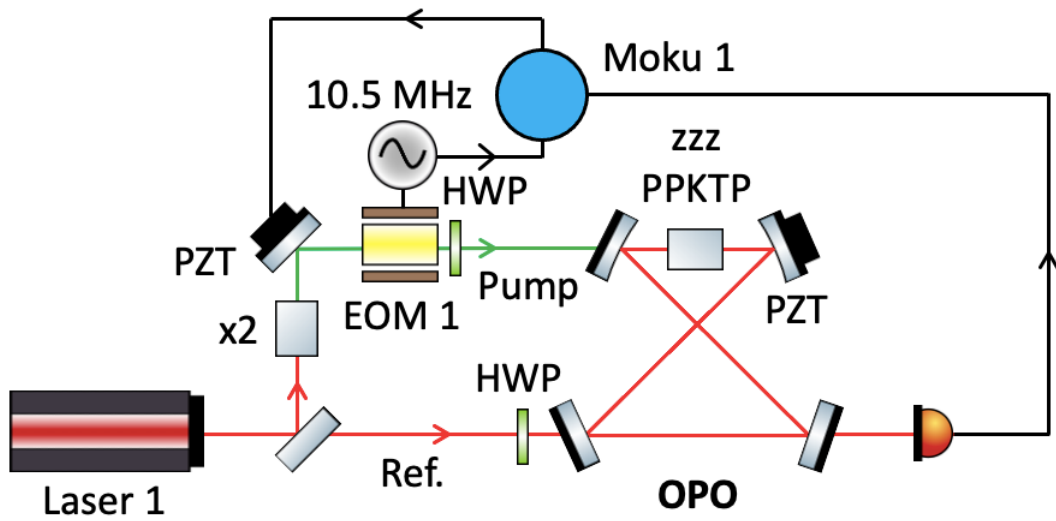


Figure 6.17: Simplified schematic experimental setup for the pump and reference beam phase lock. Ref.: reference beam.

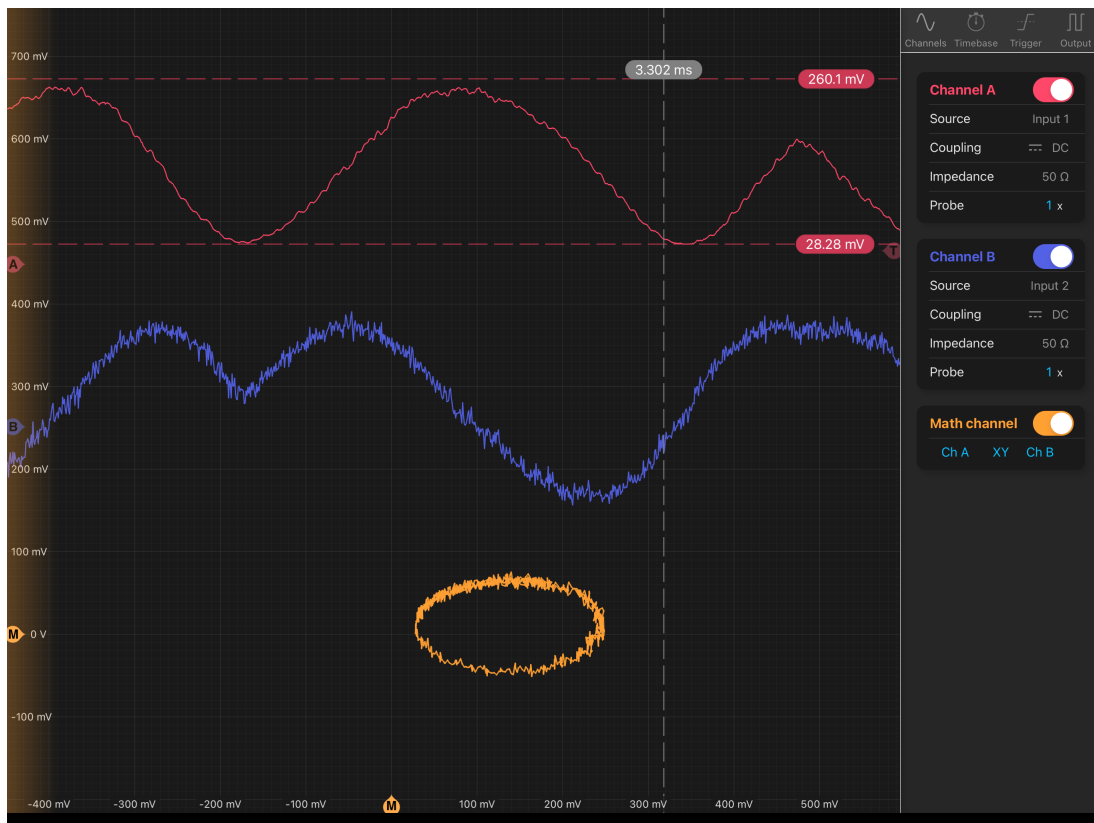
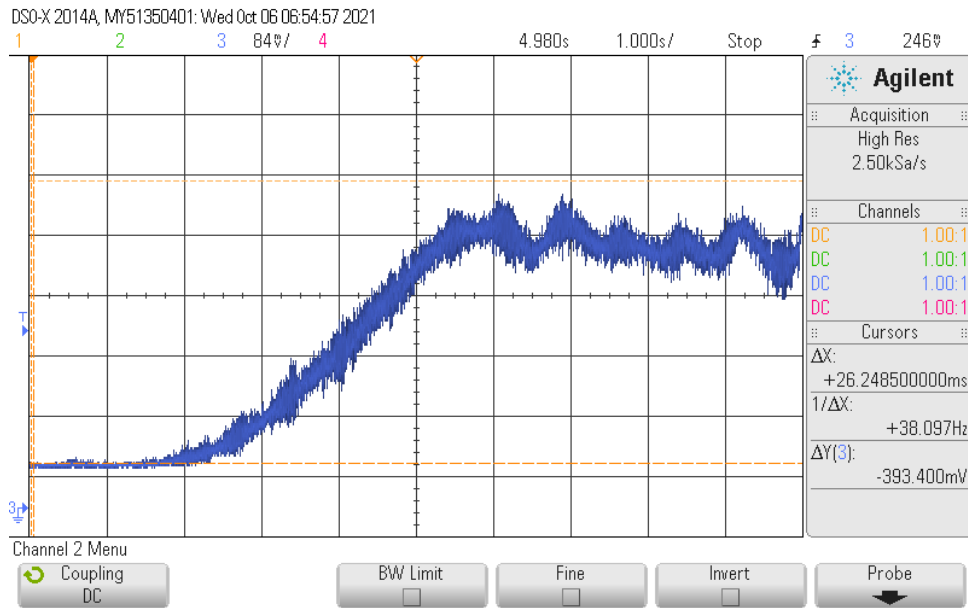


Figure 6.18: Recorded reference beam power (red trace) and the error signal (blue trace) as the pump phase scanned. The yellow trace is the XY mode of reference beam power and error signal, which is a horizontal ellipse. The two red dashed cursors indicate the minimal and maximal value of the reference beam. The y-axis is meaningful to the blue trace.

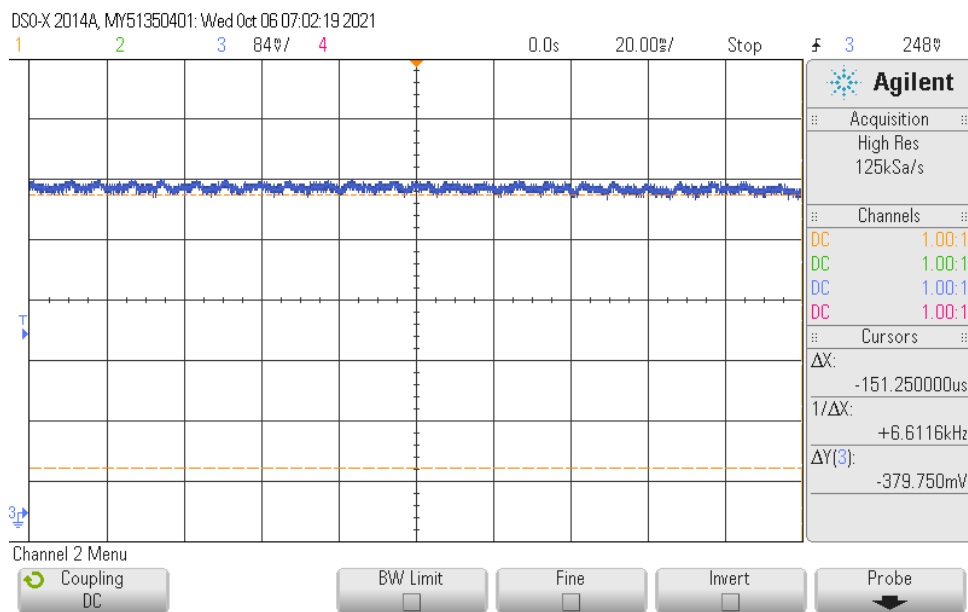
The performance of the reference beam and pump phase lock can be checked by monitoring the reference beam power after the OPO output, as indicated in

figure 6.17, with and without the phase lock. If there is a random relative phase drift, then the reference beam power will fluctuate randomly. Figure 6.19a shows the results without the reference beam and pump phase lock. The two dashed orange horizontal cursors mark the minimal and maximal of the reference beam power, and one can see the reference beam power drifts almost from minimal to maximal value over 5 seconds, which is about 180° phase changing. On the other hand, figure 6.19b shows the case when the reference beam and pump phase lock kicked in. One can see the reference beam power stability is improved by two order of magnitude and the reference beam power can be stabilized for 10 seconds, which is enough for the data taking. Moreover, the reference beam power stays at its maximal, which agrees with what we discussed above that the error signal is 90° with respect to the signal of reference beam power.

6.2. COVARIANCE MATRIX MEASUREMENT SETUP



(a)



(b)

Figure 6.19: Reference beam power without (a) and with (b) the phase lock between the reference beam and pump over 10 seconds. Each box in the horizontal axis is 1 second and in the vertical axis is 84 mV.

6.2.2.b LO and reference beam phase lock

Derivation of error signal for phase lock: The LO is frequency-shifted from the frequency of reference beam by 50 MHz, therefore, we can lock their relative phase by detecting their beat note. Figure 6.20 shows the simplified schematic experimental setup for the phase lock of LO and reference beam. The detail of the phase locked physical implementation will be discussed later. Let's derive the error signal and

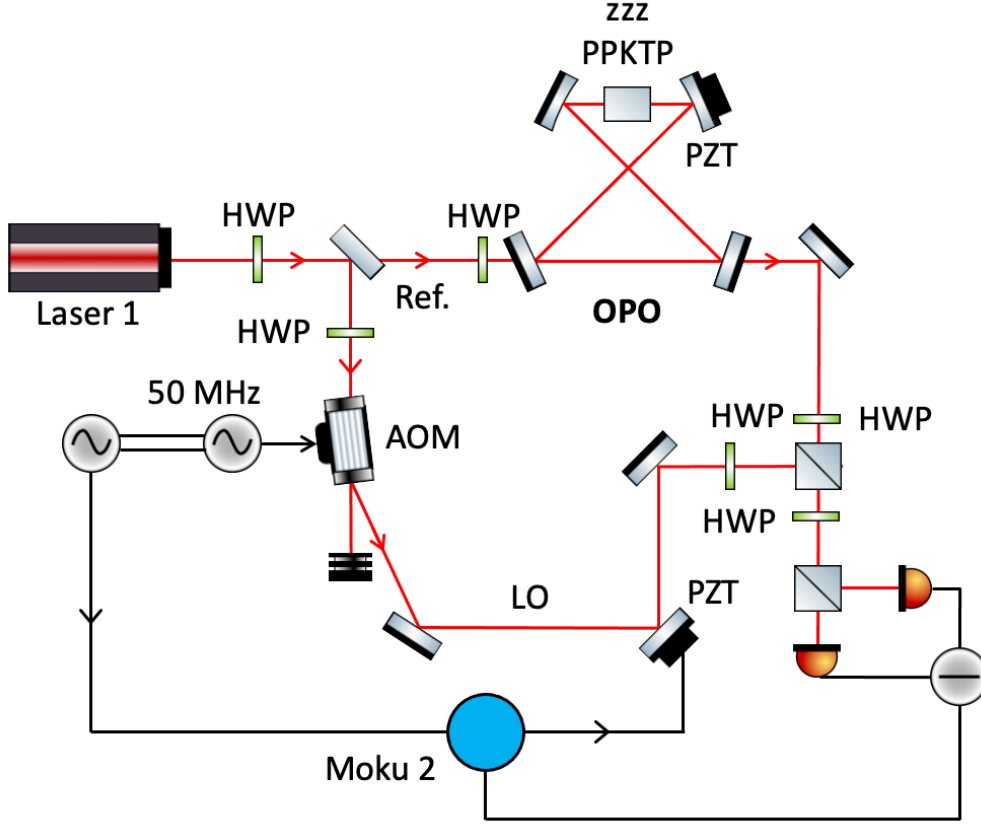


Figure 6.20: Simplified schematic experimental setup for the reference beam and frequency-shifted LO phase lock. Ref.: reference beam.

understand the properties of the error signal first: When two fields enter a detector, the observed signal is

$$\begin{aligned}
 & |E_1 e^{i(\omega_1 t + \phi_1)} + E_2 e^{i(\omega_2 t + \phi_2)}|^2 \\
 &= \underbrace{|E_1|^2 + |E_2|^2}_{\text{DC signal}} + \underbrace{2|E_1 E_2| \cos[(\omega_1 - \omega_2)t + (\phi_1 - \phi_2)]}_{\text{AC signal}}, \quad (6.27)
 \end{aligned}$$

where E_i is the electric field amplitude for field i , ω_i is the frequency of field i , ϕ_i is the initial phase of field i , and $i \in [1, 2]$. With the aid of mixer and a demodulation signal $\cos[\Delta t + \theta]$, where $\Delta = \omega_1 - \omega_2$, we can obtain the error signal (neglecting the DC term due to it will be filter out by a low pass filter)

$$\begin{aligned}
 & \cos[\Delta t + \theta] \times 2|E_1 E_2| \cos[(\omega_1 - \omega_2)t + (\phi_1 - \phi_2)] \\
 &= 2|E_1 E_2| \{ \cos(2\Delta t + \theta + \delta) + \cos(\theta - \delta) \} \\
 & \xrightarrow{\text{after a low pass filter}} 2|E_1 E_2| \cos(\theta - \delta), \quad (6.28)
 \end{aligned}$$

where $\delta = \phi_1 - \phi_2$ is the initial phase difference between the two fields. Figure 6.21 shows the error signal with different demodulated signal phase θ . The lock point is the place where $\theta - \delta = 0$. Therefore, the error signal shifts horizontally as θ changes implying we can lock the relative phase between two fields to any value.

Physical implementation and results: Figure 6.20 shows the simplified schematic experimental setup for the phase lock of LO and reference beam. The

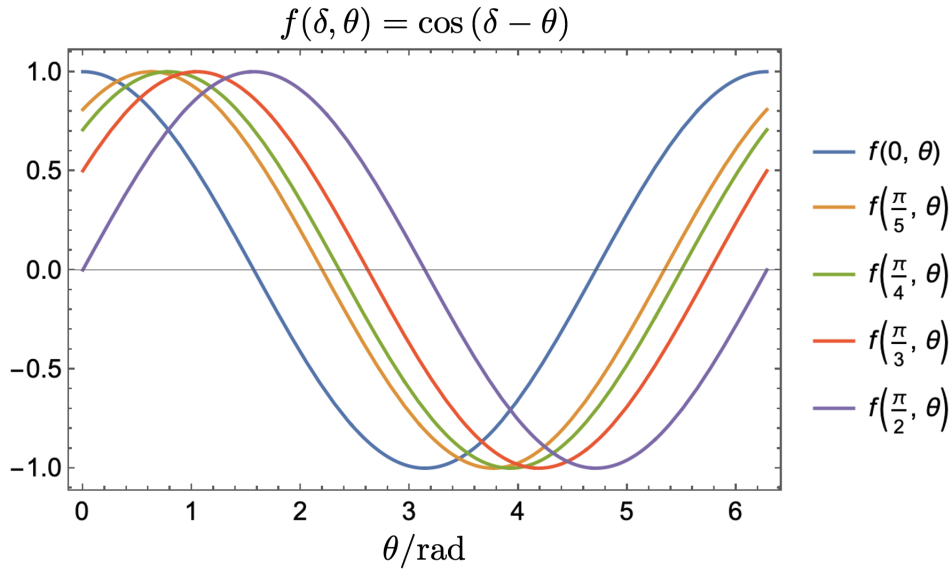


Figure 6.21: Calculated error signal, normalized to $2|E_1 E_2|$, with different demodulated phase δ .

frequency of LO has been frequency-shifted by 50 MHz by an AOM. The LO and reference beam both enter the balanced "homodyne" detector. Due to the interference of the reference beam and LO, there is a $\frac{\pi}{2}$ phase shift between the two fields detected by the photodiodes. Therefore, the subtraction removes the DC signal in Eq. 6.27. Then, the output signal, which 50 MHz beat note signal, from the detector is demodulated at the Moku 2, and the error signal is feedback to the PZT mounted mirror in the LO path to stabilize the phase.

Figure 6.22a shows the beat note of LO and reference beam without the phase lock (one can see the video recording on Youtube by clicking here). Without the phase lock, the beat note is moving around relative to the 50 MHz reference signal, which is phase locked to the signal to modulate the AOM, indicating the relative phase is not stable. Figure 6.22b shows the case when the phase lock kicked in, which improves the phase stability by an order of magnitude (one can check the recording on Youtube by clicking here). Therefore, by implementing a phase lock loop between the reference beam and LO, we can improve the phase stability of their beat note by two order of magnitude.

6.2. COVARIANCE MATRIX MEASUREMENT SETUP

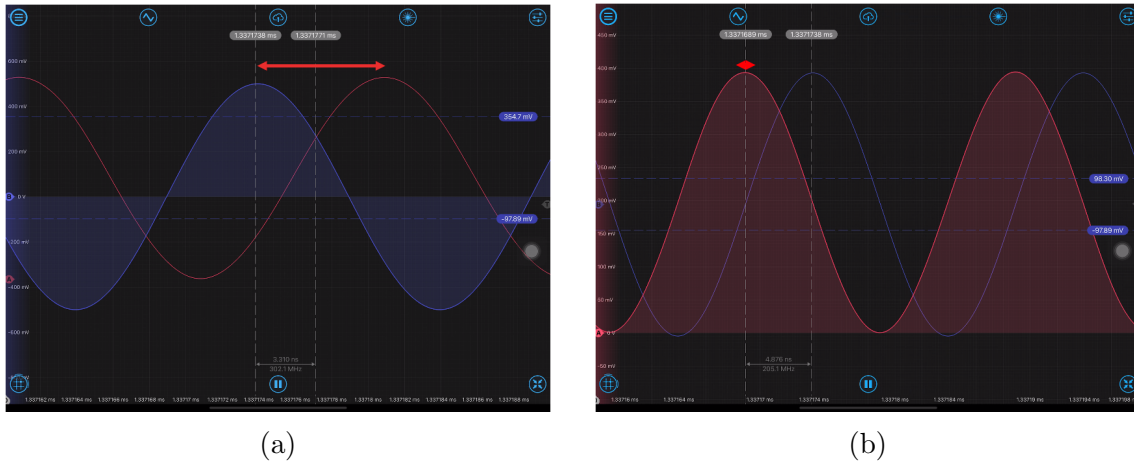


Figure 6.22: Performance test of phase lock between the reference beam and frequency-shifted LO. 50 MHz beat note (red trace) and 50 MHz reference signal (blue trace), which is phase locked to the signal sent to the AOM, without (a) and with (b) the phase lock between the reference beam and LO.

Chapter 7

Conclusion and Future Work

To perform universal quantum computing by CV measurement-based quantum computer, a 2-d or 3-d cluster state is one of the crucial conditions. The 2-d cluster states are required for performing universal quantum computing. With the 3-d cluster states, one can perform the topological error correcting code to further reduce the error rate. For the first part of this thesis, the goal is to provide a method to generate higher-dimensional cluster states and verify the cluster states in the experiment. I presented a simple method to achieve the goal by a phase-modulated quantum optical frequency comb. Specifically, by using only one OPO and one EOM, our method can generate 1-d, 2-d, and 3-d cluster states. A measurement principle and plan for verifying the cluster states by reconstructing the covariance matrix was discussed. In order to reconstruct the covariance matrix by heterodyne measurement, several improvements in the apparatus has to be implemented. Specifically, the phase noise needs to be as smaller as possible, the optical phase between LO and quantum fields needs to be stable, the balanced homodyne detector needs to have enough bandwidth, and the measured squeezing needs to be as high as possible. And the second part of this thesis describes those implementations.

I discussed the key element in this experiment, the OPO, from a classical point of view to a quantum point of view. I have presented my experimental work to improve the stability and sensitivity of the optical system, for the purpose of realizing cluster states by the phase modulation method. For the performance improvement, I have shown the work of improving the sensitivity of a balanced homodyne detector, from a simple model to estimate the SNR to a real implementation. An anomalous OPO reflection mode has been shown for the purpose of knowing which beams, reflected beam or transmitted beam, can be used to mimic the OPO output mode. For the stability improvement, I have presented the work of phase noise investigation, the improvement of OPO PDH cavity locking from SNR 40 to 3000, phase lock between pump and reference beam and improving their relative phase stability by two orders of magnitude, and the phase lock between the reference beam and LO and improving their relative phase stability by two orders of magnitude. I also have presented the work of increasing the squeezing by changing the OPO output coupler from $T = 5\%$ to 17% , and increased the observed squeezing from 3.2 dB to 5.0 dB. A discussion about increasing the squeezing by changing the OPO OC is also presented in this thesis.

Future work: The future work will focus on experimentally verifying the cluster states by reconstructing the covariance matrix. So, the first thing to check is if our

new method, heterodyne measurement, to reconstruct the covariance matrix can work. Due to the complexity of the results obtained from Fourier transform, we are planning to reconstruct the covariance matrix of the two-mode squeezed QOFC first. Once we successfully reconstruct the two-mode squeezed QOFC, then we can increase the complexity of the states by applying one modulation frequency to the QOFC.

On the other hand, we are desired to have measured squeezing as large as possible, for the reason of resolving the weak edges in the cluster states. Therefore, increasing the pump power to obtain more gain and squeezing is desired. One way to achieve this goal is coherently combining the 532 nm pump beam from laser 1 with another laser by phase lock the two lasers together, so that we can inject more pump power into the OPO. Due to the high squeezing is much mores sensitive to lower squeezing, we also need to further reduce the phase noise and loss in the apparatus.

Lastly, we would like to modify the pump and reference beam phase lock. Currently, we sent 9% of the reference beam and squeezed light to the phase lock detector, which is a 9% loss to the squeezed light and it degrades the squeezing. Therefore, for the purpose of obtaining high squeezing, we want to lock the pump and reference beam by using other methods and thus lowering the loss. Once the above few improvements can be implemented, the QFQI lab at the University of Virginia should be able to reconstruct the covariance matrices of any 2-d and 3-d cluster states.

Bibliography

- [1] Frank Arute, Kunal Arya, Ryan Babbush, Dave Bacon, Joseph C. Bardin, Rami Barends, Rupak Biswas, Sergio Boixo, Fernando G. S. L. Brandao, David A. Buell, Brian Burkett, Yu Chen, Zijun Chen, Ben Chiaro, Roberto Collins, William Courtney, Andrew Dunsworth, Edward Farhi, Brooks Foxen, Austin Fowler, Craig Gidney, Marissa Giustina, Rob Graff, Keith Guerin, Steve Habegger, Matthew P. Harrigan, Michael J. Hartmann, Alan Ho, Markus Hoffmann, Trent Huang, Travis S. Humble, Sergei V. Isakov, Evan Jeffrey, Zhang Jiang, Dvir Kafri, Kostyantyn Kechedzhi, Julian Kelly, Paul V. Klimov, Sergey Knysh, Alexander Korotkov, Fedor Kostritsa, David Landhuis, Mike Lindmark, Erik Lucero, Dmitry Lyakh, Salvatore Mandrà, Jarrod R. McClean, Matthew McEwen, Anthony Megrant, Xiao Mi, Kristel Michielsen, Masoud Mohseni, Josh Mutus, Ofer Naaman, Matthew Neeley, Charles Neill, Murphy Yuezhen Niu, Eric Ostby, Andre Petukhov, John C. Platt, Chris Quintana, Eleanor G. Rieffel, Pedram Roushan, Nicholas C. Rubin, Daniel Sank, Kevin J. Satzinger, Vadim Smelyanskiy, Kevin J. Sung, Matthew D. Trevithick, Amit Vainsencher, Benjamin Villalonga, Theodore White, Z. Jamie Yao, Ping Yeh, Adam Zalcman, Hartmut Neven, and John M. Martinis. Quantum supremacy using a programmable superconducting processor. *Nature*, 574(7779):505–510, October 2019. Bandiera_abtest: a Cg_type: Nature Research Journals Number: 7779 Primary_atype: Research Publisher: Nature Publishing Group Subject_term: Quantum information;Quantum physics Subject_term_id: quantum-information;quantum-physics.
- [2] Warit Asavanant, Yu Shiozawa, Shota Yokoyama, Baramjee Charoensombutamon, Hiroki Emura, Rafael N. Alexander, Shuntaro Takeda, Jun ichi Yoshikawa, Nicolas C. Menicucci, Hidehiro Yonezawa, and Akira Furusawa. Generation of time-domain-multiplexed two-dimensional cluster state. *Science*, 366(6463):373–376, 2019.
- [3] Dave Bacon. Too entangled to quantum compute one-way. *Physics*, 2:38, May 2009.
- [4] Stephen D. Bartlett, Barry C. Sanders, Samuel L. Braunstein, and Kae Nemoto. Efficient classical simulation of continuous variable quantum information processes. *Phys. Rev. Lett.*, 88:097904, 2002.
- [5] Gary C. Bjorklund. Frequency-modulation spectroscopy: a new method for measuring weak absorptions and dispersions. *Opt. Lett.*, 5:15, 1980.
- [6] Eric D. Black. An introduction to pound–drever–hall laser frequency stabilization. *American Journal of Physics*, 69(1):79–87, 2001.

- [7] Michael J. Bremner, Caterina Mora, and Andreas Winter. Are random pure states useful for quantum computation? Phys. Rev. Lett., 102:190502, May 2009.
- [8] H. J. Briegel and R. Raussendorf. Persistent entanglement in arrays of interacting particles. Phys. Rev. Lett., 86:910, 2001.
- [9] Dan E. Browne and Hans J. Briegel. One-way quantum computation - a tutorial introduction. arXiv, 2006.
- [10] Richard A. Campos, Bahaa E. A. Saleh, and Malvin C. Teich. Quantum-mechanical lossless beam splitter: $Su(2)$ symmetry and photon statistics. Phys. Rev. A, 40:1371–1384, Aug 1989.
- [11] José Capmany and Carlos R. Fernández-Pousa. Quantum model for electro-optical phase modulation. J. Opt. Soc. Am. B, 27(6):A119–A129, Jun 2010.
- [12] Moran Chen. Large-scale cluster-state entanglement in the quantum optical frequency comb. University of Virginia, 2015.
- [13] Moran Chen, Nicolas C. Menicucci, and Olivier Pfister. Experimental realization of multipartite entanglement of 60 modes of a quantum optical frequency comb. Phys. Rev. Lett., 112:120505, Mar 2014.
- [14] D. DiVincenzo. Scalable quantum computers. Paving the way to realization, chapter The physical implementation of quantum computation, page 1. Wiley, 2001.
- [15] R. W. P. Drever, J. L. Hall, F. V. Kowalski, J. Hough, G. M. Ford, A. J. Munley, and H. Ward. Laser phase and frequency stabilization using an optical resonator. Appl. Phys. B, 31:97–105, 1983.
- [16] A. Einstein, B. Podolsky, and N. Rosen. Can quantum-mechanical description of physical reality be considered complete? Phys. Rev., 47:777, 1935.
- [17] S. Emanuelli and A. Arie. Temperature-dependent dispersion equations for $KTiOPO_4$ and $KTiOAsO_4$. Appl. Opt., 42:6661, 2003.
- [18] M. M. Fejer, G. A. Magel, D. H. Jundt, and R. L. Byer. Quasi-phase-matched second harmonic generation: tuning and tolerances. IEEE J. Quantum Electron., 28:2631, 1992.
- [19] Richard P. Feynman. Simulating physics with computers. Int. J. Theor. Phys., 21:467–488, 1982.
- [20] S. T. Flammia, N. C. Menicucci, and O. Pfister. The optical frequency comb as a one-way quantum computer. J. Phys. B., 42:114009, 2009.
- [21] K. Fradkin, A. Arie, A. Skliar, and G. Rosenman. Tunable midinfrared source by difference frequency generation in bulk periodically poled $KTiOPO_4$. Appl. Phys. Lett., 74(7):914–916, 1999.

- [22] Kosuke Fukui, Akihisa Tomita, Atsushi Okamoto, and Keisuke Fujii. High-threshold fault-tolerant quantum computation with analog quantum error correction. Phys. Rev. X, 8:021054, May 2018.
- [23] Carlos González-Arciniegas, Olivier Pfister, Paulo Nussenzveig, and Marcelo Martinelli. Hidden entanglement in gaussian cluster states. In OSA Quantum 2.0 Conference, page QW6B.4. Optical Society of America, 2020.
- [24] Carlos González-Arciniegas, Paulo Nussenzveig, Marcelo Martinelli, and Olivier Pfister. Cluster states from gaussian states: Essential diagnostic tools for continuous-variable one-way quantum computing. PRX Quantum, 2:030343, Sep 2021.
- [25] D. Gross, S. T. Flammia, and J. Eisert. Most quantum states are too entangled to be useful as computational resources. Phys. Rev. Lett., 102:190501, May 2009.
- [26] Mile Gu, Christian Weedbrook, Nicolas C. Menicucci, Timothy C. Ralph, and Peter van Loock. Quantum computing with continuous-variable clusters. Phys. Rev. A, 79:062318, 2009.
- [27] P. Hyllus and J. Eisert. Optimal entanglement witnesses for continuous-variable systems. New J. Phys., 8(4):51, 2006.
- [28] M.S. Kim, W. Son, V. Bužek, and P.L. Knight. Entanglement by a beam splitter: Nonclassicality as a prerequisite for entanglement. Phys. Rev. A, 65:032323, 2002.
- [29] Ping Koy Lam. Applications of quantum electro-optic control and squeezed light. Australian National University, 1998.
- [30] Mikkel V. Larsen, Xueshi Guo, Casper R. Breum, Jonas S. Neergaard-Nielsen, and Ulrik L. Andersen. Deterministic generation of a two-dimensional cluster state. Science, 366(6463):369–372, 2019.
- [31] Seth Lloyd and Samuel L. Braunstein. Quantum computation over continuous variables. Physical Review Letters, 82(8):1784–1787, February 1999. arXiv: quant-ph/9810082.
- [32] A. V. Masalov, A. Kuzhamuratov, and A. I. Lvovsky. Noise spectra in balanced optical detectors based on transimpedance amplifiers. Review of Scientific Instruments, 88(11):113109, 2017.
- [33] N. C. Menicucci, P. van Loock, M. Gu, C. Weedbrook, T. C. Ralph, and M. A. Nielsen. Universal quantum computation with continuous-variable cluster states. Phys. Rev. Lett., 97:110501, 2006.
- [34] Nicolas C. Menicucci. Fault-tolerant measurement-based quantum computing with continuous-variable cluster states. Phys. Rev. Lett., 112:120504, Mar 2014.
- [35] Nicolas C. Menicucci, Steven T. Flammia, and Olivier Pfister. One-way quantum computing in the optical frequency comb. Phys. Rev. Lett., 101:130501, 2008.

- [36] Nicolas C. Menicucci, Steven T. Flammia, and Peter van Loock. Graphical calculus for Gaussian pure states with applications to continuous-variable cluster states. Phys. Rev. A, 83:042335, 2011.
- [37] Nicolas C. Menicucci, Peter van Loock, Mile Gu, Christian Weedbrook, Timothy C. Ralph, and Michael A. Nielsen. Universal Quantum Computation with Continuous-Variable Cluster States. Physical Review Letters, 97(11), September 2006. arXiv: quant-ph/0605198.
- [38] Ashley Montanaro. Quantum algorithms: an overview. Npj Quantum Information, 2:15023 EP –, 01 2016.
- [39] Rajveer Nehra. Non-gaussian states and measurements in quantum information science. University of Virginia, July 2020.
- [40] Michael A. Nielsen and Isaac L. Chuang. Quantum computation and quantum information. Cambridge University Press, Cambridge, U.K., 2000.
- [41] Z. Y. Ou, S. F. Pereira, H. J. Kimble, and K. C. Peng. Realization of the Einstein-Podolsky-Rosen paradox for continuous variables. Phys. Rev. Lett., 68:3663, 1992.
- [42] O. Pfister and N.-K. Tran. Number-phase teleportation and the heisenberg limit: a “paradox” and some surprises. In Quantum Communication and Quantum Imaging, volume 5161 of SPIE Proceedings, page 9, 2004.
- [43] Oliver Pfister. Quantum optics and quantum information lecture notes. 2018.
- [44] Oliver Pfister. Continuous-variable quantum computing in the quantum optical frequency comb. J. Phys. B, 53:012001, 2020.
- [45] Olivier Pfister, Sheng Feng, Gregory Jennings, Raphael Pooser, and Daruo Xie. Multipartite continuous-variable entanglement from concurrent nonlinearities. Phys. Rev. A, 70(2):020302, 2004.
- [46] R. C. Pooser and O. Pfister. Observation of triply coincident nonlinearities in periodically poled KTiOPO₄. Opt. Lett., 30:2635, 2005.
- [47] M. Pysher, A. Bahabad, P. Peng, A. Arie, and O. Pfister. Quasi-phase-matched concurrent nonlinearities in periodically poled KTiOPO₄ for quantum computing over the optical frequency comb. Opt. Lett., 35:565, 2010.
- [48] Matthew Pysher, Yoshichika Miwa, Reihaneh Shahrokhshahi, Russell Bloomer, and Olivier Pfister. Parallel generation of quadripartite cluster entanglement in the optical frequency comb. Phys. Rev. Lett., 107(3):030505, Jul 2011.
- [49] R. Raussendorf and H. J. Briegel. A one-way quantum computer. Phys. Rev. Lett., 86:5188, 2001.
- [50] R Raussendorf, J Harrington, and K Goyal. A fault-tolerant one-way quantum computer. Ann. Phys. (NY), 321(9):2242–2270, 2006.

- [51] Robert Raussendorf, Daniel E Browne, and Hans J. Briegel. The one-way quantum computer—a non-network model of quantum computation. J. Mod. Opt., 49:1299, 2002.
- [52] C. Schori, J. L. Sørensen, and E. S. Polzik. Narrow-band frequency tunable light source of continuous quadrature entanglement. Phys. Rev. A, 66:033802, 2002.
- [53] P. W. Shor. Algorithms for quantum computation: discrete logarithms and factoring. In S. Goldwasser, editor, Proceedings, 35th Annual Symposium on Foundations of Computer Science, pages 124–134, Santa Fe, NM, 1994. IEEE Press, Los Alamitos, CA.
- [54] Peter W. Shor. Polynomial-time algorithms for prime factorization and discrete logarithms on a quantum computer. SIAM Journal on Computing, 26(5):1484–1509, 1997.
- [55] M. Stobińska, A. Buraczewski, M. Moore, W. R. Clements, J. J. Renema, S. W. Nam, T. Gerrits, A. Lita, W. S. Kolthammer, A. Eckstein, and I. A. Walmsley. Quantum interference enables constant-time quantum information processing. Science Advances, 5(7):eaau9674, 2019.
- [56] Henning Vahlbruch, Moritz Mehmet, Karsten Danzmann, and Roman Schnabel. Detection of 15 dB squeezed states of light and their application for the absolute calibration of photoelectric quantum efficiency. Phys. Rev. Lett., 117:110801, Sep 2016.
- [57] D. F. Walls and G. J. Milburn. Quantum Optics. Springer, Berlin, 1994.
- [58] Blayne W. Walshe, Lucas J. Mensen, Ben Q. Baragiola, and Nicolas C. Menicucci. Robust fault tolerance for continuous-variable cluster states with excess antisqueezing. Phys. Rev. A, 100:010301, Jul 2019.
- [59] Pei Wang. Weaving the quantum optical frequency combs into hypercubic cluster states. University of Virginia, 2016.
- [60] Pei Wang, Rafael N. Alexander, Niranjana Sridhar, Moran Chen, Nicolas C. Menicucci, and Olivier Pfister. Scrolling the quantum optical frequency comb: one-way quantum computing with hybrid time-frequency entanglement. in preparation, 2015.
- [61] Pei Wang, Wenjiang Fan, and Olivier Pfister. Engineering large-scale entanglement in the quantum optical frequency comb: influence of the quasiphase-matching bandwidth and of dispersion. arXiv:1403.6631 [physics.optics], 2014.
- [62] Ling-An Wu, Min Xiao, and H. J. Kimble. Squeezed states of light from an optical parametric oscillator. J. Opt. Soc. Am. B, 4(10):1465–1475, Oct 1987.
- [63] Shota Yokoyama, Ryuji Ukai, Seiji C Armstrong, Chanond Sornphiphatphong, Toshiyuki Kaji, Shigenari Suzuki, Jun-Ichi Yoshikawa, Hidehiro Yonezawa, Nicolas C Menicucci, and Akira Furusawa. Ultra-large-scale continuous-variable cluster states multiplexed in the time domain. Nature Photonics, 7(12):982–986, December 2013.

- [64] Jun-ichi Yoshikawa, Shota Yokoyama, Toshiyuki Kaji, Chanond Sornphiphat-phong, Yu Shiozawa, Kenzo Makino, and Akira Furusawa. Invited article: Generation of one-million-mode continuous-variable cluster state by unlimited time-domain multiplexing. *APL Photonics*, 1(6):060801, 2016.
- [65] Mitsuyoshi Yukawa, Ryuji Ukai, Peter van Loock, and Akira Furusawa. Experimental generation of four-mode continuous-variable cluster states. *Phys. Rev. A*, 78:012301, 2008.
- [66] H. Zaidi, N. C. Menicucci, S. T. Flammia, R. Bloomer, M. Pysher, and O. Pfister. Entangling the optical frequency comb: simultaneous generation of multiple 2x2 and 2x3 continuous-variable cluster states in a single optical parametric oscillator. *Laser Phys.*, 18:659, 2008. Revised version at <http://arxiv.org/pdf/0710.4980v3>.
- [67] J. Zang, Z. Yang, X. Xie, M. Ren, Y. Shen, Z. Carson, O. Pfister, A. Beling, and J. Campbell. High quantum efficiency uni-traveling-carrier photodiode. *IEEE Photonics Technology Letters*, 29:302, 2017.
- [68] Jing Zhang and Samuel L. Braunstein. Continuous-variable Gaussian analog of cluster states. *Phys. Rev. A*, 73(3):032318, 2006.
- [69] Han-Sen Zhong, Hui Wang, Yu-Hao Deng, Ming-Cheng Chen, Li-Chao Peng, Yi-Han Luo, Jian Qin, Dian Wu, Xing Ding, Yi Hu, Peng Hu, Xiao-Yan Yang, Wei-Jun Zhang, Hao Li, Yuxuan Li, Xiao Jiang, Lin Gan, Guangwen Yang, Lixing You, Zhen Wang, Li Li, Nai-Le Liu, Chao-Yang Lu, and Jian-Wei Pan. Quantum computational advantage using photons. *Science*, 370(6523):1460–1463, 2020.
- [70] Xuan Zhu, Chun-Hung Chang, Carlos González-Arciniegas, Avi Pe’er, Jacob Higgins, and Olivier Pfister. Hypercubic cluster states in the phase-modulated quantum optical frequency comb. *Optica*, 8(3):281–290, Mar 2021.